NAVAL POSTGRADUATE SCHOOL

MONTEREY, CALIFORNIA

THESIS

SMALL, ROTOR POWERED, UNMANNED AERIAL VEHICLE DIRECTION OF ARRIVAL DETERMINATION USING BIO-INSPIRED MICROELECTROMECHANICAL SENSORS

by

David J. Hatch

June 2022

Thesis Advisor: Fabio Durante Pereira Alves
Co-Advisor: Gamani Karunasiri

Approved for public release. Distribution is unlimited.

THIS PAGE INTENTIONALLY LEFT BLANK

REPORT DOCUMENTATION PAGE	Form Approved OMB No. 0704-0188

Public reporting burden for this collection of information is estimated to average 1 hour per response, including the time for reviewing instruction, searching existing data sources, gathering and maintaining the data needed, and completing and reviewing the collection of information. Send comments regarding this burden estimate or any other aspect of this collection of information, including suggestions for reducing this burden, to Washington headquarters Services, Directorate for Information Operations and Reports, 1215 Jefferson Davis Highway, Suite 1204, Arlington, VA 22202-4302, and to the Office of Management and Budget, Paperwork Reduction Project (0704-0188) Washington, DC, 20503.

1. AGENCY USE ONLY *(Leave blank)*	2. REPORT DATE June 2022	3. REPORT TYPE AND DATES COVERED Master's thesis

4. TITLE AND SUBTITLE SMALL, ROTOR POWERED, UNMANNED AERIAL VEHICLE DIRECTION OF ARRIVAL DETERMINATION USING BIO-INSPIRED MICROELECTROMECHANICAL SENSORS	5. FUNDING NUMBERS
6. AUTHOR(S) David J. Hatch	
7. PERFORMING ORGANIZATION NAME(S) AND ADDRESS(ES) Naval Postgraduate School Monterey, CA 93943-5000	8. PERFORMING ORGANIZATION REPORT NUMBER
9. SPONSORING / MONITORING AGENCY NAME(S) AND ADDRESS(ES) N/A	10. SPONSORING / MONITORING AGENCY REPORT NUMBER

11. SUPPLEMENTARY NOTES The views expressed in this thesis are those of the author and do not reflect the official policy or position of the Department of Defense or the U.S. Government.

12a. DISTRIBUTION / AVAILABILITY STATEMENT Approved for public release. Distribution is unlimited.	12b. DISTRIBUTION CODE A

13. ABSTRACT (maximum 200 words)

Previous research developed a bio-inspired microelectromechanical system (MEMS) acoustic sensor, based on the hearing organ of the parasitic fly *Ormia ochracea*. It was previously demonstrated that the direction of a small, rotor powered, unmanned aerial vehicle (UAV) can be estimated using this acoustic sensor. Building on this previous work, the objective of this study was to develop a method to unambiguously determine the direction of arrival of the sound of small UAVs using an array of collocated MEMS sensors. This task was performed under the premise that the directional response of the sensors in the array could be modified to exhibit an asymmetric dipole pattern or a cardioid pattern. The proposed DOA estimation method, using comparison across normalized calibration curves, was analyzed across several different conditions. Promising results were obtained, where the best accuracy was found for the array with a cardioid directional pattern. Error was as low as one degree across a 360° azimuth range for signal-to-noise ratios of 20 dB and higher for a small hexacopter UAV. The developed method can be applied to determine the direction of arrival of potentially any acoustic source detectable by the MEMS sensors.

14. SUBJECT TERMS Ormia ochracea, angle of arrival, AOA, drone, UAV, MEMS sensor, acoustic, detection, direction, direction of arrival, DOA	15. NUMBER OF PAGES 107
	16. PRICE CODE

17. SECURITY CLASSIFICATION OF REPORT	18. SECURITY CLASSIFICATION OF THIS PAGE	19. SECURITY CLASSIFICATION OF ABSTRACT	20. LIMITATION OF ABSTRACT
Unclassified	Unclassified	Unclassified	UU

NSN 7540-01-280-5500

Standard Form 298 (Rev. 2-89)
Prescribed by ANSI Std. 239-18

THIS PAGE INTENTIONALLY LEFT BLANK

Approved for public release. Distribution is unlimited.

SMALL, ROTOR POWERED, UNMANNED AERIAL VEHICLE DIRECTION OF ARRIVAL DETERMINATION USING BIO-INSPIRED MICROELECTROMECHANICAL SENSORS

David J. Hatch
Lieutenant Commander, United States Navy
BS, Rochester Institute of Technology, 2010

Submitted in partial fulfillment of the
requirements for the degree of

MASTER OF SCIENCE IN APPLIED PHYSICS

from the

NAVAL POSTGRADUATE SCHOOL
June 2022

Approved by: Fabio Durante Pereira Alves
Advisor

Gamani Karunasiri
Co-Advisor

Joseph P. Hooper
Chair, Department of Physics

THIS PAGE INTENTIONALLY LEFT BLANK

ABSTRACT

Previous research developed a bio-inspired microelectromechanical system (MEMS) acoustic sensor, based on the hearing organ of the parasitic fly *Ormia ochracea*. It was previously demonstrated that the direction of a small, rotor powered, unmanned aerial vehicle (UAV) can be estimated using this acoustic sensor. Building on this previous work, the objective of this study was to develop a method to unambiguously determine the direction of arrival of the sound of small UAVs using an array of collocated MEMS sensors. This task was performed under the premise that the directional response of the sensors in the array could be modified to exhibit an asymmetric dipole pattern or a cardioid pattern. The proposed DOA estimation method, using comparison across normalized calibration curves, was analyzed across several different conditions. Promising results were obtained, where the best accuracy was found for the array with a cardioid directional pattern. Error was as low as one degree across a 360° azimuth range for signal-to-noise ratios of 20 dB and higher for a small hexacopter UAV. The developed method can be applied to determine the direction of arrival of potentially any acoustic source detectable by the MEMS sensors.

THIS PAGE INTENTIONALLY LEFT BLANK

TABLE OF CONTENTS

I. INTRODUCTION 1
  A. BACKGROUND 1
    1. *Ormia Ochracea* MEMS Sensor 1
    2. Threat from Small, Rotor Powered UAVs 2
    3. Status of Research 4
  B. OBJECTIVE AND THESIS ORGANIZATION 9

II. SENSOR DESCRIPTION AND DOA ESTIMATION METHOD 11
  A. SENSOR ARRAY DESCRIPTION 11
    1. Mathematical Model of the Sensor Array Response 14
    2. DOA Estimation Method 20

III. ALGORITHM EXPERIMENTAL RESULTS 27
  A. MODELED ALGORITHM RESPONSE AND FIGURES OF MERIT 27
    1. Effects of Sensor Frequency Response Mismatch 32
    2. Effects of Signal-to-Noise Ratio 35
    3. Effects of Directional Response Fluctuations 38
    4. Effects of Drone Type 41
    5. Cause of Ambiguous DOAs and Errors Greater than Ten Degrees 46
  B. MEASURED SENSOR RESPONSES 49
    1. Asymmetric Dipole Pattern Response 49
    2. Cardioid Pattern Response 55

IV. CONCLUSION 63
  A. SUMMARY OF RESULTS 63
  B. RECOMMENDATIONS FOR FUTURE WORK 65

APPENDIX A. DERIVATION OF DIF/SUM TANGENT FUNCTIONS FOR THREE DIRECTIONAL SENSORS 67

APPENDIX B. DERIVATION OF DIF/SUM TANGENT FUNCTIONS FOR SENSORS OF UNEQUAL MAGNITUDES 73

APPENDIX C. ADDITIONAL DATA PLOTS 77

SUPPLEMENTAL **83**

LIST OF REFERENCES **85**

INITIAL DISTRIBUTION LIST **89**

LIST OF FIGURES

Figure 1. Three-Dimensional Orientation of Four Microphone Array from Liu et al. Source: [30]. 6

Figure 2. Schematic Diagram of a Typical *Ormia*-inspired Sensor Designed by Our Research Group 11

Figure 3. (a) Simulated MEMS Sensor Frequency Response. (b) Measured MEMS Sensor Directional Pattern at the Sensor's Bending Frequency from Wilmott et al. Source: [31] 12

Figure 4. (a) *Ormia*-inspired Bending Mode Original Directional Response (Dipole Pattern) of a Single Sensor in a Single Holder and (b) Modified Directional Response (Asymmetric Dipole Pattern) with Three Sensors in a Triangular Holder Producing Shadowing 13

Figure 5. (a) Computer Generated Model of the Triangular Sensor Array Mount (b) 3D Printed Sensor Holder with Installed Sensor Boards....14

Figure 6. Sensor Directional Response Showing Absolute Cosine Responses and Shadowing....15

Figure 7. Representative Dif/Sum Curves of Three Sensors Responses from Equations 3–5....16

Figure 8. Tangent Equations (10) and (11) Approximations to the Dif/Sum Curves 19

Figure 9. Fourth Order Polynomial Approximation to the Dif/Sum Curves....19

Figure 10. Piece-wise Polynomial Model of the Dif/Sum Curves 20

Figure 11. Representation of Alignment of Possible DOAs on a Sound Source 21

Figure 12. Algorithm Block Diagram 21

Figure 13. Angular Intervals Corresponding to Relative Magnitudes of Unaltered Sensor Responses....23

Figure 14. Dif/Sum Calibration Curves Overlaid on Angular Intervals 24

Figure 15. (a) DOA Determination for Ideal Sensor (b) Histogram of Error for Ideal Sensor....28

Figure 16. (a) DOA Determination for Sensor Array with 1 Hz Central Frequency Mismatch and 25 dB SNR (b) Histogram of Error for Sensor with 1 Hz Central Frequency Mismatch and 25 dB SNR 29

Figure 17. Representative Mismatched Frequency Response of Three Sensors.....30

Figure 18. Yuneec Typhoon 32

Figure 19. Optimum Correlation Band for Central Frequency Mismatch 33

Figure 20. (a) Central Frequency Mismatch Effect on DOA Determination with Optimized Correlation Band (b) Central Frequency Mismatch Effect on Error with Optimized Correlation Band 34

Figure 21. (a) SNR Effect on DOA Determination – 0 Hz Central Frequency Mismatch (b) SNR Effect on Error – 0 Hz Central Frequency Mismatch.....36

Figure 22. (a) SNR Effect on DOA Determination – 2 Hz Central Frequency Mismatch (b) SNR Effect on Error – 2 Hz Central Frequency Mismatch.....37

Figure 23. (a) Directional Noise Effect on DOA Determination – 0 Hz Central Frequency Mismatch (b) Directional Noise Effect on Error – 0 Hz Central Frequency Mismatch 39

Figure 24. (a) Directional Noise Effect on DOA Determination – 2 Hz Central Frequency Mismatch (b) Directional Noise Effect on Error – 2 Hz Central Frequency Mismatch 40

Figure 25. Frequency spectrum of one second of audio from: (a) Yuneec Typhoon – No Load (b) Yuneec Typhoon - Loaded with 940 g (c) Phantom 4 Pro – No Load (d) Phantom 4 Pro – Loaded with 940 g (e) Phantom 3 Pro – Loaded with 940 g (f) Mavic Pro (g) Matrice 600.....43

Figure 26. (a) Drone Type Effect on DOA Determination – 0 Hz Central Frequency Mismatch (b) Drone Type Effect on Error – 0 Hz Central Frequency Mismatch.....44

Figure 27. (a) Drone Type Effect on DOA Determination – 2 Hz Central Frequency Mismatch (b) Drone Type Effect on Error – 2 Hz Central Frequency Mismatch.....45

Figure 28. Unloaded Typhoon with 0.1 Hz Central Frequency Mismatch, 0.0° Directional Variation, and 25 dB SNR 46

Figure 29. Mavic Pro with 0.5 Hz Central Frequency Mismatch, 0.3° Directional Variation, and 25 dB SNR 47

Figure 30. Typhoon Loaded with 940 g with 2 Hz Central Frequency Mismatch, 0.3° Directional Variation, and 25 dB SNR.....47

Figure 31. Unloaded Typhoon with 0.1 Hz Central Frequency Mismatch, 0.0° Directional Variation, and 25 dB SNR with Calibration Curve Divisions 48

Figure 32. Polar Plot of Measured Dipole Directional Response 50

Figure 33. Measured Directional Response of Asymmetric Dipole Pattern Directional Response with Corresponding Angular Intervals 51

Figure 34. Asymmetric Dipole Pattern DOA Determination – No Introduced Noise 52

Figure 35. Error Histogram for Asymmetric Dipole Pattern DOA Determination – No Introduced Noise 53

Figure 36. (a) SNR Effect on DOA Determination for Measured Asymmetric Dipole Response – 0 Hz Central Frequency Mismatch (b) SNR Effect on Error for Measured Asymmetric Dipole Response – 0 Hz Central Frequency Mismatch 54

Figure 37. DOA Determination for an Asymmetric Dipole Directional Respones - 0 Hz Central Frequency Mismatch, 5 dB SNR 55

Figure 38. Polar Plot for Measured Cardioid Directional Response.....56

Figure 39. Measured Directional Response of Measured Cardioid Directional Response with Angular Intervals 57

Figure 40. Cardioid Response DOA Determination – No Introduced Noise.....58

Figure 41. Error Histogram for Cardioid Response DOA Determination – No Introduced Noise 59

Figure 42. (a) SNR Effect on DOA Determination for Measured Cardioid Response – 0 Hz Central Frequency Mismatch (b) SNR Effect on Error for Measured Cardioid Response – 0 Hz Central Frequency Mismatch.....60

Figure 43. DOA Determination for a Cardioid Directional Response - 0 Hz Central Frequency Mismatch, 5 dB SNR 61

Figure 44. Difference over the sum of two absolute cosine functions compared to a tangent function and its fractional reciprocal.....71

Figure 45. Shadowed sensor response Dif/Sum curves (where A>B) 75

Figure 46. Shadowed sensor response Dif/Sum curves (where A<B) 75

Figure 47. (a) SNR Effect on DOA Determination for Unloaded Typhoon – 10 Hz Central Frequency Mismatch (b) SNR Effect on Error for Unloaded Typhoon – 10 Hz Central Frequency Mismatch 77

Figure 48. (a) SNR Effect on DOA Determination for Unloaded Typhoon – 0.5 Hz Central Frequency Mismatch (b) SNR Effect on Error for Unloaded Typhoon – 0.5 Hz Central Frequency Mismatch 78

Figure 49. (a) Directional Variation Effect on DOA Determination for Unloaded Typhoon – 10 Hz Central Frequency Mismatch (b) Directional Variation Effect on Error for Unloaded Typhoon – 10 Hz Central Frequency Mismatch.....79

Figure 50. (a) Directional Variation Effect on DOA Determination for Unloaded Typhoon – 0.5 Hz Central Frequency Mismatch and SNR of 25 dB (b) Directional Variation Effect on Error for Unloaded Typhoon – 0.5 Hz Central Frequency Mismatch and SNR of 25 dB 80

Figure 51. (a) Drone Type Effect on DOA Determination for Unloaded Typhoon – 0.5 Hz Central Frequency Mismatch, SNR of 25 dB, and 0.3° Maximum Directional Variation (b) Drone Type Effect on Error for Unloaded Typhoon – 0.5 Hz Central Frequency Mismatch, SNR of 25 dB, and 0.3° Maximum Directional Variation 81

LIST OF ACRONYMS AND ABBREVIATIONS

AVS	acoustic vector sensor
CAS	continuous active sonar
DOA	direction of arrival
g	gram
MEMS	microelectromechanical system
PAS	pulse active sonar
SNR	signal-to-noise ratio
UAV	unmanned aerial vehicle

THIS PAGE INTENTIONALLY LEFT BLANK

ACKNOWLEDGMENTS

Many thanks to my advisor Dr. Fabio Durante Pereira Alves for his guidance and aid in developing this thesis beyond what I could have done alone. Thank you also to my co-advisor Dr. Gamani Karunasiri for his insights and his provision of the modeled sensor I used for analytical analysis. Finally, thank you to Dr. Renato Rabelo, who trained me in characterizing and testing sensors and their responses.

THIS PAGE INTENTIONALLY LEFT BLANK

I. INTRODUCTION

One of the recent advances in offensive capability is the development of small, unmanned aerial vehicles (UAV). Small, rotor powered UAVs have become commercially common in recent years as their technology has improved and lowered in cost [1]. Inevitably, these small UAVs have been weaponized and present a very real new category of threat, that demands a new category of sensors to specifically detect them. One potential device is an acoustic microelectromechanical system (MEMS) sensor inspired by the acoustic organ of the parasitic fly *Ormia* ochracea. This current research develops an algorithm using a *Ormia*-inspired MEMS sensor to detect the direction of arrival (DOA) of a small, rotor powered UAV.

A. BACKGROUND

1. *Ormia Ochracea* MEMS Sensor

The biomimetic acoustic sensors used in this study are based on the work of Miles et al. [2], whose seminal 1995 paper introduced the auditory organ of the parasitic fly *Ormia ochracea* and its unique sensory properties. The auditory organ is less than two millimeters in width, but can detect the direction of a cricket chirping at 5 kHz with a 2° accuracy [3]. By comparison, humans have a distance between their ears of about 9 centimeters and can determine the direction of a sound source with an accuracy of 3–10°, when tested with 100 millisecond white noise pulses [4]–[6]. The unique quality of the *Ormia ochracea* auditory organ is achieving such a high level of accuracy in such a small organ.

The *Ormia ochracea* organ responds to sound with a mechanical motion in two modes of vibration, rocking and bending. The organ's response is tuned to the frequencies of crickets' chirps, and the amplitude of the response is dependent on the direction of arrival (DOA) of the sound. This organ, and its modes of response, can be mimicked in a microelectromechanical system (MEMS) which can produce an electrical signal proportional to the angle at which the sound is received. Different design types of this device have been demonstrated [7]–[11], including a double wing device with interdigited

comb fingers with capacitive readout, which is the subject of this research. The sensor is tuned by design to the desired frequency band of operation. The sensor's footprint is only a few square millimeters and requires very low power to operate, making it very attractive to be used as an acoustic sensor for detection of drones in a field environment.

2. Threat from Small, Rotor Powered UAVs

The threat from small, rotor powered UAVs has risen considerably in recent years. Advances in smart flight controls, vehicle designs, and payload capacity for small, rotor powered UAVs have made them cheaper, easier to use, and more available [12]. With these advances have come an increased threat from using commercially accessible UAVs improperly. In 2015, a small, quadcopter style UAV crashed on the lawn of the White House, even though the house of the United States President is in a no-fly zone [13]. The threat from this incursion cannot be overstated. Since early 2015, ISIS has employed small, rotor powered UAVs, commercially purchased and homemade, to carry out bombings and to conduct surveillance on coalition forces in Iraq [14]. As commercially available drones become less expensive and more available, with longer range and higher weight capacities, terrorist groups have begun incorporating them into their arsenals. Terrorist groups have leveraged the mobility and low profile of small, rotor powered UAVs to conduct political attacks, such as the drone attack on Iraq's Prime Minister in 2021 [15], [16]. In this attack, three drones loaded with explosives were flown to the Prime Minister's home. Two were shot down, but the third made it through the defenses to explode outside the house, according to the news articles. This illustrates the threat of multiple drones penetrating defenses that would prevent attack by a single drone. It can be anticipated that attacks of this nature will become more commonplace and the need to defend against them will grow in parallel.

Other groups have used multiple small, rotor powered UAVs in their attacks. In January 2022, Houthi rebels in Yemen reportedly used UAVs to conduct an attack at an oil facility in Abu Dhabi and Abu Dhabi International Airport, killing three people and wounding six [17]. The type of UAV was not specified in news reports, but subsequently Yemen banned the use of recreational drone [18]. Attacks like this one and the ones in Iraq

emphasize the potential for small UAVs to be used in asymmetric warfare with deadly results.

UAVs have been used extensively by the world's militaries for a number of years, but the climate of UAV use has shifted. As drone technology has improved, UAVs have changed from airplane shaped vehicles manufactured by the military-industrial complex to small, rotor powered UAVs that are commercially available for only a few hundred dollars.

Advancements in computing have also progressed drones to take on more autonomous roles. March 2020, during a Libyan conflict, marks the first time a drone selected a target and conducted an attack against that target without input from a human operator, when an attack drone manufactured by a Turkish company, was used by government forces against rebels in the country [19]. As artificial intelligence and autonomous systems grow in capability, it is likely that autonomous UAVs will become more prevalent. A United Nations convention discussing the banning of autonomous weapons chose not to ban autonomous weapons at this time, leaving the door open for further development of UAVs controlled autonomously [20]. This advanced capability makes possible advanced computing to control the movement and offensive ability of small UAVs.

In addition to individuals and asymmetric warfare groups, first world nations are leveraging the capabilities of small, rotor powered UAVs. The largest advance in UAVs that make them a viable weapon for national militaries builds on the advances in autonomous control and multiple UAV attack; the drone swarm. The offensive capability of drone swarms, with their ability to deploy a host of UAVs carrying explosives and chemical or biological attacks, especially combined with autonomous controls, can make drone swarms a devastating weapon [21]. Nations have incorporated this offensive capability into their militaries. Starting in 2020, Turkey acquired 500 small, rotor powered UAVs with swarming capabilities that are described as "kamikaze drones" [22]. China has demonstrated a small, truck launched, rotor powered small, multi-rotor UAV with a swarm capability of 48 drones, equipped with explosive heads that are potentially powerful enough to penetrate armored vehicles [23]. Likewise, the United States has contracted production of a small, swarm capable UAV since at least 2018 [24]. Israel has made use of

small, quadcopter style UAVs in combat possessing swarm capabilities, with reports that some of the drones are capable of carrying explosives [25]. If these nations are any indication of the future, warfare involving UAVs or fully autonomous drones will only become more prevalent.

The advantage of small, rotor powered UAVs is not only in their maneuverability, commercial availability, and low cost, but in their ability to evade detection. Radar absorbing materials and their small size make small UAVs hard to detect by radar, and when they are detected, they may be mistaken for birds or other clutter [26], [27]. In addition, the Department of National Defence of Canada also identified small, rotor powered could be carried in backpacks covertly to the site of an attack [26]. The low profile of small, rotor powered UAVs makes them easy to use as an asymmetric warfare weapon and difficult to defend against. Radar is often relied upon for targeting by the military, but the very nature of small, rotor powered UAVs makes them hard to detect by radar [27]. Other detection means would be beneficial for layered defense against small, rotor powered UAVs.

3. Status of Research

The *Ormia*-inspired MEMS sensor has been well studied since the first 1995 paper and its properties, mathematical models, and different approaches to fabrication have been well published [1], [7]–[11]. The focus of this thesis will be on the application of the sensor to determine the DOA of an acoustic source of interest. The algorithms used by different research teams to use the response of their sensor in determination of the DOA are discussed in this section.

a. Ormia Ochracea Inspired MEMS Sensors

Rahaman and Kim [28] used piezoelectric materials to measure the response of their *Ormia*-inspired MEMS device. The device used the ratio of the measured voltage output of the system relative to the response at a specified reference angle, divided by the summed response of both wings relative to the response at the same specified reference angle. This ratio forms a cosine function, which allows the DOA to be directly solved based on the magnitude of these responses.

The paper reports a directional error of 0–7.05°, with minimum error on the +90° major axes and maximum error at +30° from this axis. The sensor assembly covered a range of 360°. Left-right ambiguity was solved by comparing the responses from each wing, whichever wing had the higher response was on the side of the source emission.

Rabelo et al. [29]. used an interdigitate comb capacitive MEMS device with capacitive readout to estimate the DOA of a single frequency acoustic source. The authors used the measured difference in phase angle, based on the direction of the sound source, between the two wings of a single *Ormia*-inspired MEMS device to estimate the DOA over an arc of 180°. This phase difference based on angle was established by closing the back side of the sensor, except for a small slit to control the air exchange in the cavity. This configuration was used to increase the coupling between the bending and rocking modes of the sensor and resulting in a pronounced phase shift dependent on the angle of the acoustic source. A high degree of directionality was estimated with this technique with an angular resolution of better than 3° for sound pressure levels greater than 42 dB (relative to 20 microPascals). The technique did not resolve bearing ambiguity.

Liu et al. [30]. mathematically simulated a four microphone, three-dimensional array for sound source localization. The four microphones were modeled as if placed on what would be the axes of a Cartesian coordinate system, with the fourth microphone at the origin, as shown in Figure 1.

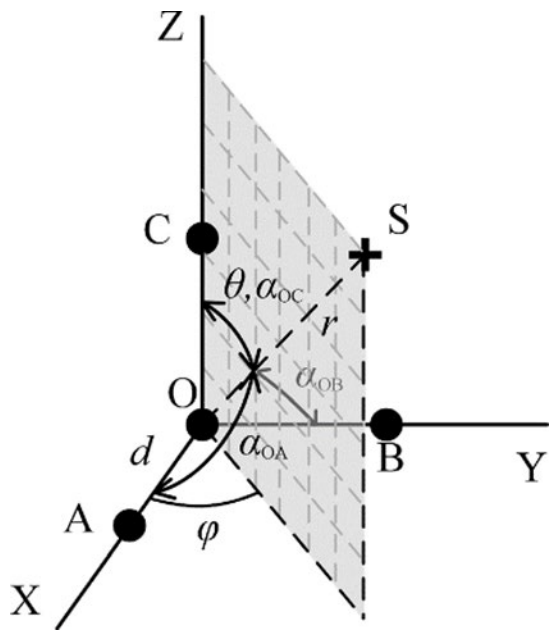

Figure 1. Three-Dimensional Orientation of Four Microphone Array from Liu et al. Source: [30].

The time delay difference between each microphone on the three axes and the microphone at the origin is used to calculate the incident angle relative to each pair of sensors. With three calculated incidence angles, both the elevation and azimuth of the acoustic source are determined and ambiguity is inherently resolved. The authors did not report figures of merit for the system, but data presented shows the sound source was localized within a few degrees for both elevation and azimuth.

The current effort of this paper builds on results from Wilmott et al. [31], where a pair of canted *Ormia*-inspired sensors were used to solve for DOA using an arctangent function. As the sound source rotates around the sensor, it forms an absolute cosine function for each individual sensor. The difference between these sensor responses, divided by the sum of their responses, can be resolved to a tangent function from which the DOA can be determined.

$$\frac{V_L/\propto_L - V_R/\propto_R}{V_L/\propto_L + V_R/\propto_R} = tan\left(\theta_{off}\right) tan(\theta) \tag{1}$$

for $-90° + \theta_{off} \leq 90° - \theta_{off}$

Here, θ_{off} is the deviation angle between the canted sensors, V_L is the voltage produced by the left canted sensor, V_R is the voltage produced by the right canted sensor, and α_R and α_R are calibration constants to equalize the response between the two sensors. The configuration of Wilmot et al. was limited to a range of -60° to +60° with a $\theta_{off} = 30°$ and reported a maximum error of 3.4°. This configuration used by the authors did not provide unambiguous 360° azimuth coverage. This thesis builds on this effort to obtain full azimuthal coverage.

b. Cilia Inspired MEMS Vector Sensors

Another promising DOA sensor is also biomimetic in nature, using cilia MEMS structures based on the lateral line organs of fish. Algorithms for analyzing the outputs of these sensors are similar in many ways to the algorithms used to solve for DOA in *Ormia*-inspired sensors. Although these sensors were demonstrated in hydrophones, review of these sensors is useful to compare accuracy and computational methods, as these same methods could also be used in sensors used in air.

Shang et al. [32], analyzes a cilia MEMS vector hydrophone consisting of a suspended cilium structure which moves as sound pressure acts on it. Piezoresistors are attached to this cilium at right angles to each other in a single plane. The deformation of these piezoresistors changes their resistance, which can be read as an electrical signal. DOA is determined by a beam forming tangent function, where the maximum value of the beam is oriented to the DOA. The tangent function is of the form

$$\Theta = atan\left(\frac{\sin(\ sensor\ signal)}{\cos(\ sensor\ signal)}\right) \tag{2}$$

Ambiguity is resolve by a phase shift analysis. The paper reports the average error is less than 5°.

Liu et al. [33]. expands on the cilia-inspired MEMS vector hydrophone to use four of them in a single plane in a single device, oriented at 15° increments to each other from 0–60°. The four cilia-inspired MEMS hydrophones were built onto a single circuit board, spaced at intervals of 16 millimeters from each other at the four corners of a square. The purpose of this research was to develop a unique way of resolving left-right ambiguity. Each individual sensor retains its ambiguity, but the individual DOAs for each sensor will only align in a single direction.

The advantage of this method is not only is ambiguity resolved, but the triangulation of the four sensors provides a range as well. The test was limited in size to a small laboratory experiment of less than 2.5 meters, but reports errors between 0.010° and 0.203° at -194 ±1 dB (@500 Hz, 0 dB ref 1 V/uPa). The four sensor cilia hydrophone covered a range of 360° and innately solved for directional ambiguity.

c. Acoustic Vector Sensors (AVS)

Another prevalent class of acoustic sensors used for sound localization is AVS. The Microflown AVS uses two platinum wires heated to approximately 300° Celsius and an omnidirectional microphone to produce its output signals [34]. As sound pressure affects the air flow between the two sensors, there is a cooling effect that can be read as an electrical signal proportional to the air velocity, as described in the same article. These vectors can be resolved to velocity vectors, acceleration vectors, and pressure vectors [35]. There are numerous computational algorithms for determining DOA based off these vectors, but the simplest is an intensity based tangent function, in either the time domain or the frequency domain, [36], [37] similar to the tangent function algorithms for *Ormia*-inspired MEMS sensors and cilia-based MEMS sensors described in the previous section. Comparison to the methods and accuracy of AVS sensors is useful to evaluate the performance of *Ormia*-inspired sensors.

Novo [36] outlines several algorithms for calculating DOA from the AVS vector outputs, including time domain intensity based tangent estimator and a frequency domain intensity based tangent estimator, as well as other advanced computational methods. Ambiguity was resolved using the complex acoustic intensity which retains phase

information in reference to an omnidirectional microphone. The average errors reported in Novo [36] were 3.43° in the time domain algorithm and 1.84° in the frequency domain algorithm. These results were further improved by calibration and by using filters down to average errors of 1.90° and 1.71° respectively. The lowest error reported by Novo was for the calibrated Capon beamforming algorithm, with an average error of 1.33°.

Terracciano et al. [37]. experimented with the use of AVS in hydrophones for detecting active sonar, using a tangent based algorithm against both a continuously active sonar (CAS) and a pulse active sonar (PAS). The tangent-based estimator calculated the DOA of the sonar using the arctangent of the ratio between sine and cosine components of the vector sensor output. The paper reports results for PAS in the time domain with a mean error of 4.64° and in the frequency domain with a mean error of 5.35° with a standard deviation of 5° for both domains. For CAS, Terracciano et al. reported a mean error in the time domain of 0.58° and in the frequency domain of 0.1° with a standard deviation of the error of 5.85° and 4.68° respectively. Error and standard deviation of the error for CAS was found to be reduced by selection of sub-bands within the acoustic signature, via band-pass filtering of the fast Fourier transformed signals. By this method, the standard deviation of the error was reduced to 2.07° for the time domain and 3.29° for the frequency domain.

B. OBJECTIVE AND THESIS ORGANIZATION

The objective of this thesis is to use the existing sensor from previous research and develop a computational algorithm for determining DOA of a small, rotor powered UAV. A sensor housing and array configuration will be developed to obtain the desired directional response. The quality of DOA determination will be analyzed as a function of time needed to compute the determination, with a goal of readouts within one second. Design and experimentation will be conducted to achieve unambiguous, 360° coverage in azimuth and determine the level of accuracy.

Section I of this thesis introduces the background to the thesis topic, with a discussion on how the technology emerged and the current status of research and varying methods for accomplishing DOA determination. The benefits of this current thesis are discussed in the context of these other research efforts. Section II of the thesis discusses

the design of the sensor array structure and the computational method that allows for DOA determination. Section III lays out the design of the analytical tests and the results from those tests, including the algorithm's response and performance at different levels of testing parameters. Figures of merit are established for directional error of the sensor array at varying signal to noise ratios (SNR), frequency mismatch between sensors, noise in the directional patterns of the sensors, and for various drones. The thesis concludes with a summary of the results and recommendations for future work.

II. SENSOR DESCRIPTION AND DOA ESTIMATION METHOD

In this research study, the DOA of the incoming acoustic signal is estimated using three *Ormia*-inspired sensors to provide 360° azimuthal coverage. The sensors' output is manipulated and compared with a pre-generated calibration curve to determine the DOA. The sector of arrival is first determined by comparison of the magnitudes of the incoming signal. Ambiguity is resolved by the asymmetric characteristic of the dipole-like directional response of individual sensors. The signals from each pair of sensors are used to calculate a difference over the sum of the two signals and this value is compared to the calibration curve to find the estimated DOA.

A. SENSOR ARRAY DESCRIPTION

The *Ormia*-inspired MEMS sensors used in this research, consist of two freestanding wings connected by a thin bridge, with the entire structure attached to a substrate using two torsional legs, perpendicular to the bridge. Figure 2 shows the schematic diagram of a typical sensor designed by our research group.

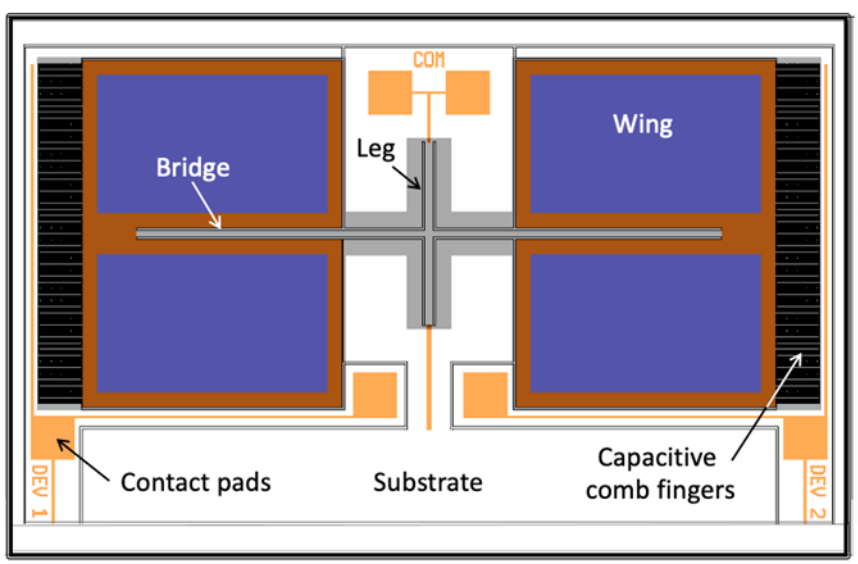

Figure 2. Schematic Diagram of a Typical *Ormia*-inspired Sensor Designed by Our Research Group

The sensor wings vibrate in and out of the substrate plane due to the incident sound pressure. The two predominant vibration modes of the mechanical structure of the sensor are bending and rocking of the wings of the sensor [31]. The wings' displacement amplitudes are a function of the incident sound frequency, sound pressure level, and DOA. The directional response of individual sensors, in the bending mode, resembles the radiation pattern of a dipole antenna (a figure-8 pattern), similar to a pressure gradient microphones. Figure 3 shows the simulated frequency response of a typical sensor (a) as well as its measured directional pattern when excited in the bending mode (b).

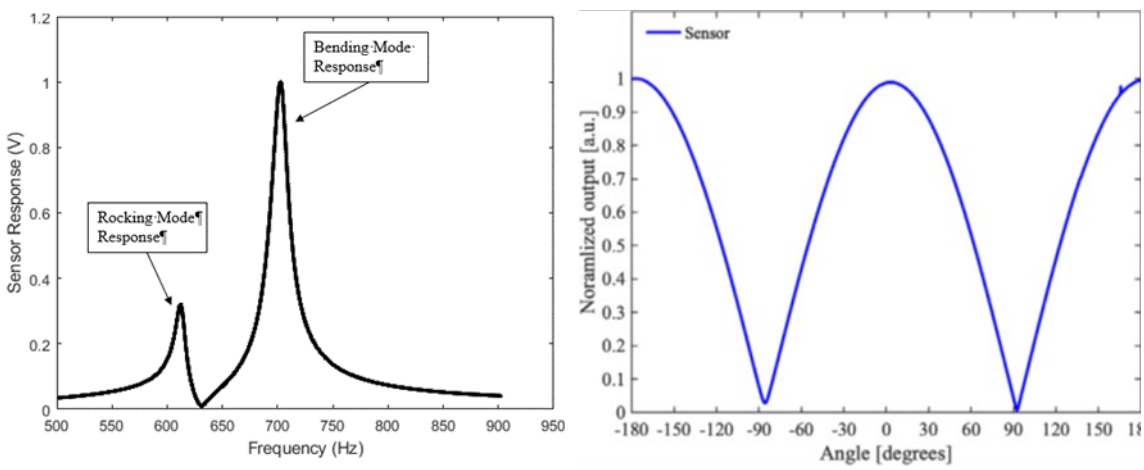

(a) (b)

Figure 3. (a) Simulated MEMS Sensor Frequency Response. (b) Measured MEMS Sensor Directional Pattern at the Sensor's Bending Frequency from Wilmott et al. Source: [31]

To resolve the azimuthal ambiguity, it is necessary to modify the individual directional response by reducing one of the two lobes of the dipole pattern with relation to the other, similar to a super cardioid [38] (asymmetric dipole pattern) as shown schematically in Figure 4 (b). The pattern modification can be used to resolve ambiguities by indicating from which direction an acoustic signal is arriving due to the decrease in magnitude from the opposite side of the sensor. This effect is similar to the way human hearing resolves ambiguity [4]–[6].

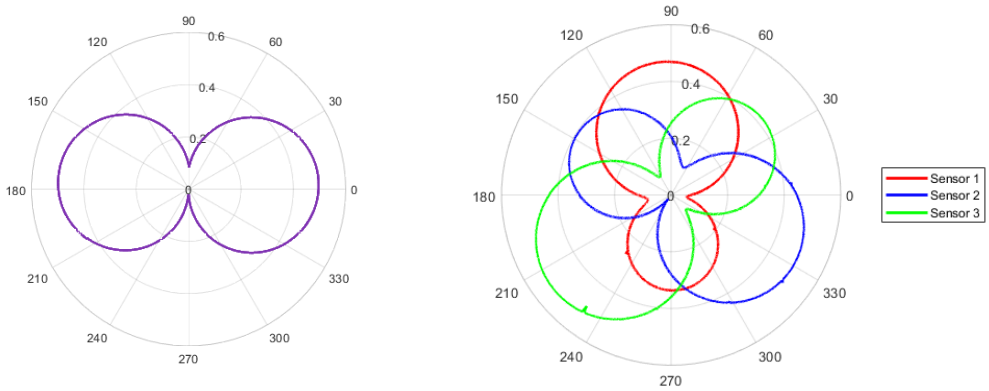

(a) (b)

Figure 4. (a) *Ormia*-inspired Bending Mode Original Directional Response (Dipole Pattern) of a Single Sensor in a Single Holder and (b) Modified Directional Response (Asymmetric Dipole Pattern) with Three Sensors in a Triangular Holder Producing Shadowing

Conceptually, this can be done by reducing the aperture on one side of the sensor, either the front or back. This is well documented in [38]. Several geometric configurations were tested with all three sensors together to obtain individual asymmetric dipole directional patterns. The senor mounts were 3D printed with polylactic acid using a MakerBot Method X and the directional response of all three sensors were measured simultaneously. The triangular sensor mount that provided the desired pattern (asymmetric dipole pattern) is shown in Figure 5.

With the influence of the housing configuration, the three sensor responses together form a unique pattern for each sector, which can be used to determine the sector from where the sound is coming and ultimately estimate the DOA.

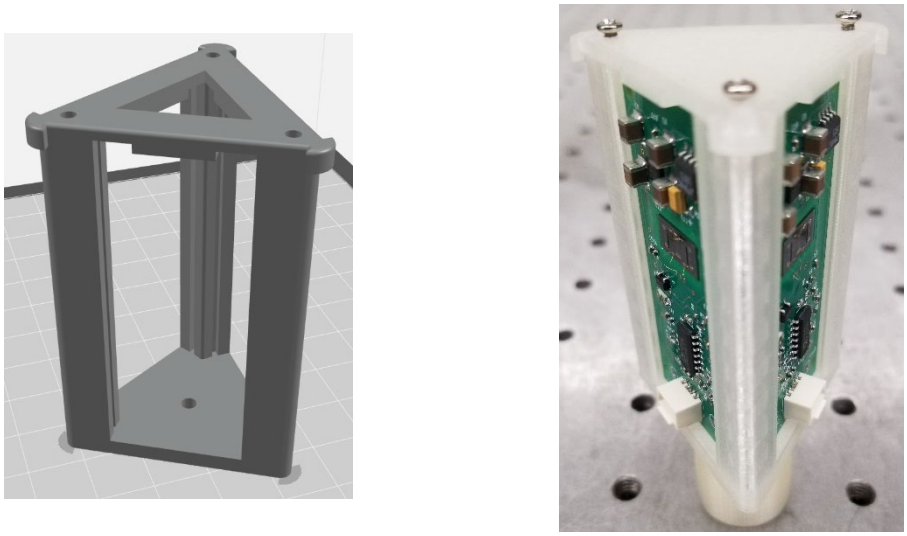

(a) (b)

Figure 5. (a) Computer Generated Model of the Triangular Sensor Array Mount (b) 3D Printed Sensor Holder with Installed Sensor Boards

The output of the sensor array provides three signals proportional to the incident sound pressure level and weighted by the directional characteristic of each sensor. The DOA determination is made by manipulating the signal output to remove the dependence on the sound pressure level by normalizing the signal differences between sensors by their sum. This is performed in pairs of canted sensors, allowing for an unambiguous determination over 360° in azimuth.

1. Mathematical Model of the Sensor Array Response

The signal produced by the *Ormia*-inspired MEMS sensor produces a response similar to the modulus of a cosine function over 360°, where the vector corresponding to the direction of the sensor is normal to the plane of the sensor. At normal incidence, the output signal is at a maximum, the same as a cosine function evaluated at zero degrees, and

at 90° incidence, the response is at a minimum. Due to the open back of the sensor, this pattern repeats on the back side hemisphere, as shown in Figure 6. Figure 6 was produced by measuring the response of a sensor array due to a single tonal signal at 688 Hz, measured over a 360° rotation. Notice that the back side response is reduced due to the housing of the sensors, as previously discussed.

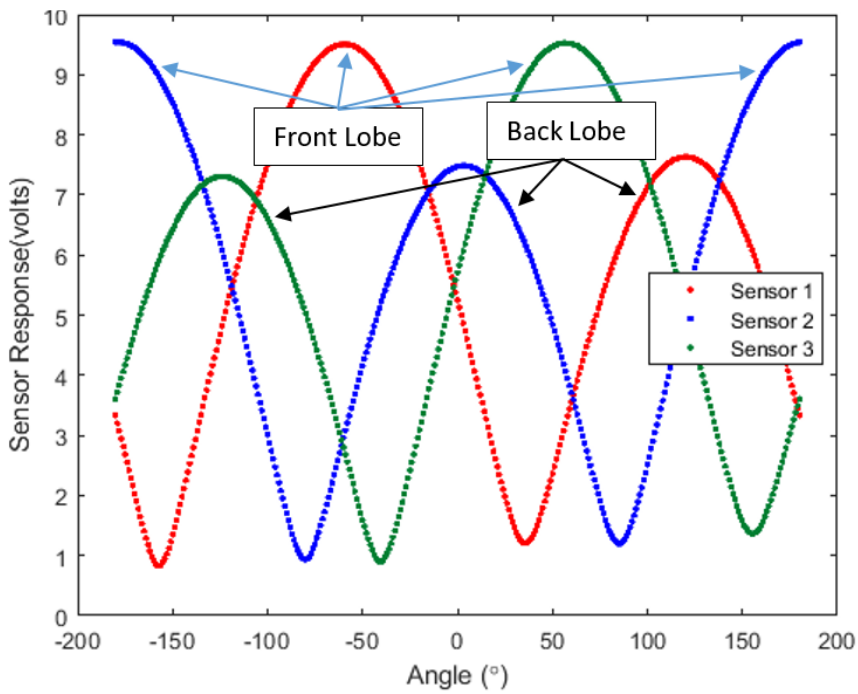

Figure 6. Sensor Directional Response Showing Absolute Cosine Responses and Shadowing

The signal outputs from adjacent sensors are used to obtain the difference over the sum of each pair, as seen in Equations 3–5.

$$DS_{12} = \frac{S_1 - S_2}{S_1 + S_2} \tag{3}$$

$$DS_{23} = \frac{S_2 - S_3}{S_2 + S_3} \tag{4}$$

$$DS_{31} = \frac{S_3 - S_1}{S_3 + S_1} \tag{5}$$

S_1, S_2, and S_3 are the raw output of the three sensors and DS is the difference over the sum (Dif/Sum) of the sensors denoted in subscripts. Note that the signal output from the sensors depend on the incident sound pressure level, however the Dif/Sums do not. Six equations can be obtained by the permutation of the three sensors, but three of the equations are the negative correspondent of the other three and are ignored. These Dif/Sum curves are shown in Figure 7.

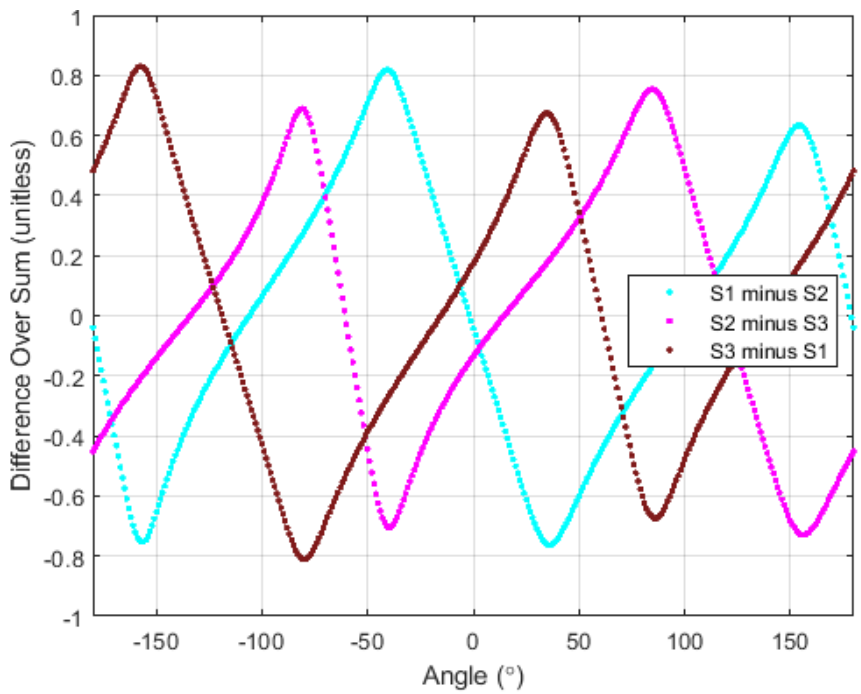

Figure 7. Representative Dif/Sum Curves of Three Sensors Responses from Equations 3–5

Using trigonometric identities, Equation 3 can be expressed as a tangent function of the form:

$$DS_{12} = \tan\left(\theta_{offset}/2\right) \tan\left(\theta + \theta_{offset}/2\right) \tag{6}$$

$$\text{for } -90° \leq \theta \leq -30° \text{ and } 90° \leq \theta \leq 150° \text{ when } \theta_{offset} = 120°$$

$$DS_{12} = \frac{1}{\tan\left(\theta_{offset}/2\right)\ \tan\left(\theta + \theta_{offset}/2\right)} \tag{7}$$

$$\text{for } -30^\circ \le \theta \le 90^\circ \text{ and } 150^\circ \le \theta \le -90^\circ \text{ when } \theta_{offset} = 120^\circ$$

where θ_{offset} is the deviation angle between sensors 1 and 2 and θ is the DOA of the acoustic signal. This function repeats periodically every 180° when the offset between the sensors is 120°. The derivation of Equation 6 is shown in Appendix A.

The DOA can be estimated as:

$$\theta = \operatorname{atan}\left(\frac{DS_{12}}{\tan\left(\theta_{offset}/2\right)}\right) - \frac{\theta_{offset}}{2} \tag{8}$$

$$\text{for } -90^\circ \le \theta \le -30^\circ \text{ and } 90^\circ \le \theta \le 150^\circ \text{ when } \theta_{offset} = 120^\circ$$

$$\theta = \operatorname{atan}\left[\frac{1}{\tan\left(\theta_{offset}/2\right) DS_{12}}\right] - \frac{\theta_{offset}}{2} \tag{9}$$

$$\text{for } -30^\circ \le \theta \le 90^\circ \text{ and } 150^\circ \le \theta \le -90^\circ \text{ when } \theta_{offset} = 120^\circ$$

The starting basis for this Dif/Sum tangent estimator is the absolute cosine like response of the *Ormia*-inspired sensor. However, as can be seen in Figure 6, the cosine trend fails near the minimums of each sensor, presenting as an acute curve instead of a sharp discontinuity. This can be attributed to the coupling between bending and rocking modes. The rocking vibration is much smaller than the bending for open back sensors as seen in Figure 3(a). The small peak at approximately 610 Hz is due to the rocking mode, compared to the large peak at approximately 700 Hz from the bending mode. However, the rocking mode peaks at 90°, where the bending mode is minimum and the rocking mode is asymmetric, causing the deviation from the cosine model. This means that even when the sensor is oriented at 90° to the acoustic source in the horizontal plane, it does not have a zero output. The modified dipole directional pattern also affects the values of the minima observed in Figure 6. Nevertheless, each Dif/Sum curve is unique regardless of the signal

output at the minima. The difference between minima of the raw sensor data only affects the values of the minima and maxima of the Dif/Sum curves shown in Figure 7.

The modification in directional pattern caused by the shadowing on the back of each sensor by the housing is necessary to resolve ambiguity, but it produces a change in curvature of the Dif/Sum curves. In this case, Equations 6 and 7 need to be modified. It was found that the introduction of a coefficient (a), a phase angle shift (b), and an offset variable (c) into each tangent term of Equations 6 and 7 was sufficient to compensate for the modified directional pattern. The modified equations take the form of

$$DS_{12} = a\tan(\theta + b) + c \tag{10}$$

$$DS_{12} = \frac{1}{a\tan(\theta + b) + c} \tag{11}$$

Derivation of these equations is found in Appendix B. The constants a, b and c in Equations 10 and 11 can be found by curve fitting the experimental data. These equations are still periodic, but the period is no longer 180°. Instead, the length of the arcs where these equations hold true are unique to the modified directional responses.

A series of fittings using Equations 10 and 11 were made using simulated directional responses of the sensor array. As can be seen in Figure 8, the fittings are not accurate near the inflection points.

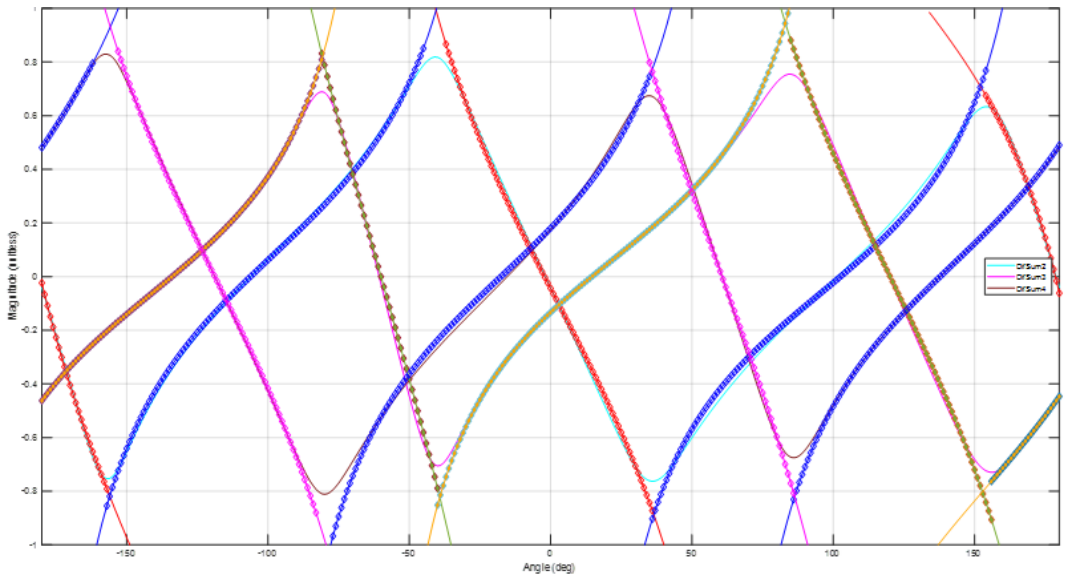

Figure 8. Tangent Equations (10) and (11) Approximations to the Dif/Sum Curves

A different approach was attempted using a piecewise polynomial curve fit (15 different polynomials). Modeling with fourth order polynomial equations, as seen in Figure 9, was found to be significantly more accurate, but also breaks down at the inflection points.

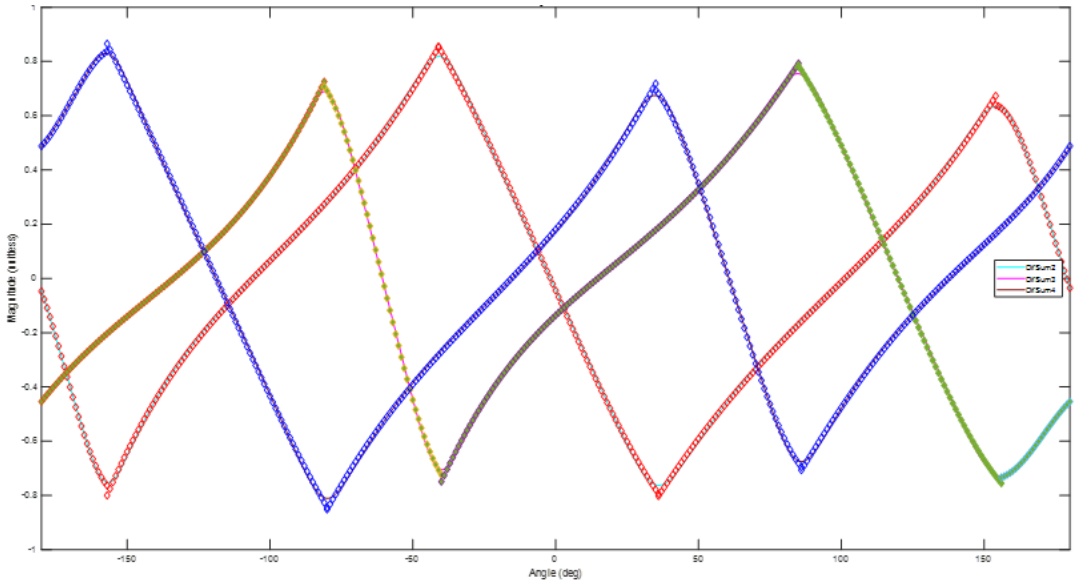

Figure 9. Fourth Order Polynomial Approximation to the Dif/Sum Curves

This fourth order polynomial provides four possible solutions for each individual sloped line, and these four solutions would need to be further analyzed to obtain the correct DOA.

Although use of either the tangent equation estimator or the polynomial equation estimator methods would substantially reduce computation time, there are markedly 12 regions, near the inflection points, over a 360° azimuth where the estimated DOA would be certainly inaccurate. To overcome these problems, Dif/Sum curves were modeled using a piecewise fitted polynomial using a cubic interpolation [39], as shown in Figure 10. This fitted curve was used to generate a high resolution, evenly spaced calibration curve for use in estimating the DOA.

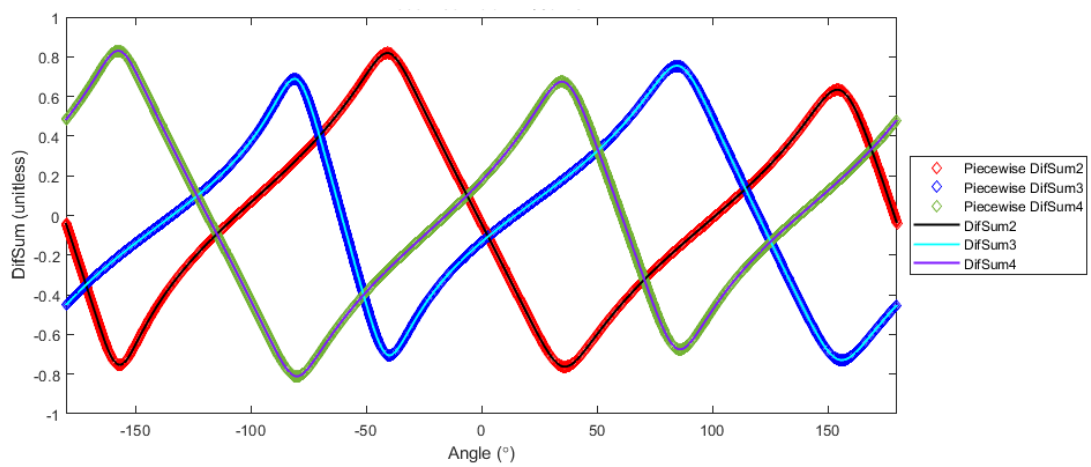

Figure 10. Piece-wise Polynomial Model of the Dif/Sum Curves

2. DOA Estimation Method

The DOA estimation method for this sensor array compares measured sensor outputs to a calibration curve of possible expected responses. Because the comparison will yield multiple possible computed DOAs for each Diff/Sum curve, results for all three Diff/Sum curves should be compared. The direction with highest correlation, as represented graphically in Figure 11 represents the correct DOA.

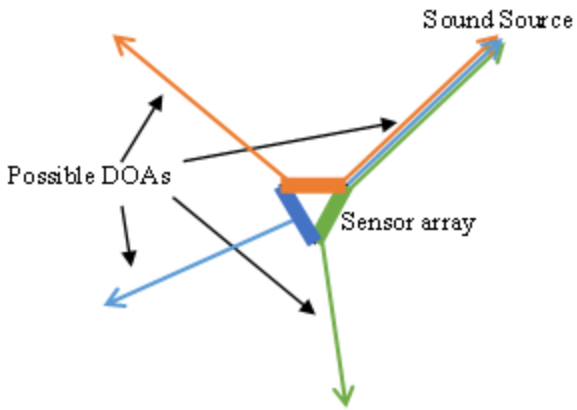

Figure 11. Representation of Alignment of Possible DOAs on a Sound Source

The algorithm for estimating the DOA is summarized in Figure 12.

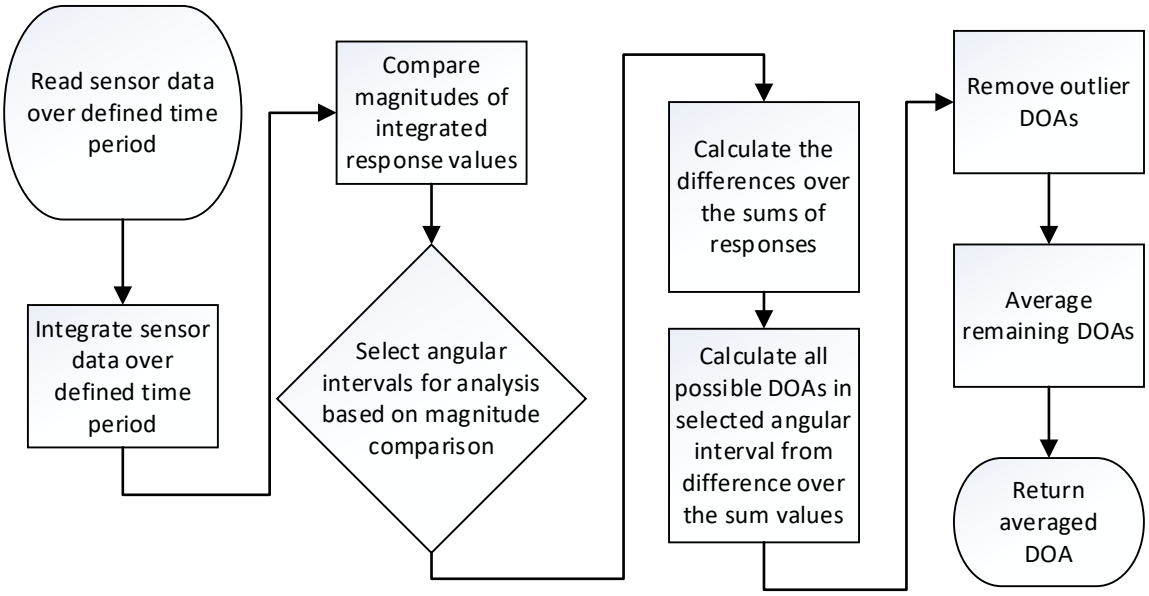

Figure 12. Algorithm Block Diagram

A calibration curve is generated to record the known sensor array directional response over the entire azimuth range. This calibration curve was obtained for the sensors stimulated with a single tone at their resonant frequency over a continuous 360° rotation

of the array. The difference over the sum of each pair of sensors forms the calibration curve to which future readings will be compared to estimate the DOA.

The steps to the algorithm are outlined as follows.

1. Acoustic sensor outputs are recorded over a defined time period by each sensor individually (0.5 to 1 s).
2. The time series of each sensor is integrated over that time period to reduce the effects of noise and potential fluctuations of the acoustic source. The integrated values are the input to the DOA determination algorithm.
3. The three sensor responses are ranked by magnitude in relation to each other. The corresponding angular intervals on the calibration curve where the sensor input values are also in the same order of relative magnitude are selected for further analysis. These angular intervals are shown in Figure 13 as the different colored regions corresponding to the intersections of the three sensor responses. Note the ambiguity between like-colored intervals. Even though the asymmetry of the dipole pattern of each sensor can create unique sensor responses in these areas, the relative order of the magnitudes in these regions are identical. Inspection of the directional patterns in Figure 13 indicate that if the asymmetry between front and back lobes is increased or if the back lobe is fully suppressed (cardioid-like pattern), these ambiguous regions would disappear, making this algorithm more reliable.

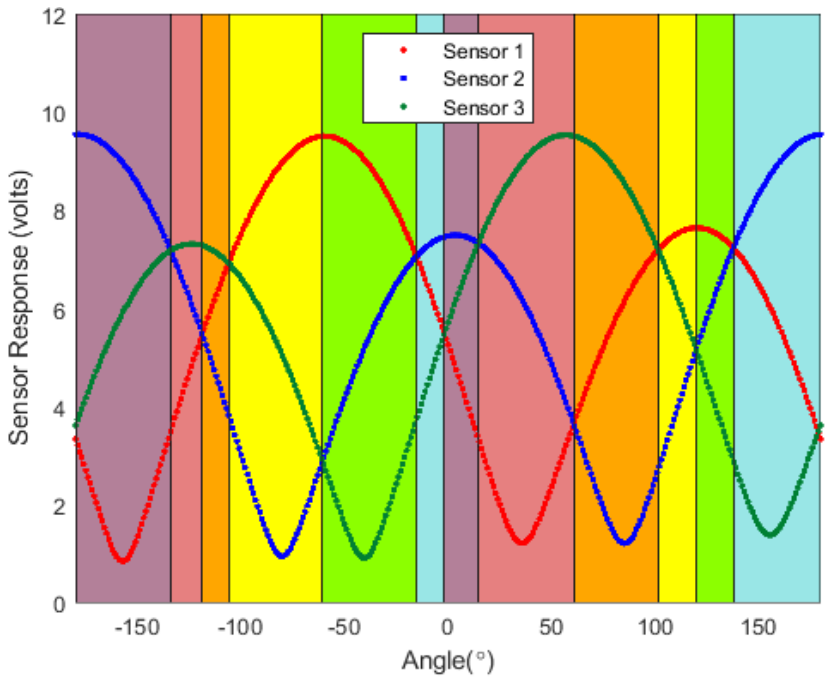

Figure 13. Angular Intervals Corresponding to Relative Magnitudes of Unaltered Sensor Responses

4. The three sensor responses are used as the inputs in Equations 1–3 to determine three Dif/Sum values.

5. These three Dif/Sum values are located, using a nearest neighbor algorithm [40], on the selected angular intervals of the calibration curves, shown in Figure 14, resulting in multiple possible DOAs.

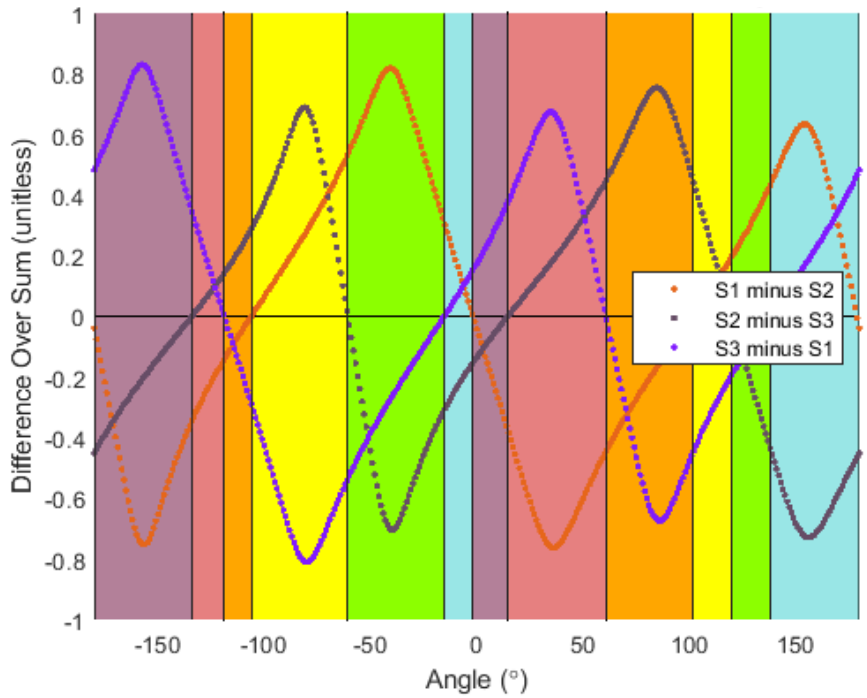

Figure 14. Dif/Sum Calibration Curves Overlaid on Angular Intervals

6. The multiple possible DOAs are compared with one another, and DOAs whose differences are within a pre-specified angular interval (correlation band) are selected for further analysis.

7. Outliers were removed from this selection of possible DOAs by performing two rounds of outlier removal using a standard outlier removal function in Matlab [41]. This removes possible DOAs that are not grouped with the majority of possible DOAs that were calculated.

8. The remaining DOAs after the two rounds of outlier removal are averaged to provide the final DOA estimation.

9. In some instances, due to noise and other errors, there may be an equal number of possible DOAs that align with each other. In these instances, both possible DOAs are reported as ambiguous.

To reduce computation, a simple magnitude comparison of the raw sensor data is performed to find the two possible angular intervals (see Figure 13) for the acoustic source.

This initial check removes potential for erroneously locating the estimated DOA in angular intervals where it cannot exist and lowers computation time by limiting the number of potential DOAs to which it must be compared.

Two DOAs are possible from each selected angular interval of the Dif/Sum curve and there are three Dif/Sum curves, one from each pair of sensors, thus, there may be as many as six possible DOAs that can be calculated. These multiple DOAs should only align on the correct DOA.

THIS PAGE INTENTIONALLY LEFT BLANK

III. ALGORITHM EXPERIMENTAL RESULTS

The algorithm developed, described in Section II, was tested to determine how reliably and accurately the DOA of a small UAV can be determined. The tests were conducted using recorded acoustics from commercially available drones as surrogates for small, rotor powered UAVs.

A. MODELED ALGORITHM RESPONSE AND FIGURES OF MERIT

Testing of the sensor array and algorithm was conducted using the simulated frequency and directional responses of the *Ormia*-inspired MEMS sensors, shown in Figure 3(a) and Figure 6, respectively. These sensor outputs to the acoustic stimulus were obtained by the convolution of the Fourier transform of a one second time series sample of drone audio by the frequency response of the sensors in the sensor array, shown in Figure 3(a). These sensor outputs were then weighted, angle by angle, by the directional curve of the sensor, shown in Figure 6. This total signal was summed, resulting in the total signal received by the sensor as a function of the frequency response of the sensor and the directional response of the sensor array. This total integrated signal was the input to the algorithm for the determination of the DOA.

Representative results for the algorithm are displayed in Figures 15 and 16. Error plots show show error values of less than ten degrees to examine in detail the angles where the algorithm works well. Accounting for the large error values is handled separately and discussed in detail below. Figure 15 shows the ideal case for the sensor, with no introduced error. Figure 16 shows the DOA determination when several types of potential perturbations (noise) are introduced.

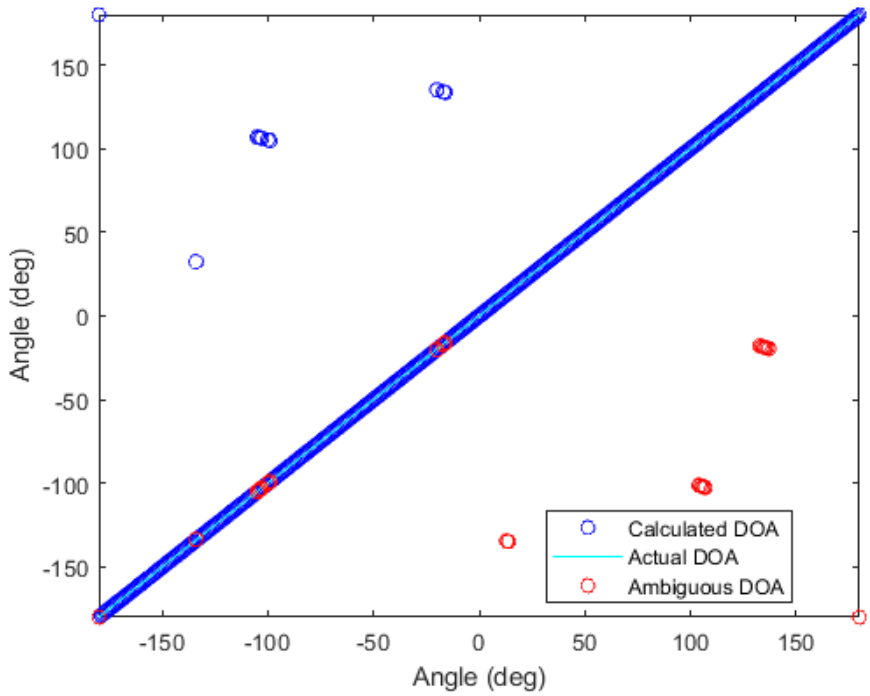

(a)

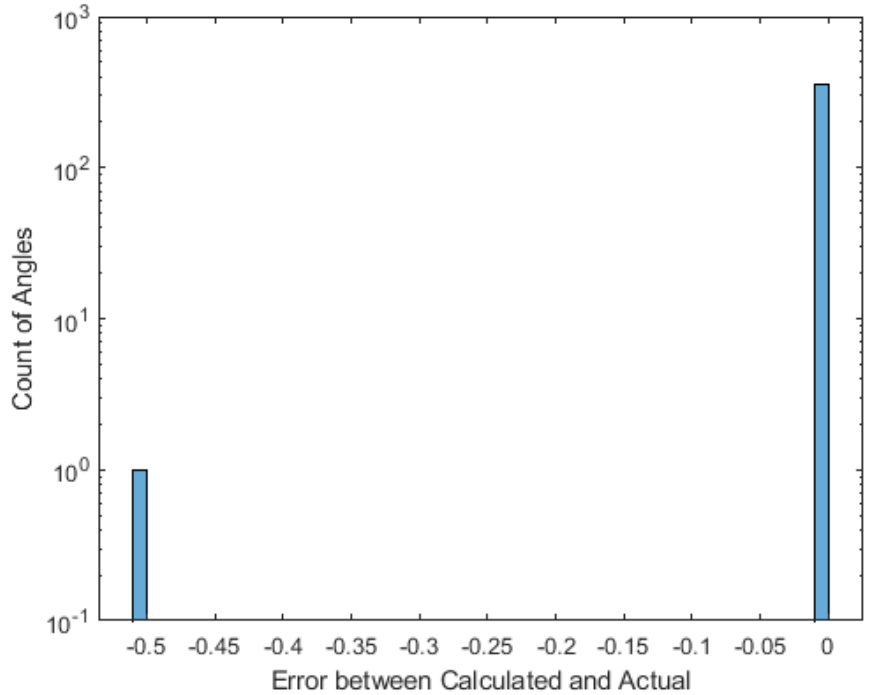

(b)

Figure 15. (a) DOA Determination for Ideal Sensor (b) Histogram of Error for Ideal Sensor

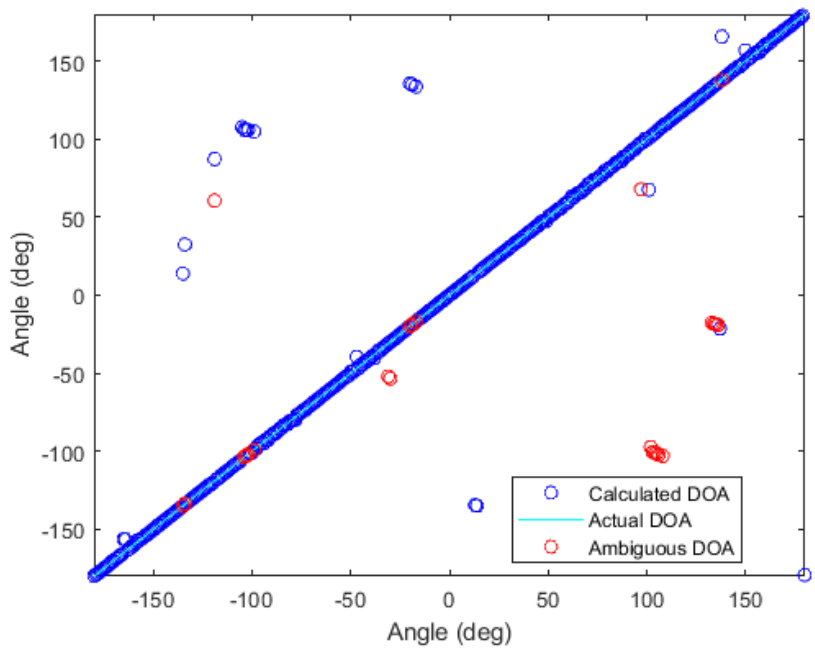

(a)

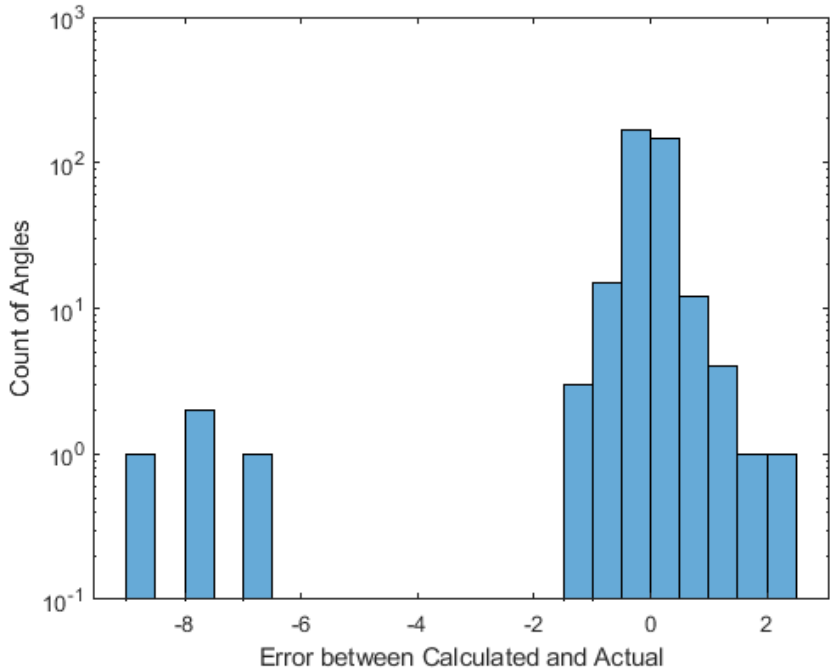

(b)

Figure 16. (a) DOA Determination for Sensor Array with 1 Hz Central Frequency Mismatch and 25 dB SNR (b) Histogram of Error for Sensor with 1 Hz Central Frequency Mismatch and 25 dB SNR

To examine the performance of the algorithm, four test variables were chosen over which to test the determination of the DOA. The first test variable was the mismatch in central frequency response between sensors due to manufacturing tolerances as represented in Figure 17.

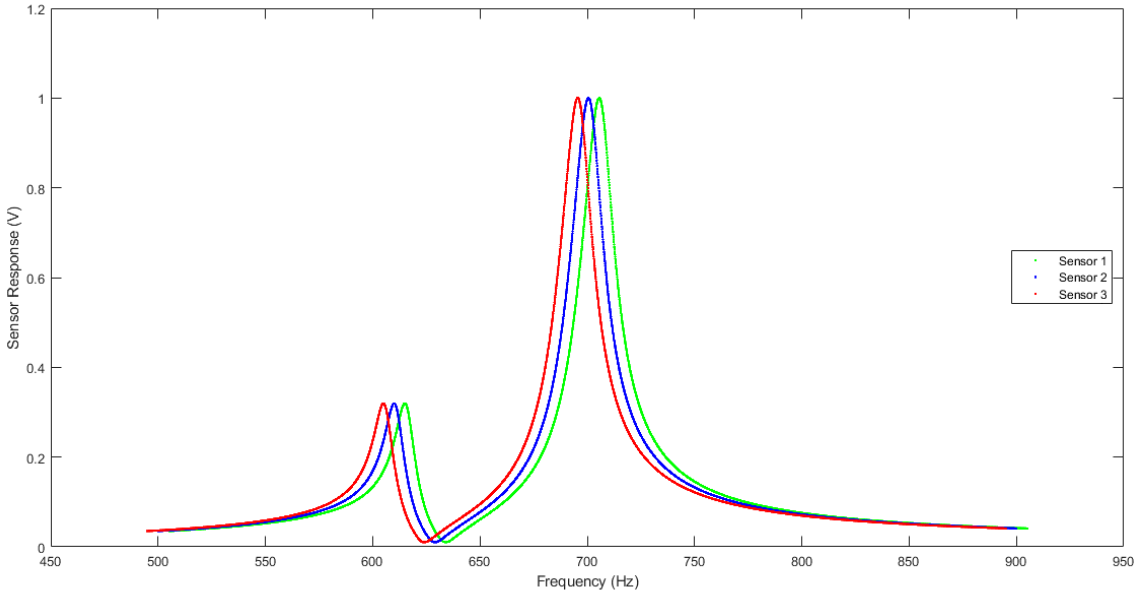

Figure 17. Representative Mismatched Frequency Response of Three Sensors

Central frequency was defined as the frequency which produces the maximum response for the sensor, shown in Figure 17 near 700 Hz. The second test variable was the signal-to-noise ratio (SNR) level, where white noise was introduced to the sensor output signal mathematically to reduce the SNR. The third test variable was the fluctuation on the directional pattern of the sensors, which may occur due to several factors, including but not limited by, manufacturing error, environmental fluctuations (e.g., wind, humidity, temperature, etc.), mountings and assembles, and close by obstacles interferences. This noise was also introduced mathematically. Finally, recorded acoustic signals of different commercially available quadcopter drones were used to characterize the effect on DOA estimation of different acoustic sources. Test parameters were varied one at a time, with the other parameters specified and held constant.

Five figures of merit (FOM) were employed for determining the effect of the four parameters on the error of the estimated DOA. All of them were computed over 360° in azimuth at one-degree intervals, for a total of 360 occurrences. The first two FOM are intended to show where the algorithm experiences inadequacies in the algorithm method. They are:

FOM 1: Number of DOAs with an error greater than ten degrees, which represent the DOAs outside a chosen acceptable range of error.

FOM 2: Number of ambiguous DOAs calculated. Ambiguous DOAs occur when the correlation between possible DOAs produces equal numbers of indications for two possible DOAs.

The next three FOM are computed only for the estimated DOAs with error less than ten degrees, to distinguish them from errors occuring due to inadequacies of the algorithm method. This is to show how accurate the algorithm is when it is operating as intended. The focus of these three FOM is to examine the DOA estimator performance as if the algorithm method and ambiguities have been uniformly resolved to satisfaction. This is expected to happen when the directional characteristics of the MEMS sensors are tailored by design of the assembly to obtain the required amount of asymmetry in the dipole pattern (discussed in Section II-A-2). The FOM are a measure of the directional error, obtained by the difference between the computed and actual DOAs for each angle. They are:

FOM 3: Average of the DOA error, to probe any potential systematic tilt caused by the algorithm or potential error in referencing the sensor array direction.

FOM 4 and FOM 5: Standard deviation of the DOA error, to probe the spread of the error, and three times the standard deviation, which for both positive and negative error values combined, theoretically represents 99.7% of all estimated DOAs, assuming a normal distribution of the error.

Finally, it is important to mention that testing of the algorithm with a one second audio sample showed that computational time to estimate one DOA lasted an average 0.03 seconds, running Matlab on a standard office PC.

1. Effects of Sensor Frequency Response Mismatch

Due to manufacturing tolerances, *Ormia*-inspired sensors may deviate slightly in their frequency response from each other. Because the algorithm described is based on comparison between sensors, innate discrepancies between the sensors will produce inherent errors in the accuracy of the algorithm. The effect of this frequency mismatch was analyzed by offsetting the frequencies of the sensors. To perform this analysis the frequency response of two of the sensors were offset by a set number of Hertz (Hz) symmetrically above and below a sensor whose central frequency was held fixed. The performance of the algorithm in DOA determination was then tested with drone audio as the frequency mismatch was varied. No other perturbation (noise source) was introduced. All tests were conducted using a sampled acoustic signal from a hovering unloaded Yuneec Typhoon small hexacopter, shown in Figure 18.

Figure 18. Yuneec Typhoon

Since the error in DOA estimation should increase with increasing mismatch in the sensors' frequency responses, the correlation band (step 5 of the algorithm – Section II-A-2) must be adjusted accordingly. It was found that the optimum correlation band is related to the central frequency mismatch by a second order polynomial as shown in Figure 19.

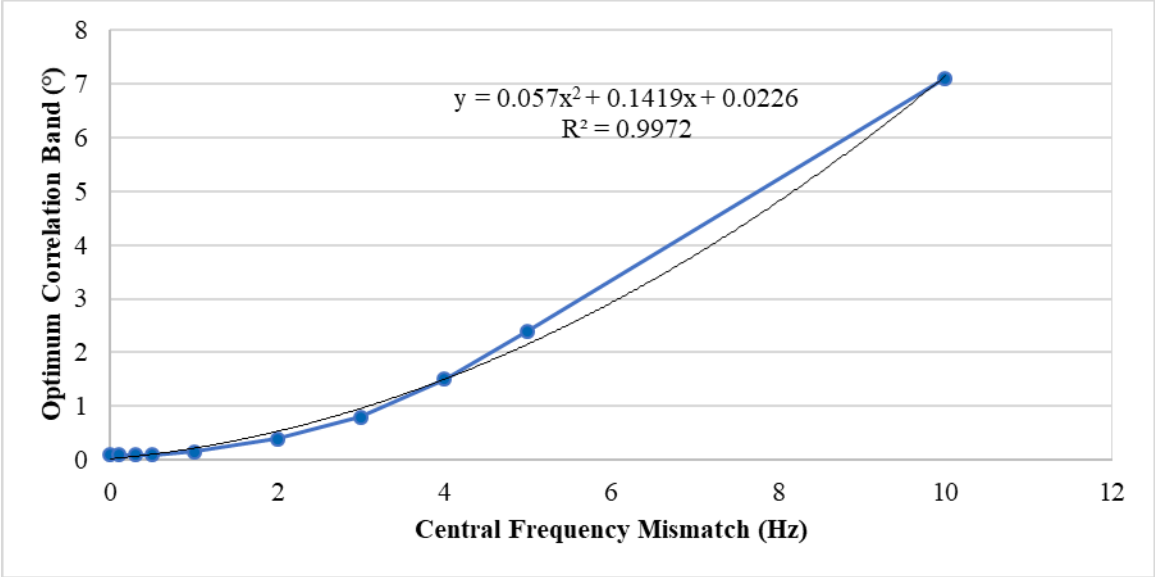

Figure 19. Optimum Correlation Band for Central Frequency Mismatch

Using these optimum correlation bands, the five FOM were evaluated as the central frequency mismatch was varied. Results are shown in Figure 20.

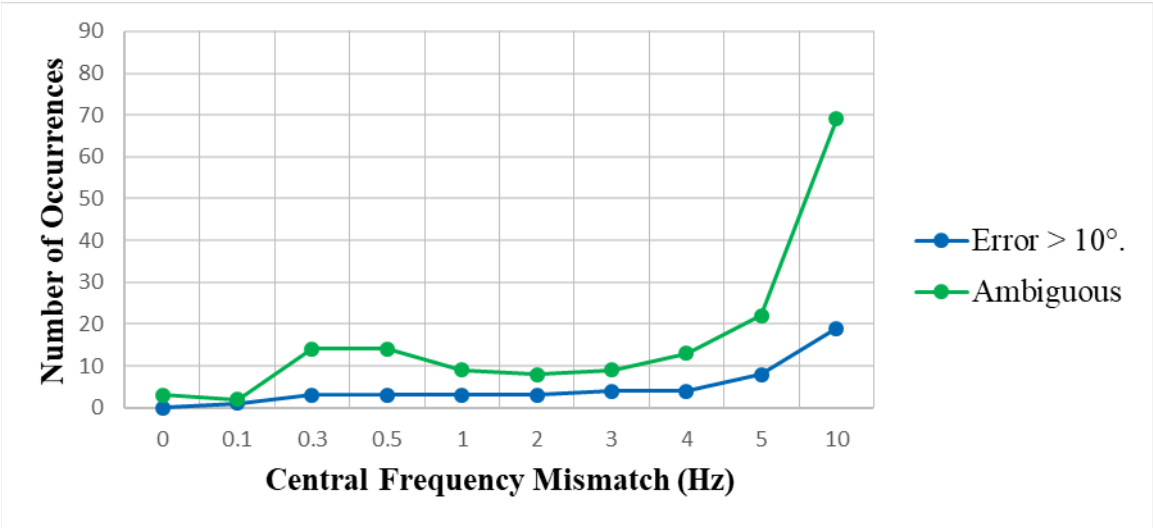

(a)

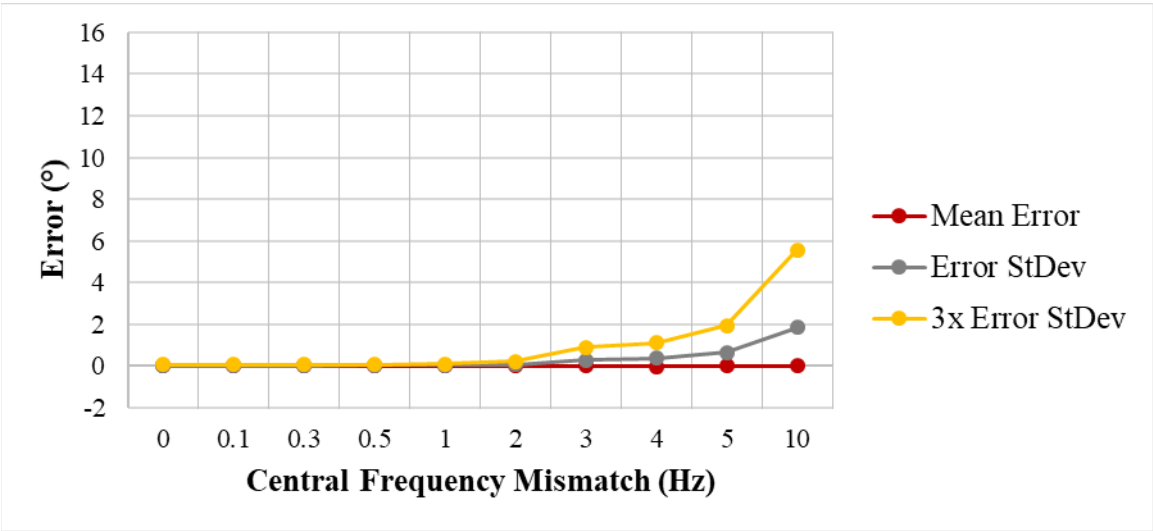

(b)

Figure 20. (a) Central Frequency Mismatch Effect on DOA Determination with Optimized Correlation Band (b) Central Frequency Mismatch Effect on Error with Optimized Correlation Band

As can be seen in Figure 20, all FOM increase as the frequency response mismatch increases. The standard deviation of the error was less than 1/30 of a degree when the central frequency mismatch was 1 Hz and less. A signal processing correction for

frequency response mismatch has been studied by our research group that would place all FOM near the best-case scenario with no mismatch.

2. Effects of Signal-to-Noise Ratio

The algorithm was tested over a range of SNR to characterize the effect of noise on the accuracy of the estimated DOA. The noise was artificially generated by a Gaussian random number generator and was added to the sensor input computationally, after the acoustic signal had been processed by the sensor program and integrated.

Background noise is generated once and applied across all three sensors at the same time sensors as a proportion of their signal strength, since background noise is common to all the sensors. System noise is generated and applied individually to each sensor so as to be random and different for each sensor. Noise was generated individually for each DOA determined. To attempt to emulate real world conditions, the maximum system noise was constrained to one-tenth of the background noise, since system noise realistically will be much less than environmental noise.

SNR effect on DOA estimation was conducted with no central frequency mismatch, to demonstrate the ideal case, shown in Figure 21. Testing was also conducted with a two Hz mismatch, with the three sensors placed at central frequencies of 701 Hz, 703 Hz, and 705 Hz, shown in Figure 22. No directional noise was injected and all testing was conducted using the same acoustic signal sample from an unloaded Yuneec Typhoon. DOAs were determined with a five degrees correlation band.

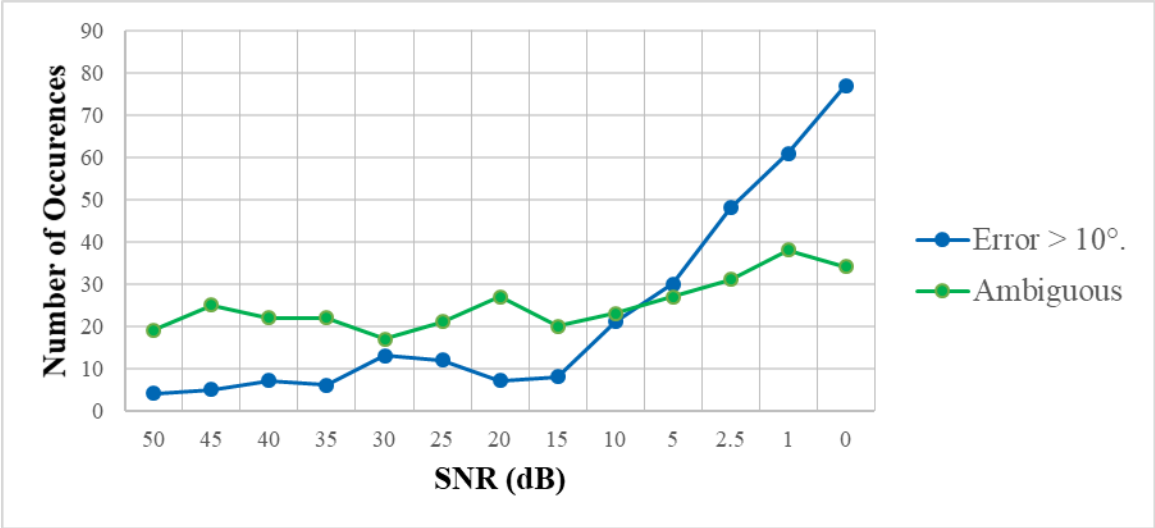

(a)

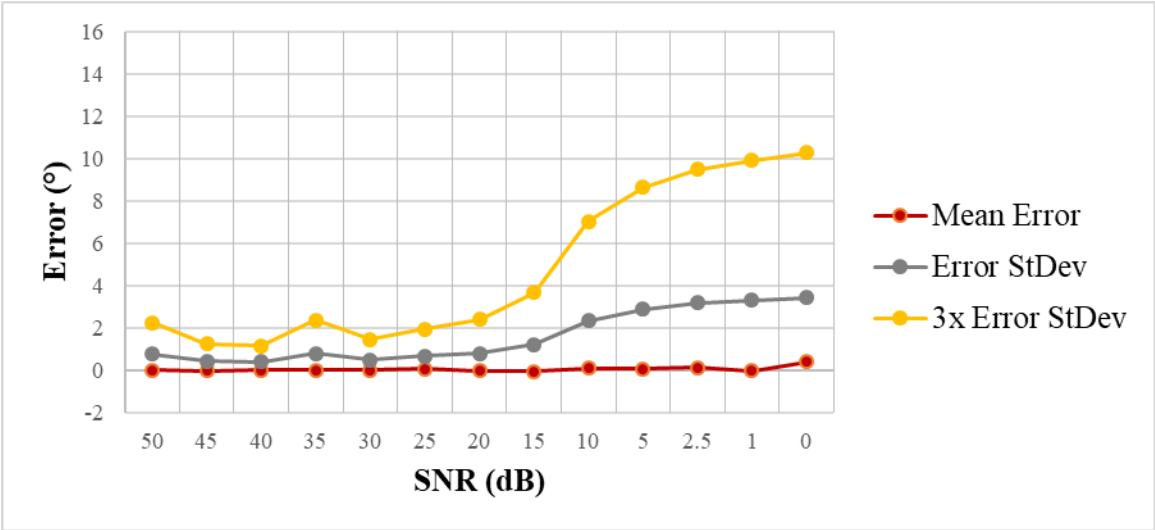

(b)

Figure 21. (a) SNR Effect on DOA Determination – 0 Hz Central Frequency Mismatch (b) SNR Effect on Error – 0 Hz Central Frequency Mismatch

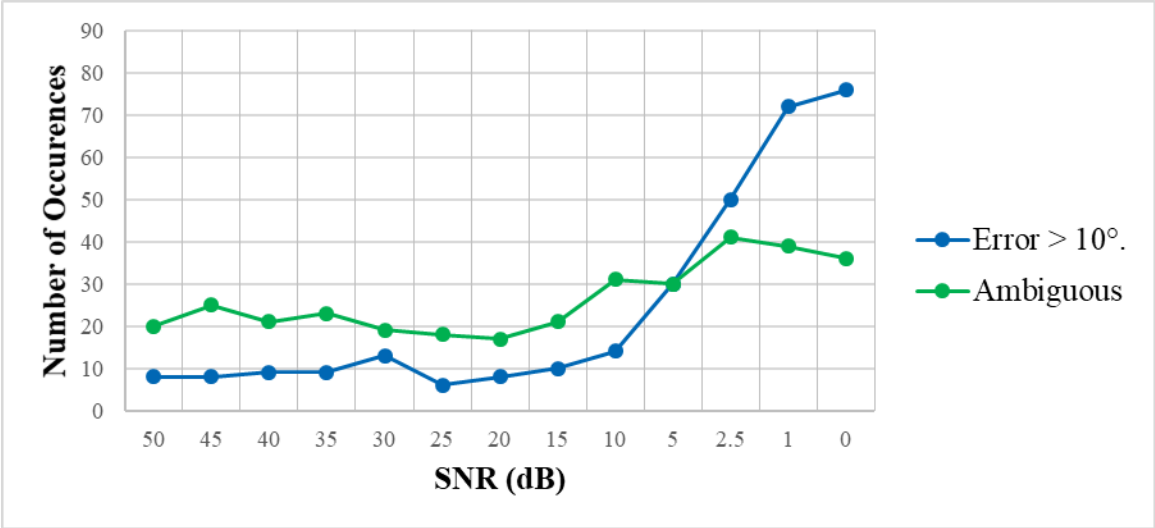

(a)

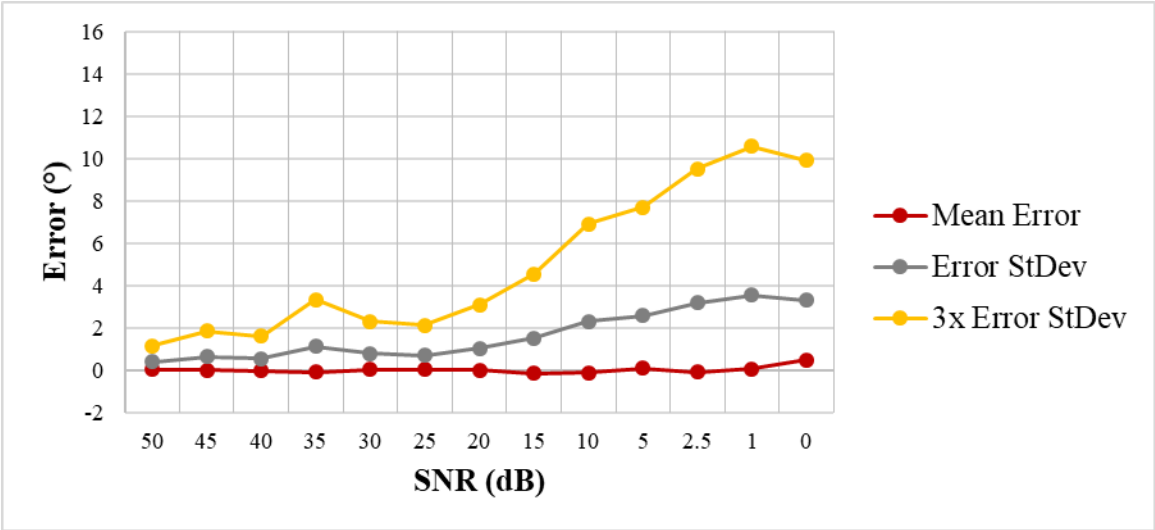

(b)

Figure 22. (a) SNR Effect on DOA Determination – 2 Hz Central Frequency Mismatch (b) SNR Effect on Error – 2 Hz Central Frequency Mismatch

For both the ideal case and the 2 Hz mismatch, the number of ambiguous DOAs and errors greater than ten degrees were approximately constant when the SNR was 15 dB and above. At approximately an SNR of 10 dB, the number of DOAs not found and ambiguous DOAs started increasing. At an SNR of 1 dB, the number of errors greater than

ten degrees was above twenty percent of the DOAs found and the DOA determination was largely unusable.

From Figures 21 and 22, it is observed that the counts of error larger than ten degrees as well as the number of ambiguous findings are significantly large even high SNR values. This indicates a vulnerability of this algorithm to noise, for this particular directional response pattern (see discussion in Section II-A-2). In contrast, Figures 21 and 22 show that the higher the SNR is, the lower the standard deviation of the error is, as expected. In addition, the standard deviation is low even at low SNRs. The average error over 360° of azimuth remains close to zero, indicating no artificial tilt.

3. Effects of Directional Response Fluctuations

The sensor directional response shown in Figures 4(a) (dipole pattern) and 4(b) (asymmetric dipole pattern) will not always follow the design specifications and are prone to perturbations. To observe the effect of the variability of the directional pattern, directional noise was added using a random number generator with a Gaussian distribution with a maximum corresponding to a fraction of a degree. This random noise was generated and added angle by angle over a full 360° in azimuth for each sensor independently.

Testing of directional noise was conducted with an SNR of 25 dB and sensor central frequency mismatches of both the ideal case at 0 Hz mismatch and at 2 Hz mismatch. DOAs were estimated with five degrees correlation bands. Results are shown in Figures 23 and 24.

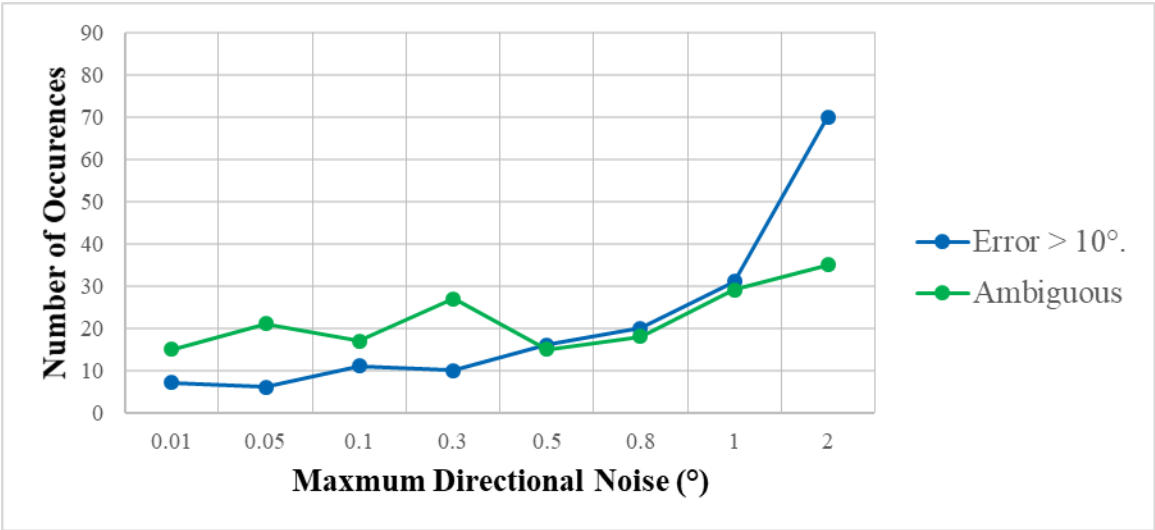

(a)

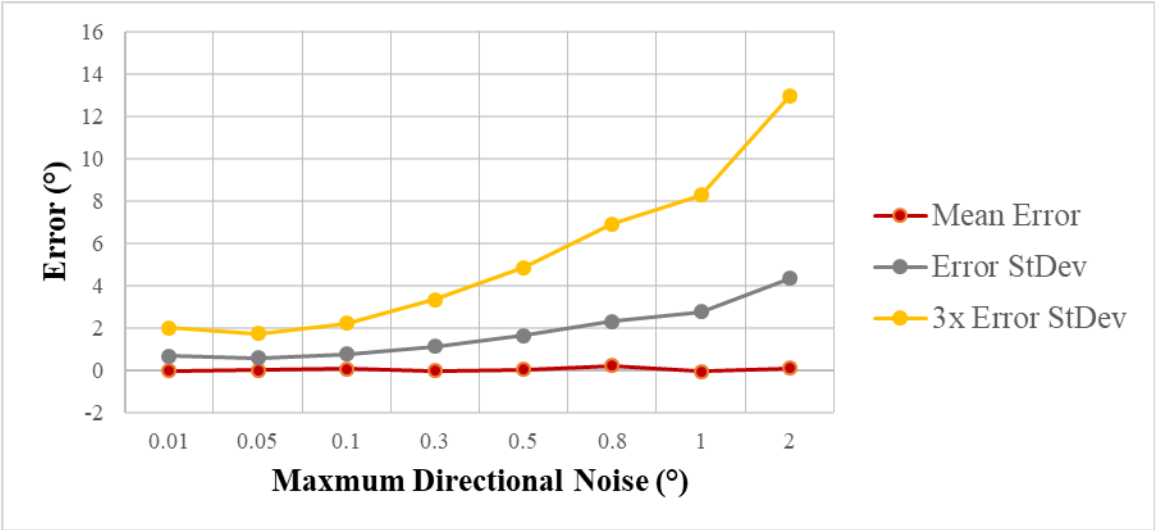

(b)

Figure 23. (a) Directional Noise Effect on DOA Determination – 0 Hz Central Frequency Mismatch (b) Directional Noise Effect on Error – 0 Hz Central Frequency Mismatch

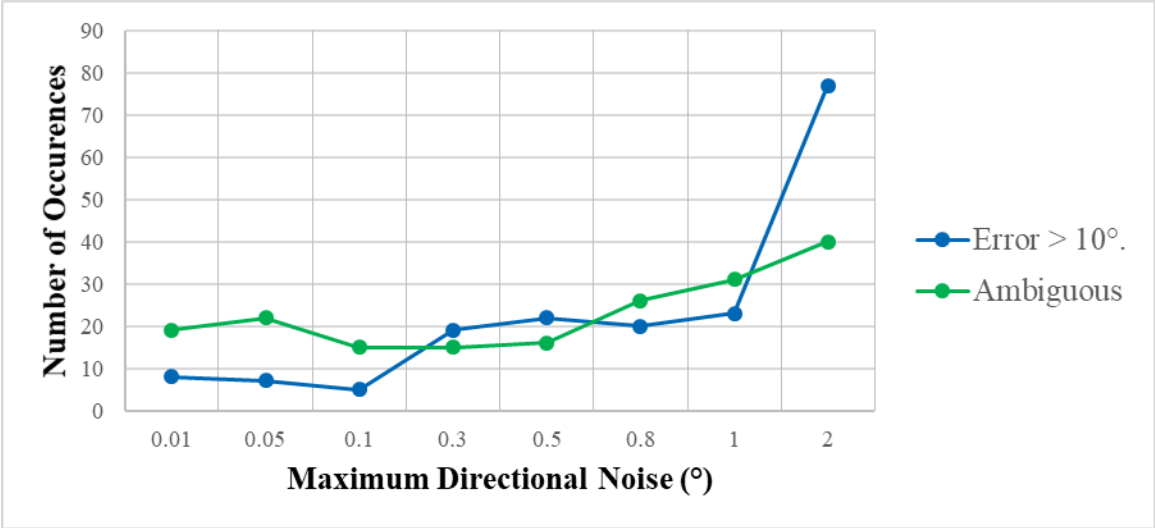

(a)

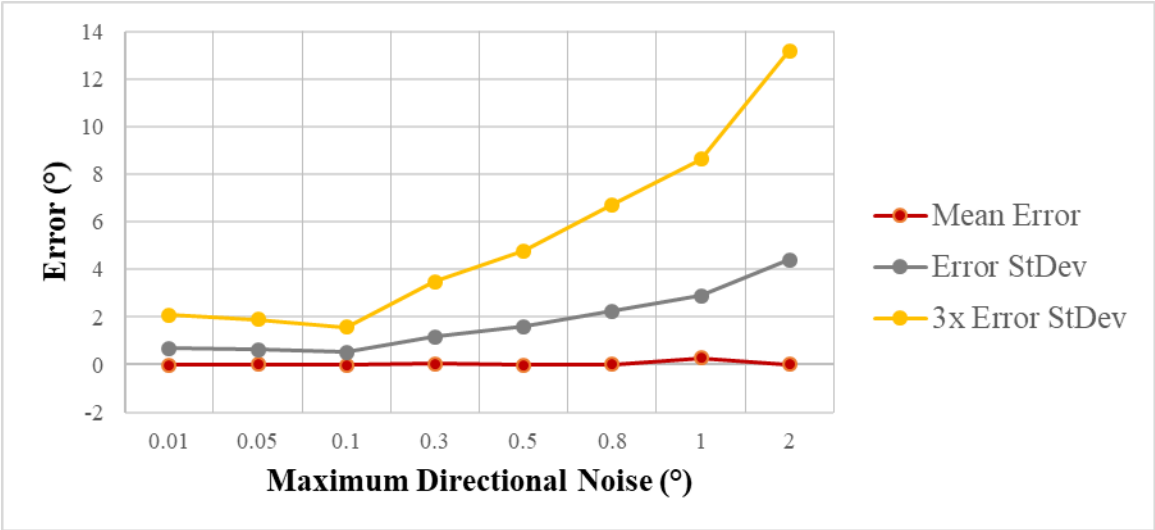

(b)

Figure 24. (a) Directional Noise Effect on DOA Determination – 2 Hz Central Frequency Mismatch (b) Directional Noise Effect on Error – 2 Hz Central Frequency Mismatch

From Figures 23 and 24, it is evident that directional noise has a steadily increasing effect on accuracy and reliability of the DOA determination. Interestingly, the number of errors greater than ten degrees is not much affected by this error and most largely affected by the SNR, which was set to 25 dB in this case.

4. Effects of Drone Type

The DOA estimation algorithm was tested using four commercially available drones to investigate the response of the algorithm against a variety of different acoustic signals. The drones tested were the Yuneec Typhoon, DJI Phantom 4 Pro, DJI Phantom 3 Pro, DJI Mavic Pro, and the DJI Matrice 600. The Phantom 4 Pro and Typhoon were tested both when unloaded and when carrying a 940 gram (g) weight. The Phantom 3 Pro was tested only when loaded with 940 g. The Yuneec Typhoon is a hexacopter and the other drones are quadcopters.

The audio for these drones was sampled for one second for use in the DOA estimation algorithm. The frequency spectra, between 500 and 900 Hz, are shown in Figure 25.

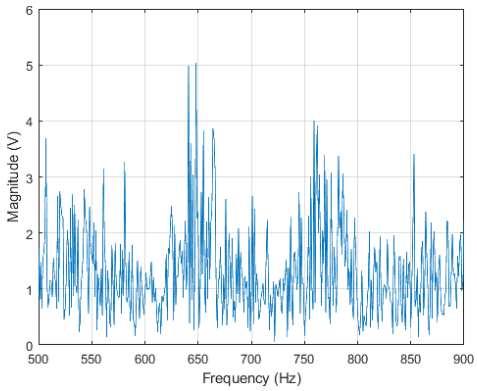
Magnitude (V)
Frequency (Hz)

(a)

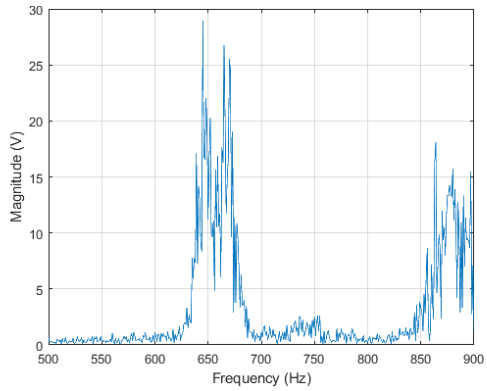
Magnitude (V)
Frequency (Hz)

(b)

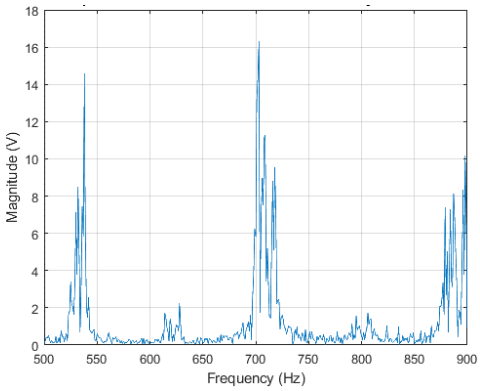
Magnitude (V)
Frequency (Hz)

(c)

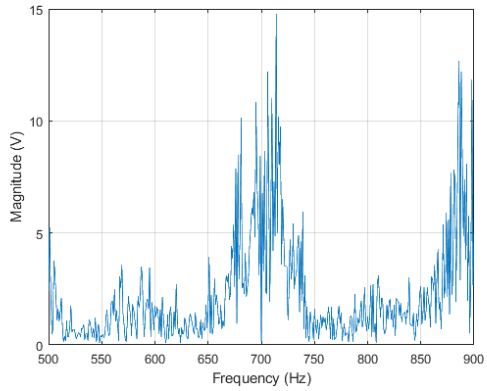
Magnitude (V)
Frequency (Hz)

(d)

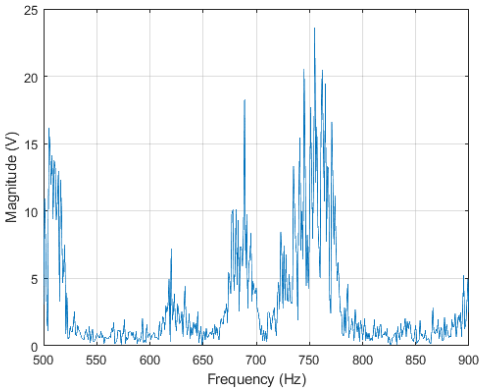
Magnitude (V)
Frequency (Hz)

(e)

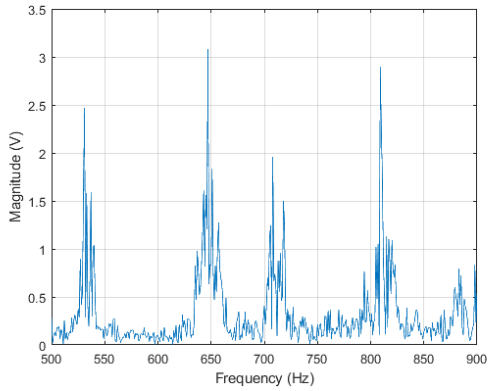
Magnitude (V)
Frequency (Hz)

(f)

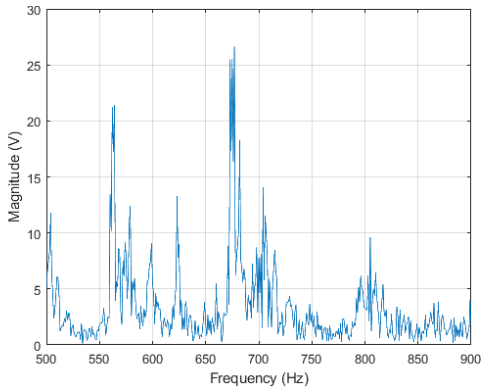

(g)

Figure 25. Frequency spectrum of one second of audio from: (a) Yuneec Typhoon – No Load (b) Yuneec Typhoon - Loaded with 940 g (c) Phantom 4 Pro – No Load (d) Phantom 4 Pro – Loaded with 940 g (e) Phantom 3 Pro – Loaded with 940 g (f) Mavic Pro (g) Matrice 600

The DOA for these drones were all analyzed with five degrees correlation bands, an SNR of 25 dB, and 0.3 maximum Gaussian directional noise. Results are shown in Figures 26 and 27.

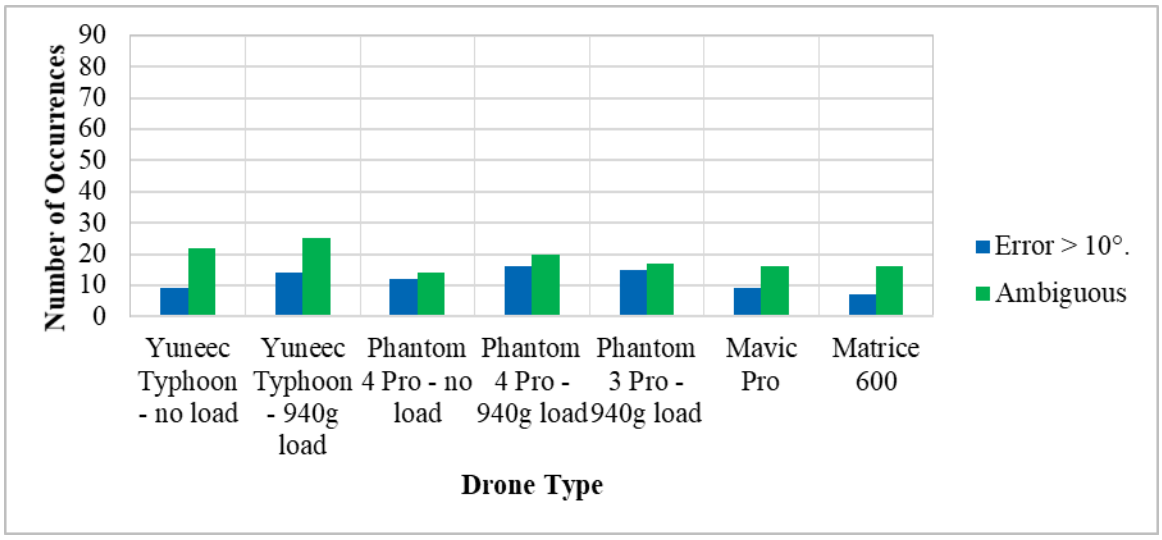

(a)

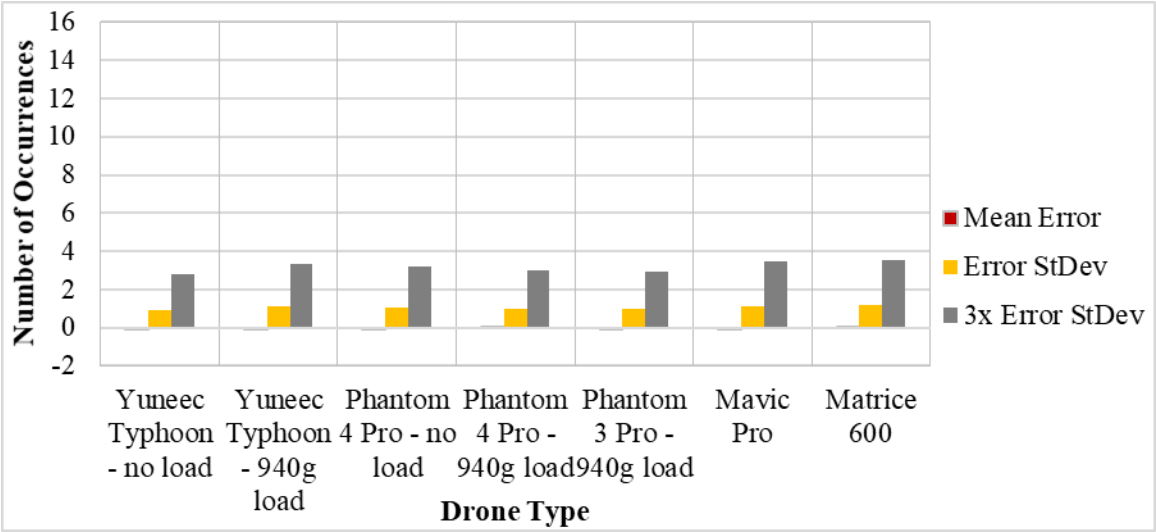

(b)

Figure 26. (a) Drone Type Effect on DOA Determination – 0 Hz Central Frequency Mismatch (b) Drone Type Effect on Error – 0 Hz Central Frequency Mismatch

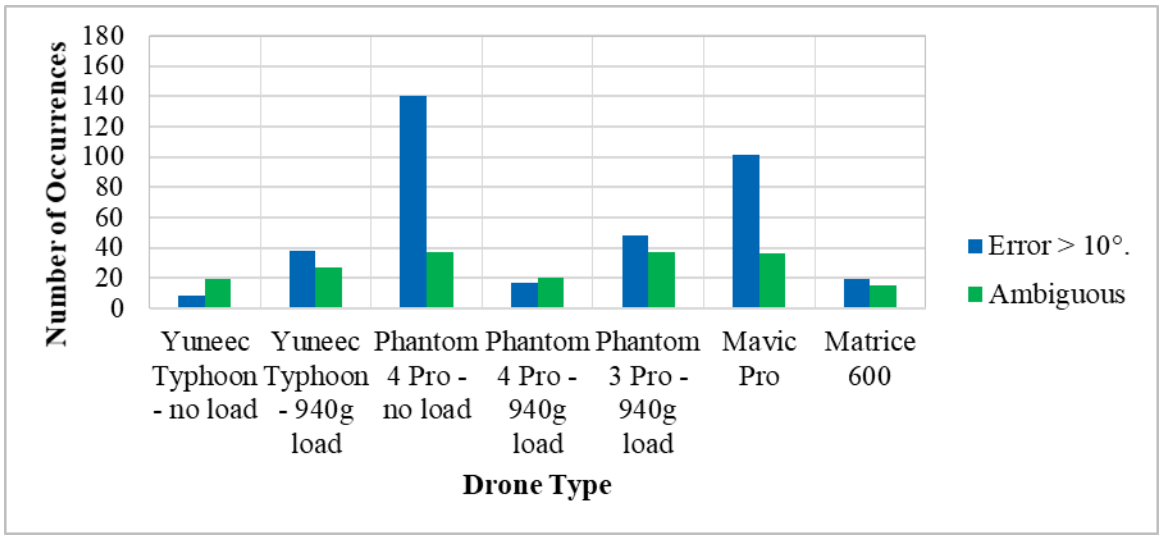

(a)

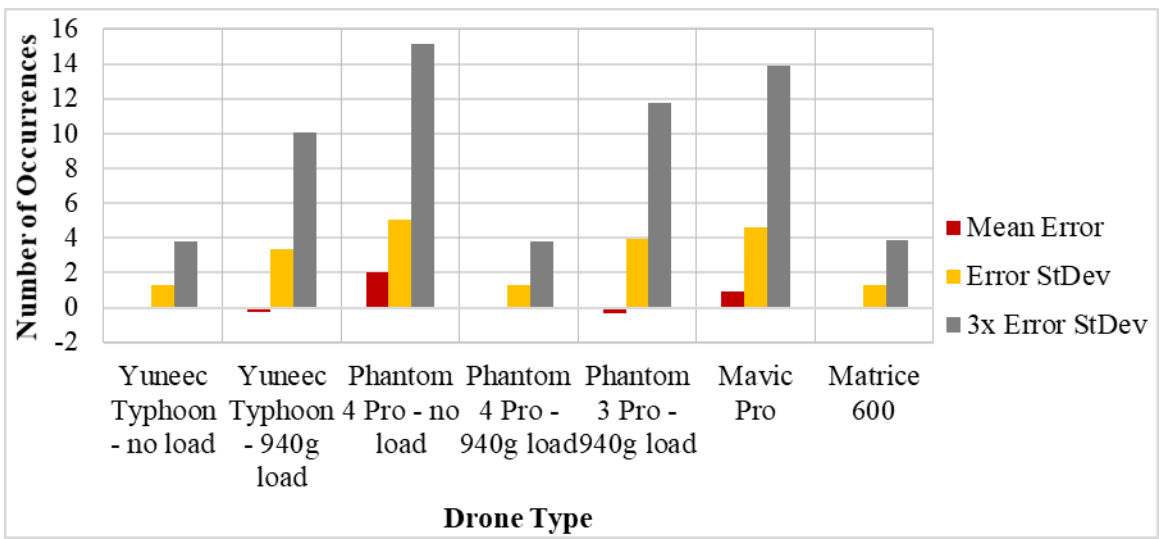

(b)

(Note the change in scale of the vertical axis in (a) from previous graphs showing ambiguous and errors greater than ten degrees, for visual purposes)

Figure 27. (a) Drone Type Effect on DOA Determination – 2 Hz Central Frequency Mismatch (b) Drone Type Effect on Error – 2 Hz Central Frequency Mismatch

The most marked response was the increase in the number of ambiguous DOAs and error greater than ten degrees between the zero mismatch case, shown in Figure 26(b), and the case of a 2 Hz central frequency mismatch, shown in Figure 27(b). The greatest change,

however, for a 2 Hz mismatch, was in the number of errors greater than ten degrees, which for the Matrice 600 leaps to 101 and for the Phantom 4 Pro with no load surged to 140. In contrast, the Yuneec Typhoon, both loaded and unloaded, as well as the Phantom 3 with a load, and even the Phantom 4 when loaded, all showed much lower values. Based on these results, it can be concluded that the accuracy of the algorithm used is highly dependent on the mismatch of the sensors frequency response. Sources more uniformly distributed over the spectrum are less prone to large errors.

5. Cause of Ambiguous DOAs and Errors Greater than Ten Degrees

Investigating the source of larger errors and ambiguous DOAs revealed the same general pattern over a full 360° rotation, irrespective of magnitudes of SNR and directional variation and which drone type was used. As can be seen in Figures 28–30, the erroneous DOAs fall in the same general locations.

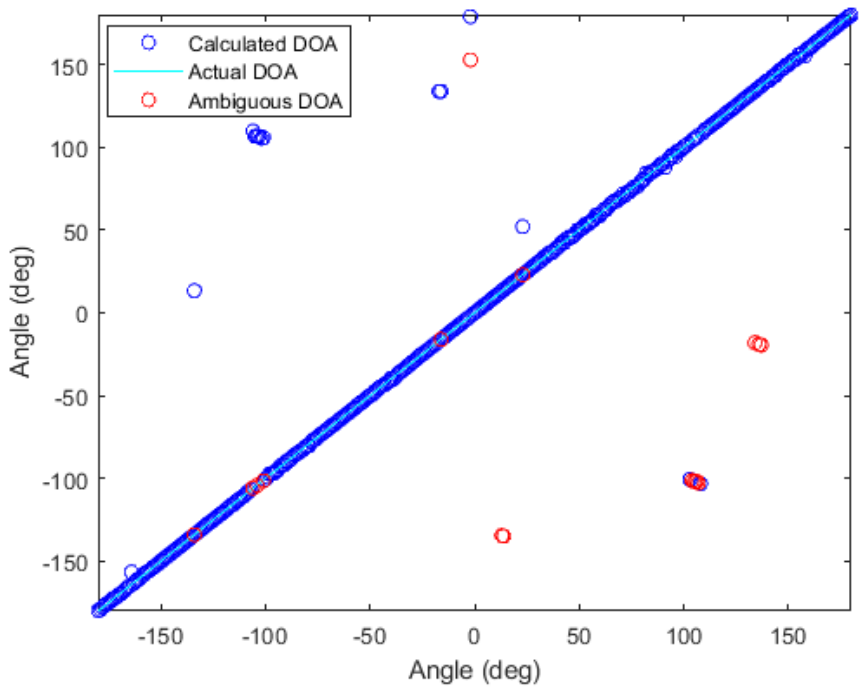

Figure 28. Unloaded Typhoon with 0.1 Hz Central Frequency Mismatch, 0.0° Directional Variation, and 25 dB SNR

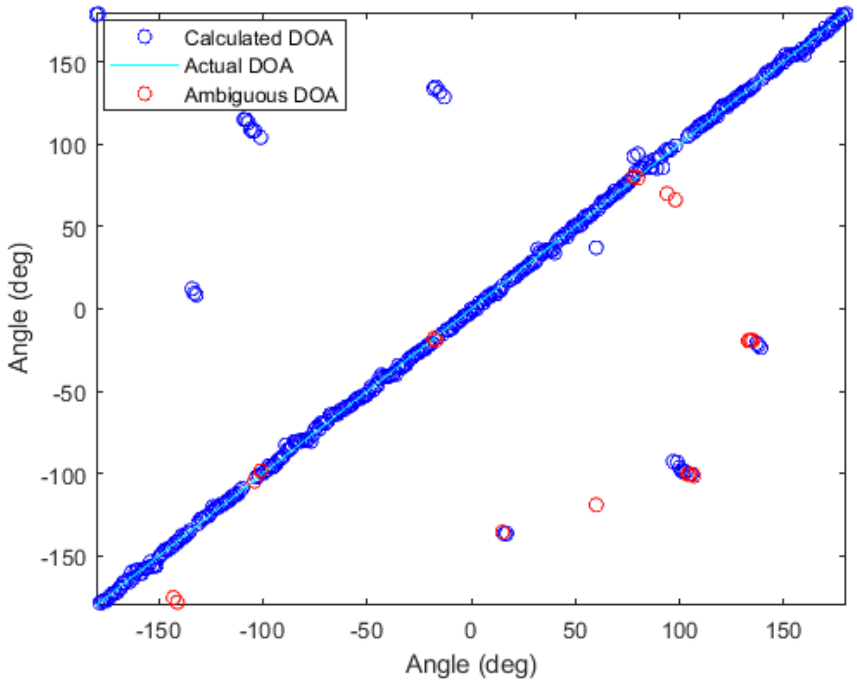

Figure 29. Mavic Pro with 0.5 Hz Central Frequency Mismatch, 0.3° Directional Variation, and 25 dB SNR

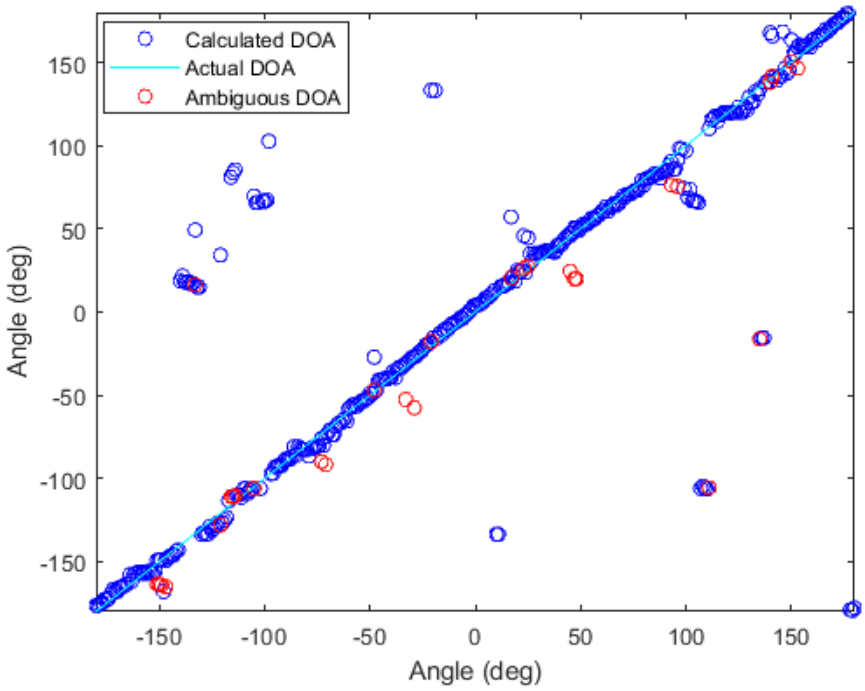

Figure 30. Typhoon Loaded with 940 g with 2 Hz Central Frequency Mismatch, 0.3° Directional Variation, and 25 dB SNR

More erroneous DOAs arise as more error sources are added to the analysis, but there is a noticeable pattern in Figures 28–30 where these DOAs are located. Investigating the individual DOAs where these problems occur reveals a reoccurring issue in the correlation of the possible DOAs found by the nearest neighbor function. Examining the divisions of the angular intervals selected by the unaltered sensor response reveals a potential cause. Overlaying the DOA estimations from Figure 30 with the angular intervals, the potential causes of ambiguity and outlier DOAs can be seen, as shown in Figure 31.

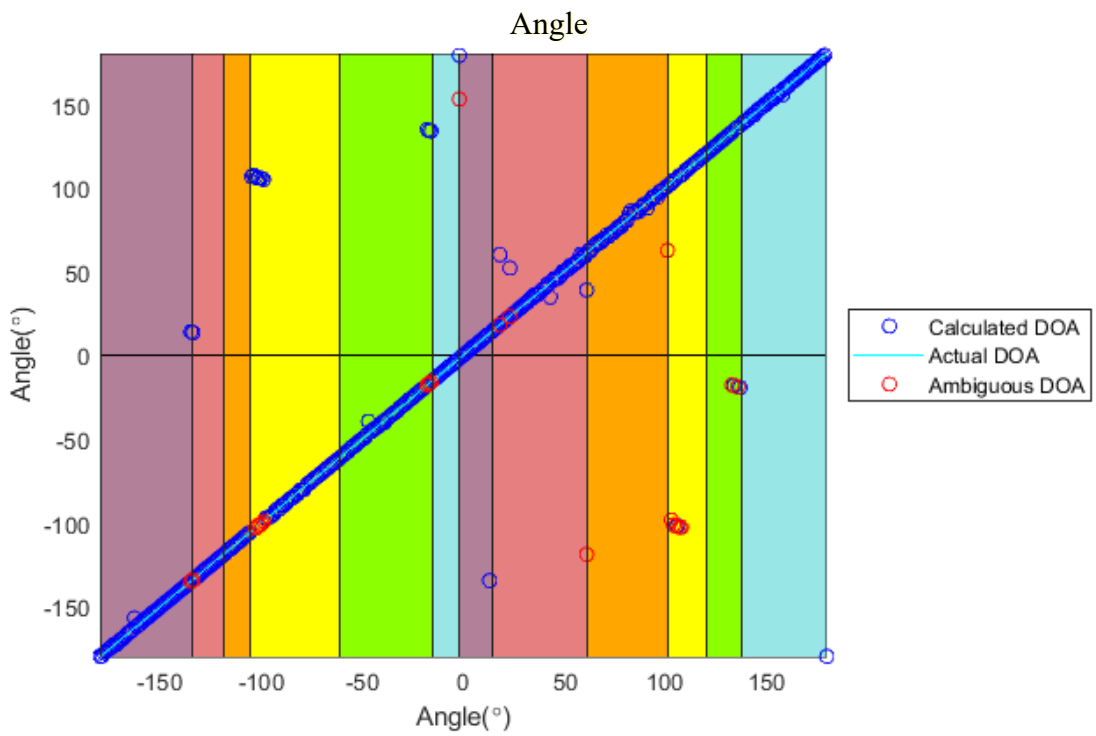

Like-colored regions are ambiguous to each other

Figure 31. Unloaded Typhoon with 0.1 Hz Central Frequency Mismatch, 0.0° Directional Variation, and 25 dB SNR with Calibration Curve Divisions

The asymmetric directional response of individual sensors provided by the sensor array was intended to impart sufficient uniqueness of the calibration curves to prevent miscalculations like the one presented, but with error the algorithm sometimes does not estimate DOAs accurately. The reduced back lobe on the sensor responses introduced by the array assembly reduced the ambiguous regions, but did not entirely eliminate them. As

seen in Figure 31, the same colored regions on the left and right sides of the Figure 31 are ambiguous to one another, and the erroneous DOAs are often located in the smaller ambiguous regions. Introducing sufficient uniqueness in the calibration curve to remove these smaller ambiguous regions could be accomplished by sufficient attenuating the back lobes to a condition where the maxima of one back lobe is less than the crossing point of the other two sensors front lobes (see the indications in Figure 13).

As can be seen in Figure 31, other sources of error are the boundaries between regions themselves. To reduce this error, it would be necessary to successfully extend the selected calibration curves intervals to overlap one another and thereby prevent miscalculations at the borders between the intervals. This requires more sophisticated approaches and it is left for future work.

B. MEASURED SENSOR RESPONSES

Two sensor array configurations were built and characterized in an anechoic chamber. In this case the sensors showed nearly matched frequency responses (resonant peak difference less than one degree). The developed algorithm was tested for both arrays with conditions described in the following sections.

1. Asymmetric Dipole Pattern Response

A prism-like mount was 3D printed with air gaps to provide the asymmetric dipole pattern response shown in Figure 32. Here the back lobes are suppressed to approximately 60% of the front lobes.

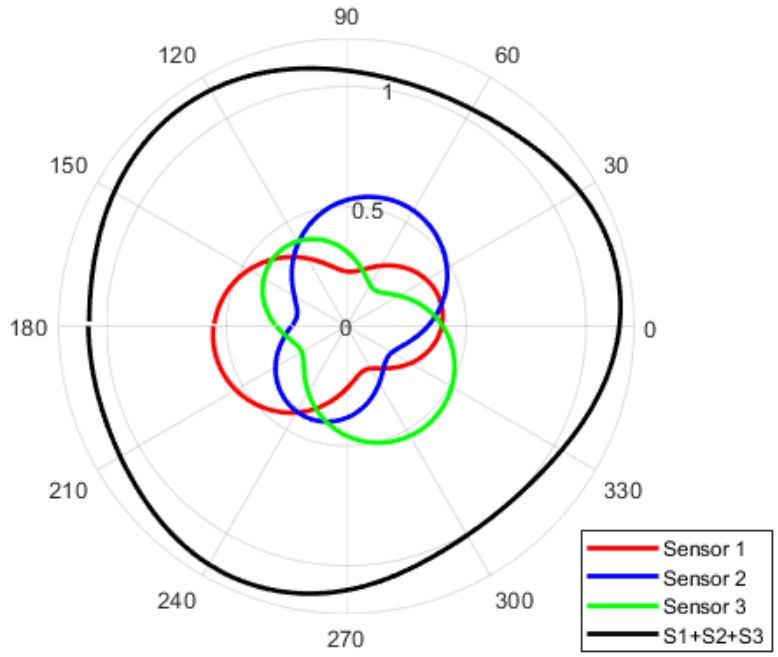

Radial scale in volts

Figure 32. Polar Plot of Measured Dipole Directional Response

This asymmetric dipole pattern response created the angular intervals shown in Figure 33. These angular intervals were created by the ranking of the relative magnitudes of the sensor responses. Like-colored regions are ambiguous to each other.

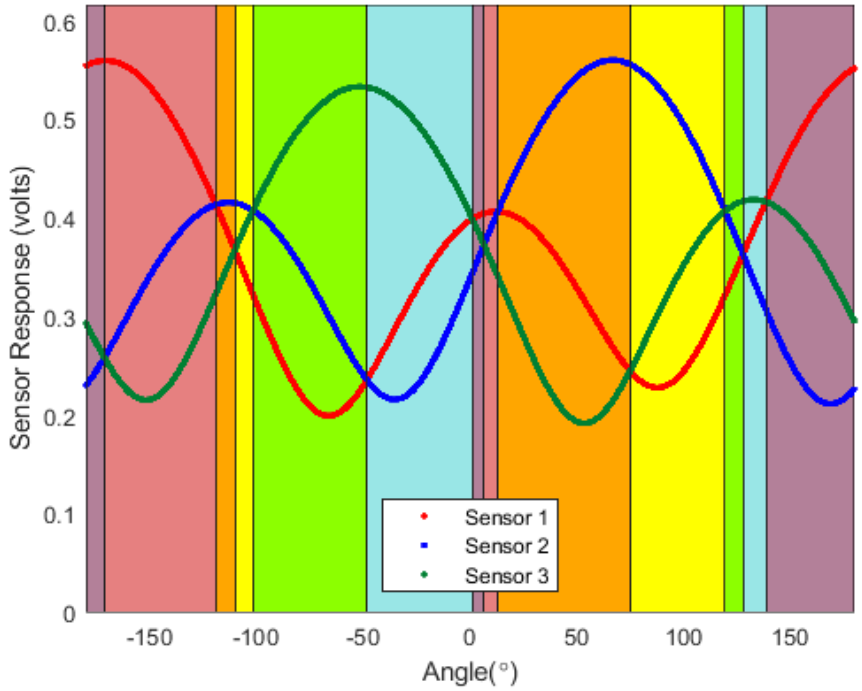

Figure 33. Measured Directional Response of Asymmetric Dipole Pattern Directional Response with Corresponding Angular Intervals

The DOA determination algorithm was run for the recorded sample of the Yuneec Typhoon over 360° in azimuth at one degree intervals. Initially, no artificial noise was introduced. The results are shown in Figure 34.

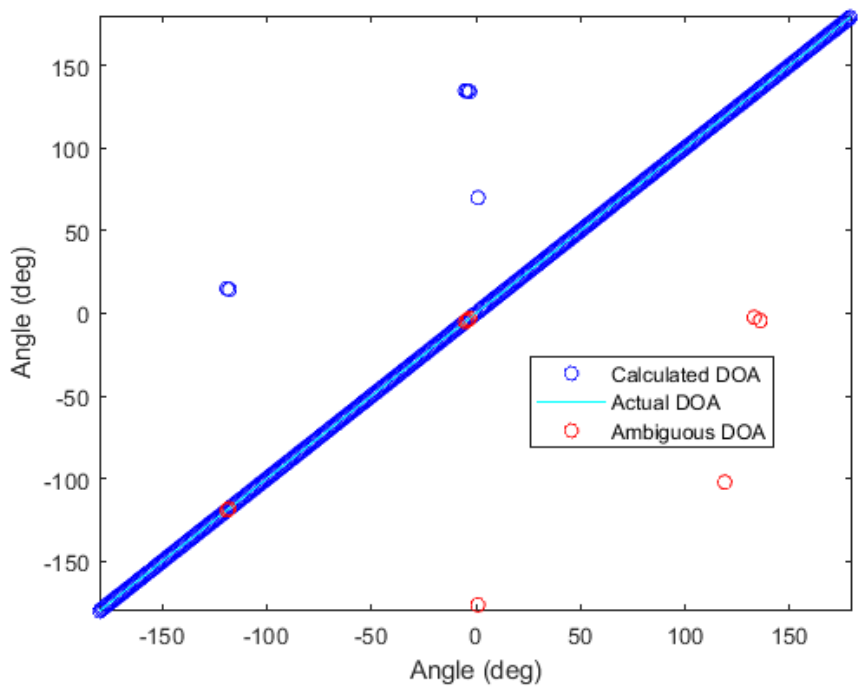

Figure 34. Asymmetric Dipole Pattern DOA Determination – No Introduced Noise

It can be observed that the same pattern of errors greater than ten degrees and ambiguous DOAs remains from the previous analysis, occurring on the ambiguous intervals and near the interval interfaces. Error for this analysis is shown in Figures 35.

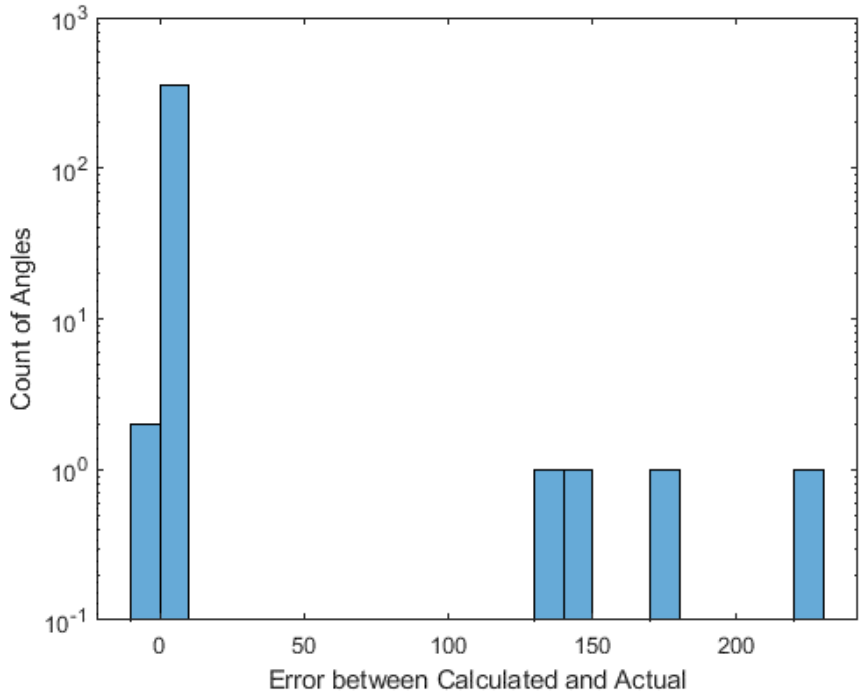

Note the logarithmic scale used for the vertical axis

Figure 35. Error Histogram for Asymmetric Dipole Pattern DOA Determination – No Introduced Noise

An analysis of the effect of SNR was performed on this measured asymmetric dipole directional response. The results are shown in Figure 36.

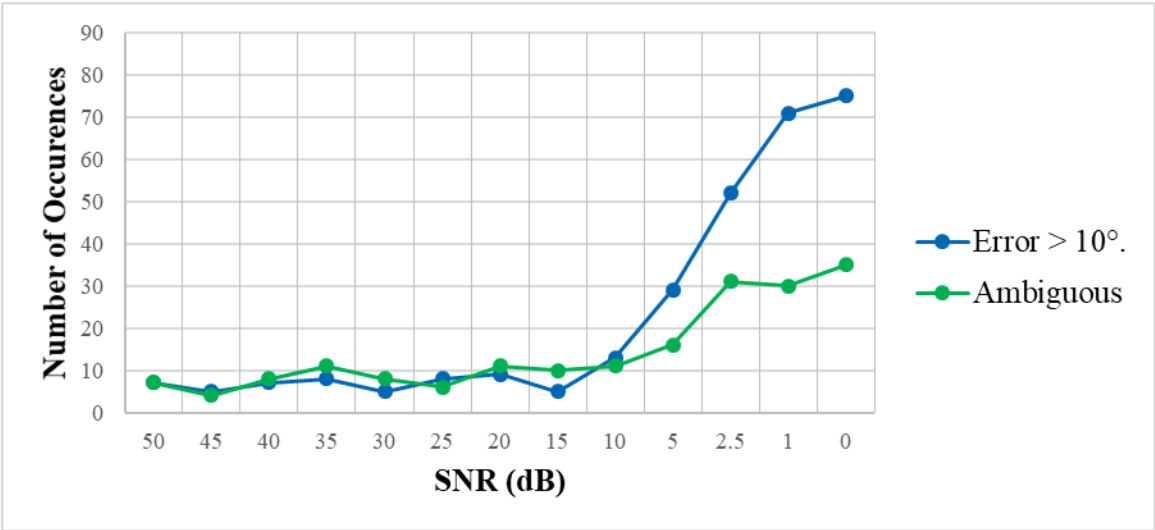

(a)

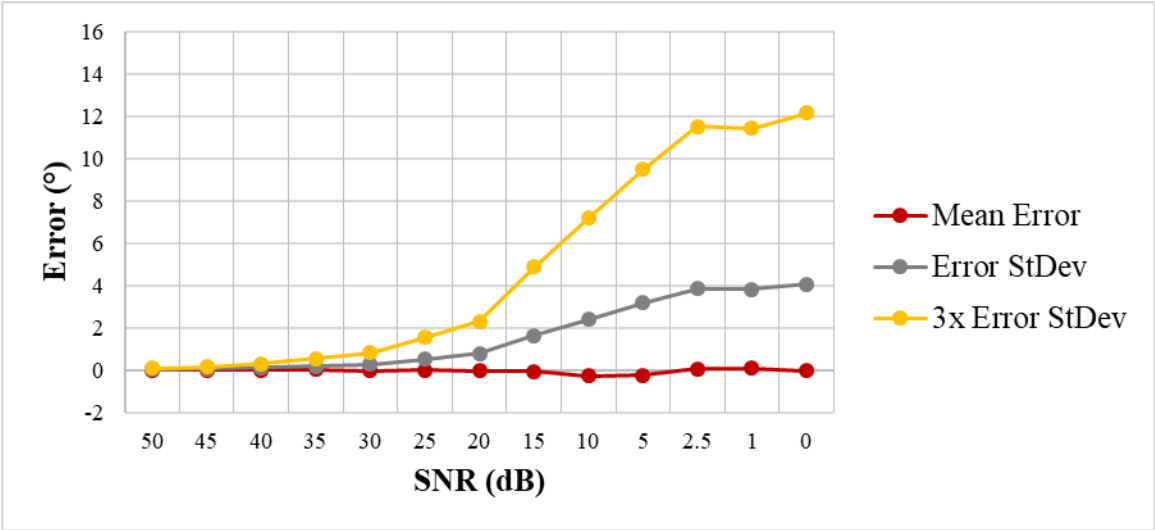

(b)

Figure 36. (a) SNR Effect on DOA Determination for Measured Asymmetric Dipole Response – 0 Hz Central Frequency Mismatch (b) SNR Effect on Error for Measured Asymmetric Dipole Response – 0 Hz Central Frequency Mismatch

The increase in larger error and ambiguous DOAs follows nearly the same pattern as for the modeled asymmetric dipole response used in previous analysis for a 0 Hz mismatch, shown in Figure 20. However, the number of ambiguous DOAs reduced significantly. This indicates that the reduction of the back lobe indeed reduces the

ambiguity regions and increases the DOA determination accuracy. Figure 37 shows that for SNR lower than 10 dB the DOA determination is significantly compromised. The DOA determination for an SNR of 5 dB is shown in Figure 37 as representative of the error in DOA estimation for low SNR.

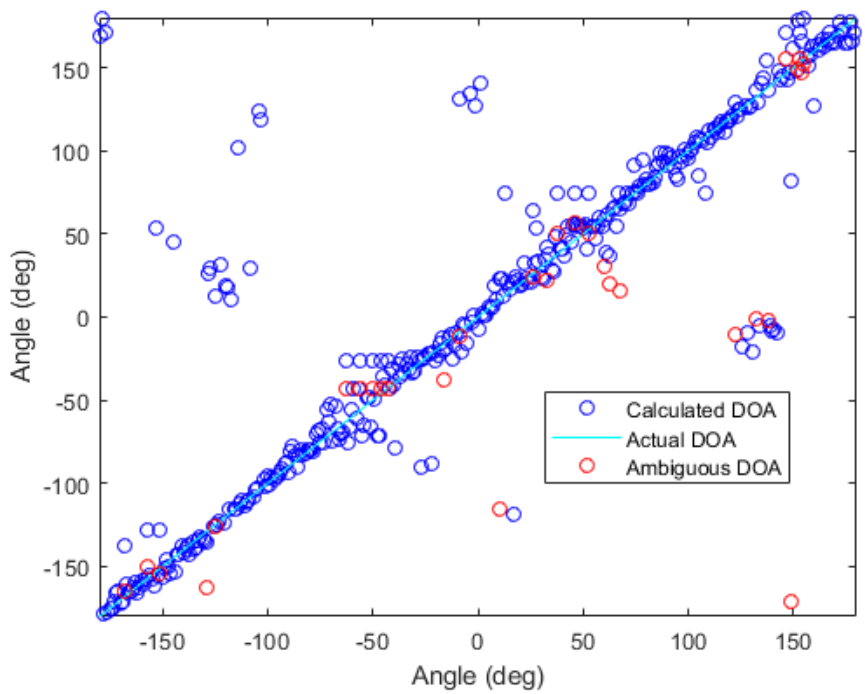

Figure 37. DOA Determination for an Asymmetric Dipole Directional Respones - 0 Hz Central Frequency Mismatch, 5 dB SNR

2. Cardioid Pattern Response

To test the hypothesis that reducing the back lobe of the directional pattern of the MEMS sensors would reduce the DOA determination ambiguity, the gaps on the prism-like sensor mount were closed to generate the directional pattern shown in Figure 38.

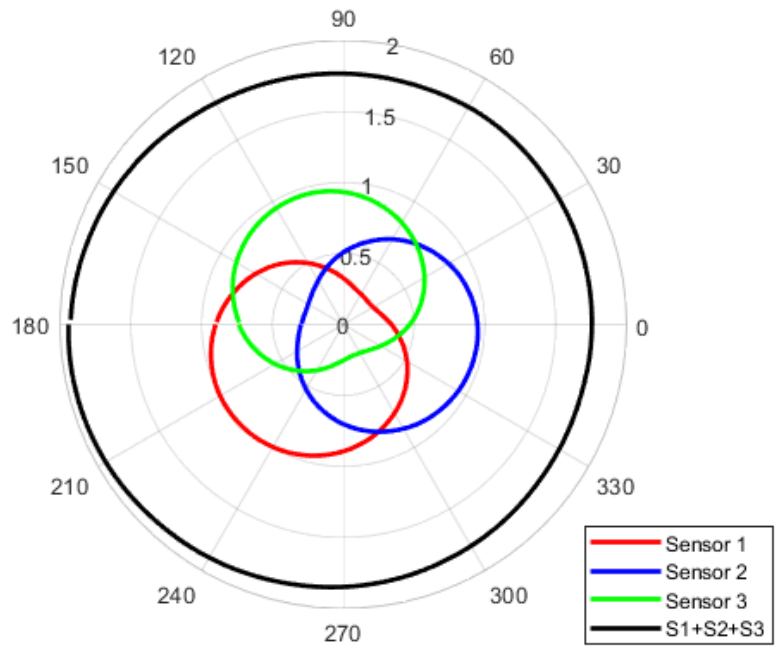

Radial axis in volts

Figure 38. Polar Plot for Measured Cardioid Directional Response

The back lobes of the sensors directional responses were suppressed, generating cardioid-like directional patterns. This created an entirely unique calibration curve, where there were no ambiguous intervals as seen previously, shown in Figure 39. Each individual angular interval has its own unique combination of relative magnitudes between the three sensors, creating six angular intervals.

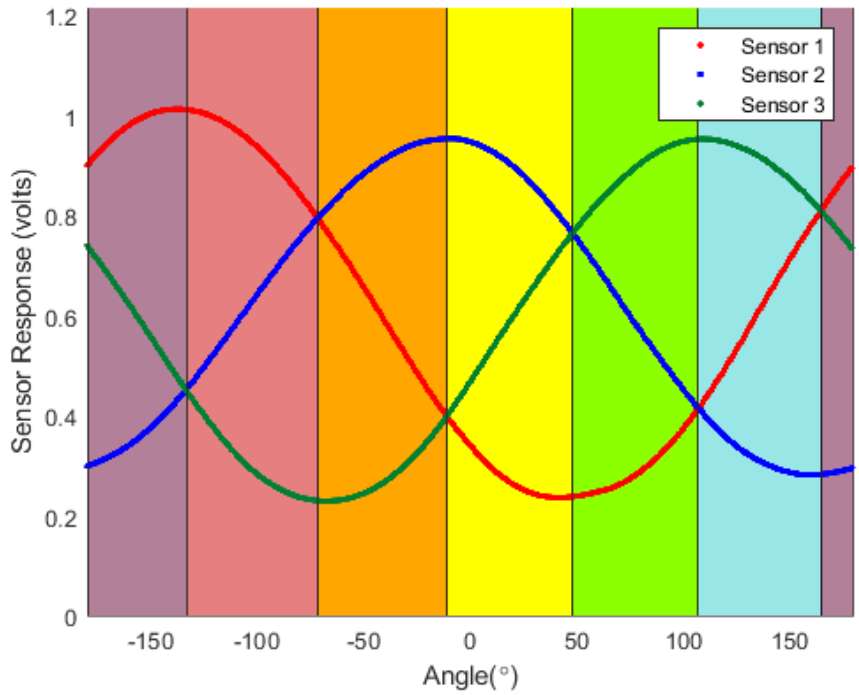

Figure 39. Measured Directional Response of Measured Cardioid Directional Response with Angular Intervals

The same procedure used in Section II-A-2 was repeated here. The results are shown in Figure 40.

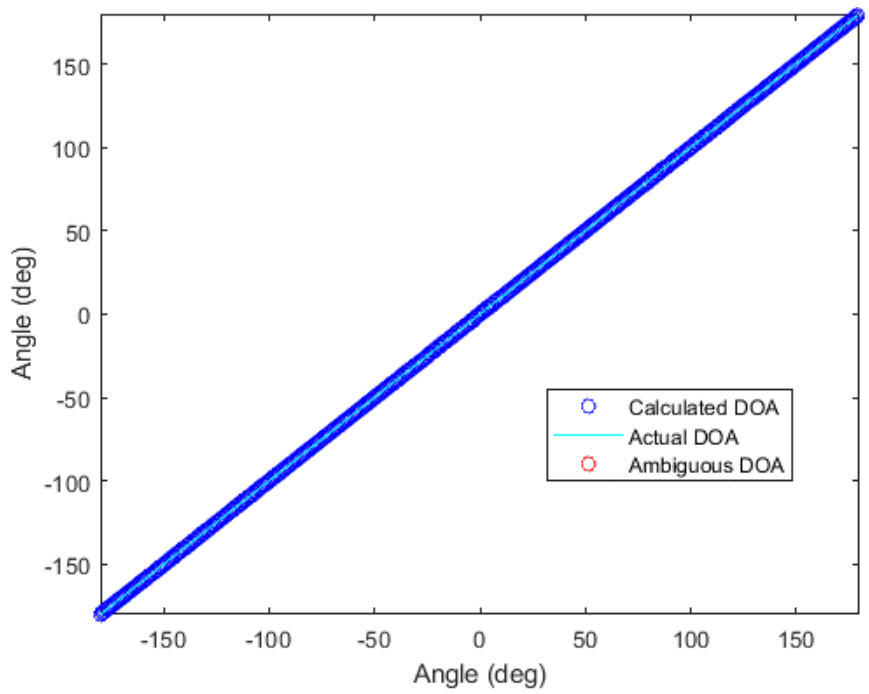

Figure 40. Cardioid Response DOA Determination – No Introduced Noise

Figure 40 shows that using the cardioid directional responses, all DOAs were found with negligible error and no ambiguous DOAs were found. The error histogram is shown in Figure 41.

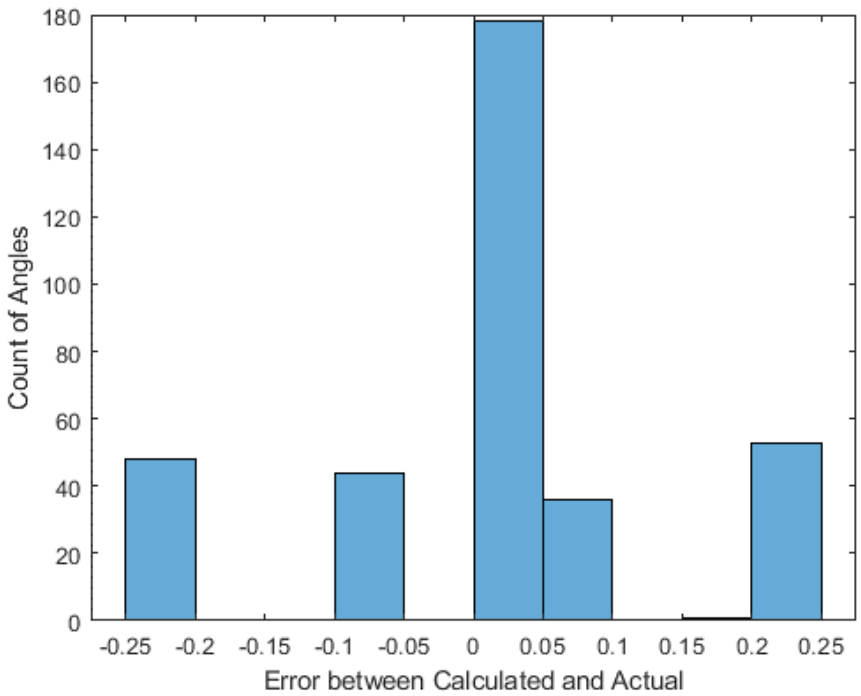

Figure 41. Error Histogram for Cardioid Response DOA Determination – No Introduced Noise

An analysis of the effect of SNR was performed and the results are shown in Figure 42.

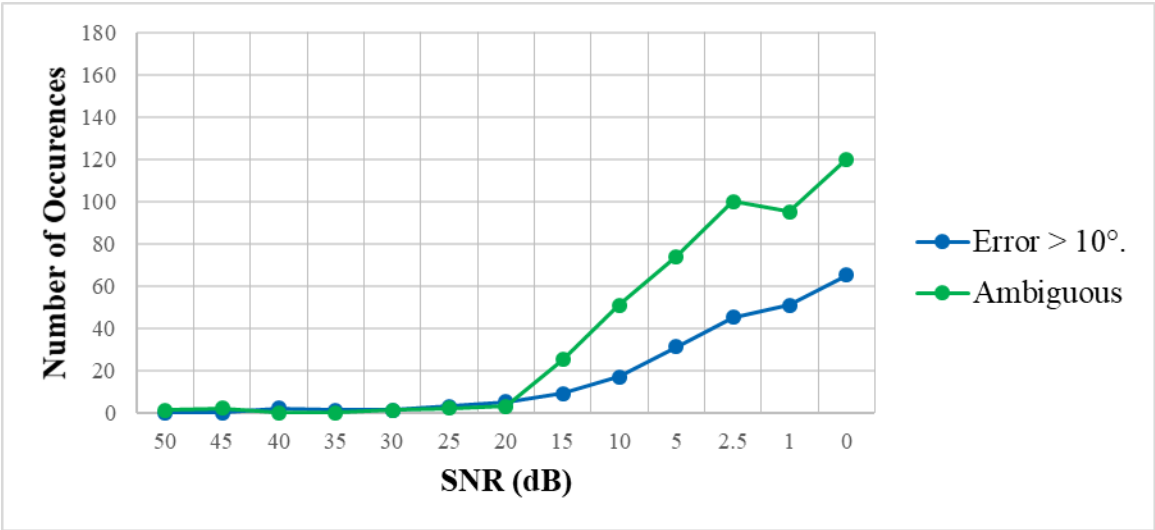

(a)

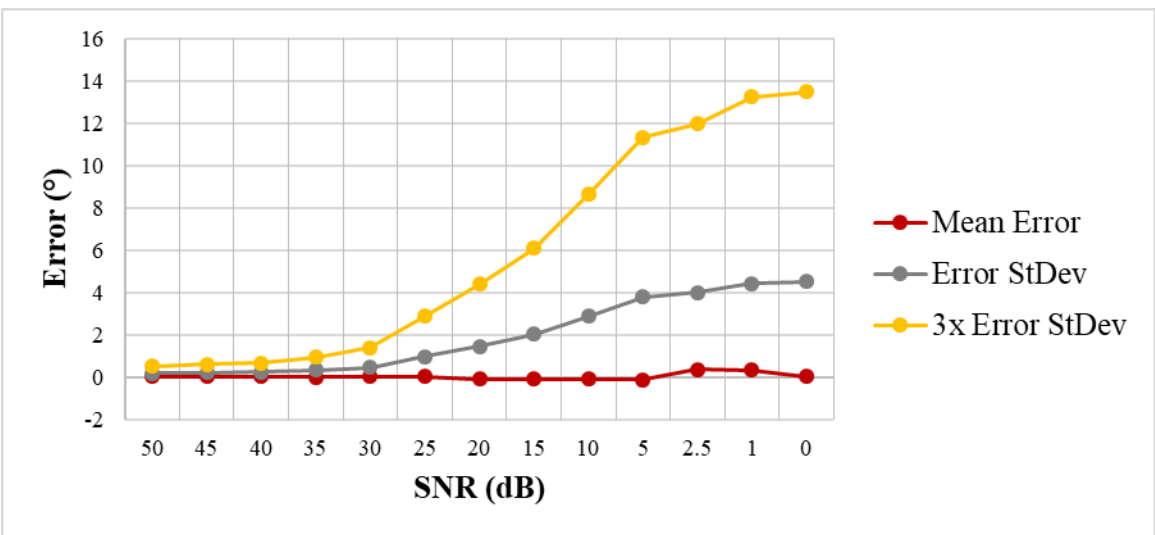

(b)

Figure 42. (a) SNR Effect on DOA Determination for Measured Cardioid Response – 0 Hz Central Frequency Mismatch (b) SNR Effect on Error for Measured Cardioid Response – 0 Hz Central Frequency Mismatch

The dramatic improvement observed for the cardioid directional response proves the hypothesis on back lobe suppression. A representative plot of the DOA determination is shown in Figure 43 for an SNR of 5 dB, indicating the DOA estimation error for low SNR.

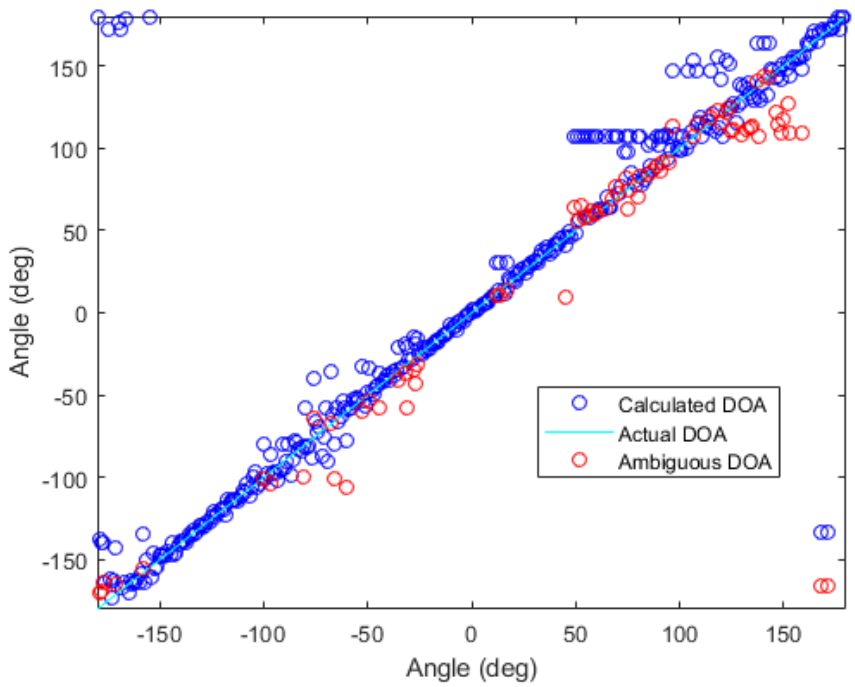

Figure 43. DOA Determination for a Cardioid Directional Response - 0 Hz Central Frequency Mismatch, 5 dB SNR

At this point, the directional pattern of choice is the one with a suppressed back lobe (cardioid), however, there is still benefit in investigating asymmetric dipole patterns with smaller back lobes, as aforementioned. Compearing the standard deviation of the error in Figure 36 (b) and Figure 42 (b), the asymmetric dipole directional pattern consistently has a lower standard deviation of the error than the cardioid direction pattern for the same SNR value. Of particular interest is to find the directional response that provide more robust results in presence of noise (lower SNR). This will be left for future studies.

THIS PAGE INTENTIONALLY LEFT BLANK

IV. CONCLUSION

The results of the proposed DOA estimation method using comparison across normalized calibration curves, has shown some promising results. The method also has some limitations and some areas where improvement could be made, which may hopefully guide future work.

A. SUMMARY OF RESULTS

Small, rotor powered UAVs have become ubiquitous in everyday life as they have become cheaper and easier to use. These commercially available UAVs are also sometimes used to carry out violent attacks with military goals. Defense against these small, multi-rotor UAV threats must first start with the ability to detect these small UAVs with accuracy and reliability. In this study, an algorithm to determine the direction of arrival of the sound produced by small rotor powered UAVs was developed for an array of three collocated *Ormia*-inspired MEMS sensors.

The MEMS sensors used in this study, when operated with open backs, exhibit a gradient directional pattern (dipole-like) in the main vibrational mode. A prism shaped housing was created to control the directional pattern of individual sensors, reducing and suppressing the back lobe of the dipole, forcing a directional asymmetry. The directional pattern of the full array is comprised of three asymmetric dipoles with an angular offset of 120°, forming three pairs of canted sensors.

This characteristic was used to provide a normalized calibration curve formed by the difference over the sum of each pair of sensors. This calibration curve represents the expected response of the sensor array to which the actual response is compared to determine the DOA of the acoustic signal. Because multiple possible DOAs are produced by the algorithm, they are compared, the possible DOAs with highest correlation are averaged and the result reported as the estimated DOA.

The difference over the sum of the sensor responses were fitted using piecewise polynomial fitting with a nearest neighbor search routine. An algorithm was developed to perform these procedures and provide the estimated DOA. This algorithm was tested over

different conditions where noise and perturbations were artificially generated to account for frequency response mismatch among the sensors, signal-to-noise ratio, directional pattern variations, and drone type. The runtime of the algorithm, implemented in Matlab, was found to be approximately 0.03 seconds for a single DOA, when run on a typical office PC.

Analyses were conducted for three different directional responses from the sensors: a computer simulated asymmetric dipole pattern with the back lobe slightly smaller than the front, an experimentally obtained asymmetric dipole pattern with the back lobe approximately 60% lower than the front lobes, and an experimentally obtained cardioid pattern with the back lobe suppressed. As a general observation, the error in most of the conditions grew as more noise was added to the sensors' responses, compromising the accuracy of the DOA determination in cases of frequency response mismatch of 2 Hz and higher and SNR lower than 15 dB. Finally, the algorithm was tested over a variety of drones with different acoustic signatures and it was found to work relatively well across the drones tested. The greatest limitation here is the sensors' frequency response mismatch. Because the drones' acoustic signatures are essentially comprised of narrow spectral bands, a slight difference on the sensor's frequency response will provide a large difference from the calibration curve, which was obtained at the resonant peak. This effect was found less prominent for sources with more uniform spectral distributions. These errors were minimized when the frequency responses of the three sensors matched ideally.

Another important observation was the overall error was found to slightly reduce when the back lobe was reduced, due to reduction of ambiguous azimuthal regions in the calibration curve. This reduces the probability of ambiguous DOAs and large DOA errors. When the back lobe was totally suppressed, in the case of the cardioid pattern, the general error was significantly reduced. In this case, there are no ambiguous azimuthal regions in the calibration curve and the accuracy is high and uniform across the entire azimuth range of 360°.

There are several advantages of the discussed algorithm. The mathematical analysis of the sensor array, using the difference over the sum, pointed to a potential use of fractional reciprocal tangent functions which may potentially be leveraged for future development of

the algorithm with less computational requirement and more reliability. In addition, this algorithm is generic enough that it could potentially be adapted to accomplish inversion of any set of three non-injective functions, so long as the non-injective functions use the same input. This means for any three functions of the same input where the output is known, but there are multiple inputs that could produce the same output, the developed algorithm can be used to determine the actual input.

B. RECOMMENDATIONS FOR FUTURE WORK

Future work to improve the estimation of DOAs using a normalized calibration curve could include incorporating the tangent and fractional reciprocal tangent equations to directly calculate the possible DOAs instead of the current method of using a nearest neighbor algorithm on a piecewise polynomial model of the normalized calibration curve. Using tangent estimators would reduce computation time, remove the memory requirement for a large database of piecewise polynomial models, and improve reliability that is lost by using the nearest neighbor algorithm.

A second and distinct computational method for calculating the possible DOAs directly would be using fitted polynomial equations to model the difference over the sum curves. Accuracy for this method during this thesis was better than for the tangent equations, but still not perfect. These fitted polynomial equations could be improved in future work by splitting each portion of the normalized calibration curve into positive and negative halves to allow for more accurate modeling. Like the tangent equations, using a polynomial estimator would reduce computation time, require less memory, and remove the need for a nearest neighbor subroutine.

The correlation band, used to find the highest correlation DOAs in the algorithm can introduce significant errors. This occurs when the correlation band is either too small, excluding possible DOAs, or too large, incorporating possible DOAs that are not accurate and which skew the final DOA estimation. The correlation band is currently set as a constant parameter and does not dynamically adjust to improve accuracy. An alternative to a fixed correlation band would be to calculate the difference between the possible DOAs of the three Dif/Sum calibration curves and use the set of possible DOAs with the smallest

differences to estimate the DOA. This method would provide reliability in DOA determination by dynamically adjusting for possible DOAs that may spread in angle due to error introduced by noise or other factors. This method would also improve accuracy when noise is low by focusing in on only the narrowest difference in possible DOAs.

In addition to a more dynamic correlation method, overlapping the selected calibration curve intervals would reduce the errors caused by the interfaces between the intervals of the calibration curve. If an actual DOA is close to the edge of a calibration curve interval, noise can cause the input signals to be identified in the adjacent interval and consequently generate an erroneous DOA estimation. Overlapping the calibration curve intervals would potentially correct this issue.

Finally, a thorough analysis of the algorithm performance is warranted, where the back lobe of the MEMS sensors directional response is systematically varied to find the directional response that provide more robust results in presence of noise.

APPENDIX A. DERIVATION OF DIF/SUM TANGENT FUNCTIONS FOR THREE DIRECTIONAL SENSORS

Trigonometric identities are sourced from Joyce [42].

1. $abs(\cos\theta)$

2. $abs(\cos(\theta+\theta_{offset}))$

3. $$\frac{abs(\cos\theta) - abs(\cos(\theta+\theta_{offset}))}{abs(\cos\theta) + abs(\cos(\theta+\theta_{offset}))}$$

4. $$\frac{abs(\cos\theta) - abs(\cos(\theta+\theta_{offset}))}{abs(\cos\theta) + abs(\cos(\theta+\theta_{offset}))} \times \frac{abs(\cos\theta) - abs(\cos(\theta+\theta_{offset}))}{abs(\cos\theta) - abs(\cos(\theta+\theta_{offset}))}$$

5. $$\frac{cos^2\theta - 2\times abs(\cos\theta\cos(\theta+\theta_{offset})) + cos^2(\theta+\theta_{offset})}{cos^2\theta - cos^2(\theta+\theta_{offset})}$$

6. $\cos 2\theta = 2\,cos^2\theta - 1$ [42]

7. $$\frac{1/2[\cos(2\theta) + 1 + cos(2\theta+2\theta_{offset}) + 1] - 2\times abs[\cos\theta\cos\left(\theta+\theta_{offset}\right)]}{1/2\left(\cos(2\theta) + 1 - \cos(2\theta+2\theta_{offset}\right) - 1)}$$

8. $$\cos\alpha\cos\beta = \frac{\cos(\alpha+\beta)\cos(\alpha-\beta)}{2}$$ [42]

9. $$\frac{1/2[\cos(2\theta) + cos(2\theta+2\theta_{offset}) + 2] - abs[\cos(2\theta+\theta_{offset}) + cos\left(-\theta_{offset}\right)]}{1/2\left(\cos(2\theta) - \cos(2\theta+2\theta_{offset}\right))}$$

10. $$\frac{1/2[\cos(2\theta) + cos(2\theta+2\theta_{offset})]}{1/2\left(\cos(2\theta) - \cos(2\theta+2\theta_{offset}\right))} + \frac{1}{1/2\left(\cos(2\theta) - \cos(2\theta+2\theta_{offset}\right))} - \frac{abs[\cos(2\theta+\theta_{offset}) + cos\left(-\theta_{offset}\right)]}{1/2\left(\cos(2\theta) - \cos(2\theta+2\theta_{offset}\right))}$$

11. $\cos(\alpha) - \cos(\beta) = -2\sin\left(\frac{\alpha+\beta}{2}\right)\sin(\frac{\alpha-\beta}{2})$ [42]

12. $\cos(\alpha) + \cos(\beta) = 2\cos\left(\frac{\alpha+\beta}{2}\right)\cos(\frac{\alpha-\beta}{2})$ [42]

13. $$\frac{\cos\left(\frac{2x+2x+2\theta_{offset}}{2}\right)\cos\left(\frac{2x-2x-2\theta_{offset}}{2}\right)}{-\sin\left(\frac{2x+2x+2\theta_{offset}}{2}\right)\sin\left(\frac{2x-2x-2\theta_{offset}}{2}\right)}+\frac{1}{-\sin\left(\frac{2x+2x+2\theta_{offset}}{2}\right)\sin\left(\frac{2x-2x-2\theta_{offset}}{2}\right)}-\frac{abs[\cos(2x+\theta_{offset})+\cos\left(-\theta_{offset}\right)]}{-\sin\left(\frac{2x+2x+2\theta_{offset}}{2}\right)\sin\left(\frac{2x-2x-2\theta_{offset}}{2}\right)}$$

14.

$$\frac{\cos(2x+\theta_{offset})\cos(-\theta_{offset})}{-\sin(2x+\theta_{offset})\sin(-\theta_{offset})}-\frac{1}{\sin(2x+\theta_{offset})\sin(-\theta_{offset})}-\frac{abs[\cos(2x+\theta_{offset})+\cos\left(-\theta_{offset}\right)]}{-\sin(2x+\theta_{offset})\sin(-\theta_{offset})}$$

15.

$$\frac{\cos(2x+\theta_{offset})\cos(-\theta_{offset})}{-\sin(2x+\theta_{offset})\sin(-\theta_{offset})}-\frac{1}{\sin(2x+\theta_{offset})\sin(-\theta_{offset})}+\frac{abs[\cos(2x+\theta_{offset})+\cos\left(-\theta_{offset}\right)]}{\sin(2x+\theta_{offset})\sin(-\theta_{offset})}$$

16. $\sin(-\theta)=-\sin(\theta)$ [42]

17. $\cot\theta=\frac{\sin\theta}{\cos\theta}$ [42]

18.

$$-\cot(2x+\theta_{offset})\operatorname{cotan}(-\theta_{offset})-\csc(2x+\theta_{offset})\csc(-\theta_{offset})+\frac{abs[\cos(2x+\theta_{offset})+\cos\left(-\theta_{offset}\right)]}{\sin(2x+\theta_{offset})\sin(-\theta_{offset})}$$

19. $\cos(-\theta)=\cos(\theta)$ [42]

20.

$$-\cot(2x+\theta_{offset})\cot(-\theta_{offset})-\csc(2x+\theta_{offset})\csc(-\theta_{offset})+\csc(-\theta_{offset})\frac{abs[\cos(2x+\theta_{offset})+\cos\left(-\theta_{offset}\right)]}{\sin(2x+\theta_{offset})}$$

21.

$$-\cot(2x+\theta_{offset})\cot(-\theta_{offset})-\csc(2x+\theta_{offset})\csc(-\theta_{offset})+\csc(-\theta_{offset})\frac{abs[\cos(2x+\theta_{offset})+\cos\left(-\theta_{offset}\right)]}{\sin(2x+\theta_{offset})}$$

Using $\theta_{offset}=120^\circ$, for three sensors spaced to evenly divide 360°.

22.

$$-\frac{1}{\sqrt{3}}\cot(2x+\theta_{offset})+\frac{2}{\sqrt{3}}\csc\left(2x+\theta_{offset}\right)-\frac{2}{\sqrt{3}}\frac{abs\left[\cos(2x+\theta_{offset})-\frac{1}{2}\right]}{\sin(2x+\theta_{offset})}$$

Case 1: Evaluate absolute value as positive.

23. $-\frac{1}{\sqrt{3}}cot(2x+\theta_{offset}) + \frac{2}{\sqrt{3}}\csc\left(2x+\theta_{offset}\right) - \frac{2}{\sqrt{3}}\frac{+[\cos(2x+\theta_{offset}) - \frac{1}{2}]}{\sin(2x+\theta_{offset})}$

24.

$$-\frac{1}{\sqrt{3}}cot(2x+\theta_{offset}) + \frac{2}{\sqrt{3}}\csc\left(2x+\theta_{offset}\right) - \frac{2}{\sqrt{3}}\left[cot\left(2x+\theta_{offset}\right) - (\frac{1}{2})csc\left(2x+\theta_{offset}\right)\right]$$

25.

$$-\frac{1}{\sqrt{3}}cot(2x+\theta_{offset}) + \frac{2}{\sqrt{3}}\csc\left(2x+\theta_{offset}\right) - \frac{2}{\sqrt{3}}\cot\left(2x+\theta_{offset}\right) + \frac{1}{\sqrt{3}}csc(2x+\theta_{offset})$$

26. $-\sqrt{3}cot(2x+\theta_{offset}) + \sqrt{3}\csc\left(2x+\theta_{offset}\right)$

27. $-\sqrt{3}\frac{1-cos(4x+2\theta_{offset})}{sin(4x+2\theta_{offset})} + \sqrt{3}\frac{1}{\sin\left(2x+\theta_{offset}\right)}$

28. $\frac{\sqrt{3}}{sin(2x+\theta_{offset})}(-cos(2x+\theta_{offset}) + 1)$

29. $\sqrt{3}(-cot(2x+\theta_{offset}) + \csc(2x+\theta_{offset}))$

30. $\tan\theta/2 = \frac{1-\cos\theta}{\sin\theta}$ [42]

31. $\tan\theta/2 = \csc\theta - \cot\theta$

32. $\sqrt{3}(tan(x+\theta_{offset}/2))$

From eqn. 22, the $\sqrt{3}$ is the result of

33. $\cot(-\theta_{offset}) - \csc(-\theta_{offset})$

From (18),

34. $\frac{\cos(-\theta_{offset})}{\sin(-\theta_{offset})} - \csc(-\theta_{offset})$

35. $\frac{\cos(-\theta_{offset})}{\sin(-\theta_{offset})} - \csc(-\theta_{offset})$

36. $\cos(-\theta) = \cos(\theta)$ [42]

From (17),

37. $-\dfrac{\cos(\theta_{offset})}{\sin(\theta_{offset})} + \csc(\theta_{offset})$

38. $-\cot\theta_{offset} + \csc(\theta_{offset})$

From (34),

39. $\tan\theta_{offset}/2$

From (33) and (36),

40. $(\tan\theta_{offset}/2)\,(\tan(x+\theta_{offset}/2))$ Q.E.D

Case 2: Evaluate absolute value as negative.

From (23),

41. $-\dfrac{1}{\sqrt{3}}\cot(2x+\theta_{offset}) + \dfrac{2}{\sqrt{3}}\csc\left(2x+\theta_{offset}\right) - \dfrac{2}{\sqrt{3}}\dfrac{-[\cos(2x+\theta_{offset}) - \frac{1}{2}]}{\sin(2x+\theta_{offset})}$

42.

$$-\frac{1}{\sqrt{3}}\cot(2x+\theta_{offset}) + \frac{2}{\sqrt{3}}\csc\left(2x+\theta_{offset}\right) + \frac{2}{\sqrt{3}}\left[\cot\left(2x+\theta_{offset}\right) - \left(\frac{1}{2}\right)\csc\left(2x+\theta_{offset}\right)\right]$$

43.

$$-\frac{1}{\sqrt{3}}\cot(2x+\theta_{offset}) + \frac{2}{\sqrt{3}}\csc\left(2x+\theta_{offset}\right) + \frac{2}{\sqrt{3}}\cot\left(2x+\theta_{offset}\right) - \left(\frac{1}{\sqrt{3}}\right)\csc\left(2x+\theta_{offset}\right)$$

44. $\dfrac{1}{\sqrt{3}}\csc\left(2x+\theta_{offset}\right) + \dfrac{1}{\sqrt{3}}\cot\left(2x+\theta_{offset}\right)$

45. $\tan\theta/2 = \dfrac{\sin\theta}{1+\cos\theta}$ [42]

46. $\tan\theta/2\,(1+\cos\theta) = \sin\theta$

47. $\csc\theta + \cot\theta = \cot\theta/2$

From (44),

48. $\frac{1}{\sqrt{3}}\cot\left(\theta+\theta_{offset}\right)$

49. $\frac{1}{\sqrt{3}\,\tan\left(\theta+\theta_{offset}\right)}$

From (39), $\sqrt{3}=\tan{}^{\theta_{offset}}/_{2}$

50. $\frac{1}{\tan{}^{\theta_{offset}}/_{2}\,\tan\left(\theta+{}^{\theta_{offset}}/_{2}\right)}$ Q.E.D

The match between these derived functions and the original Dif/Sums is shown in Figure 44.

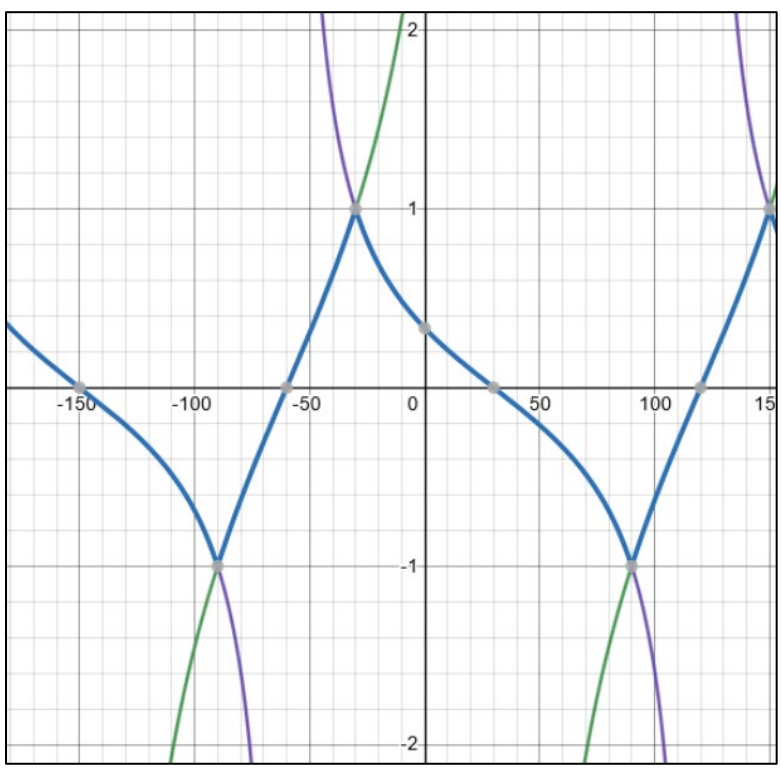

Blue line: Dif/Sum of two absolute cosine functions
Purple line: tangent function
Green line: fractional reciprocal of the tangent function

Figure 44. Difference over the sum of two absolute cosine functions compared to a tangent function and its fractional reciprocal

THIS PAGE INTENTIONALLY LEFT BLANK

APPENDIX B. DERIVATION OF DIF/SUM TANGENT FUNCTIONS FOR SENSORS OF UNEQUAL MAGNITUDES

Trigonometric identities are sourced from Joyce [42].

1. $abs\ (A\cos\theta)$ where A is an unknown constant

2. $abs\ (B\cos(\theta+\theta_{offset})$ where B is an unknown constant

3. $$\frac{abs(A\cos\theta) - abs(B\cos(\theta+\theta_{offset}))}{abs(A\cos\theta) + abs(B\cos(\theta+\theta_{offset}))}$$

4. $$\frac{abs(A\cos\theta) - abs(B\cos(\theta+\theta_{offset}))}{abs(A\cos\theta) + abs(B\cos(\theta+\theta_{offset}))} \times \frac{abs(A\cos\theta) - abs(B\cos(\theta+\theta_{offset}))}{abs(A\cos\theta) - abs(B\cos(\theta+\theta_{offset}))}$$

5. $$\frac{A^2cos^2\theta - 2\times abs(AB\cos\theta\cos(\theta+\theta_{offset})) + B^2cos^2(\theta+\theta_{offset})}{A^2cos^2\theta - B^2cos^2(\theta+\theta_{offset})}$$

6. $\cos 2\theta = 2\,cos^2\,\theta - 1$ [42]

7. $$\frac{1/2[A^2\cos(2\theta) + A^2 + B^2cos(2\theta+2\theta_{offset}) + B^2] - 2\times abs[AB\cos\theta\cos\left(\theta+\theta_{offset}\right)]}{1/2\left(A^2\cos(2\theta) + A^2 - B^2\cos(2\theta+2\theta_{offset}\right) - B^2)}$$

8. $$\cos\alpha\cos\beta = \frac{\cos(\alpha+\beta) + \cos(\alpha-\beta)}{2}$$ [42]

9. $$\frac{1/2[A^2\cos(2\theta) + B^2cos(2\theta+2\theta_{offset}) + A^2 + B^2] - abs[AB\cos(2\theta+\theta_{offset}) + ABcos\left(-\theta_{offset}\right)]}{1/2\left(A^2\cos(2\theta) - B^2\cos(2\theta+2\theta_{offset} + A^2 - B^2\right))}$$

This equation cannot be simplified by trigonometric identities due to the introduction of the coefficients. However, since the denominator is the difference between two similar cosine functions, adjusted by some coefficients and offsets, it is reasonable to conclude that the simplified version of the denominator will be a cosine function, adjusted by some coefficients and offsets, of form

10. $C\cos(D\theta+E) + F$ where C, D, E and F are unknown constants

Likewise, the numerator is a sum of similar cosine functions, with one of those cosine functions taking either the positive or negative case due to the absolute value

function. Since a sine function is the same as a cosine function, offset by 90°, it is reasonable to assume the numerator, when simplified, can take the form of.

11. $G\sin(H\theta + I) + J$ where G, H, I and J are unknown constants

From this assumed numerator and this assumed denominator, and based on the derivation in Appendix A, it is further reasonable to extrapolate that a simplified form of this equation when the absolute value is taken as a positive value can be expressed as a tangent function of form

12. $K\tan(L\theta + M) + N$ Q.E.D. where K, L, M, and N are unknown constants

Based on the derivation in Appendix A. it is also expected that the absolute value expression, when evaluated as a negative, will result in a corollary function that is a fractional reciprocal to the tangent function in Equation 12, of form

13. $\dfrac{1}{K\tan(L\theta + M) + N}$ Q.E.D. where K, L, M, and N are unknown constants but the SAME constants as in Equation B.12

Testing these expectations graphically shows these assumptions to hold true, as shown in Figures 45 and 46. Constants K, L, M, and N are solved using fitting functions.

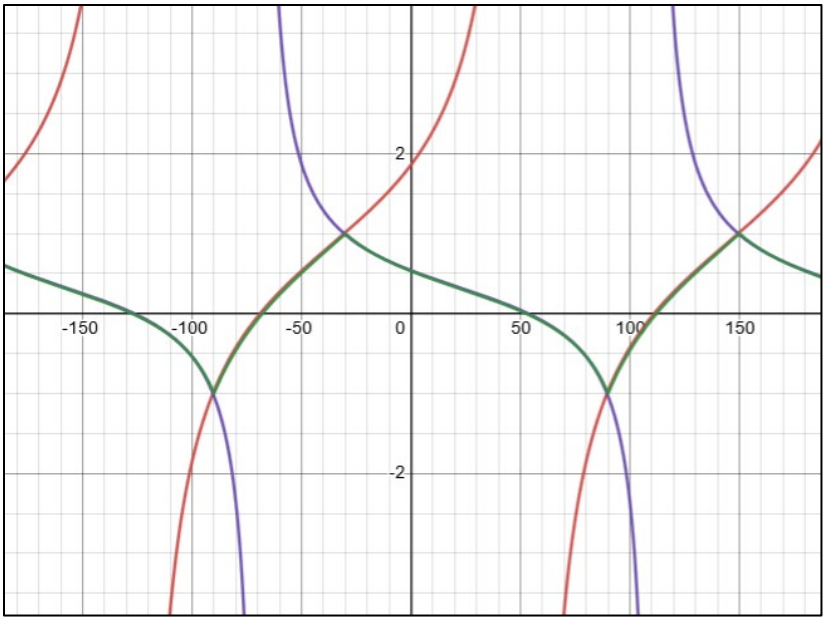

Green line: Dif/Sum curve

Red line: tangent curve

Purple line: fractional reciprocal tangent curve

Figure 45. Shadowed sensor response Dif/Sum curves (where A>B)

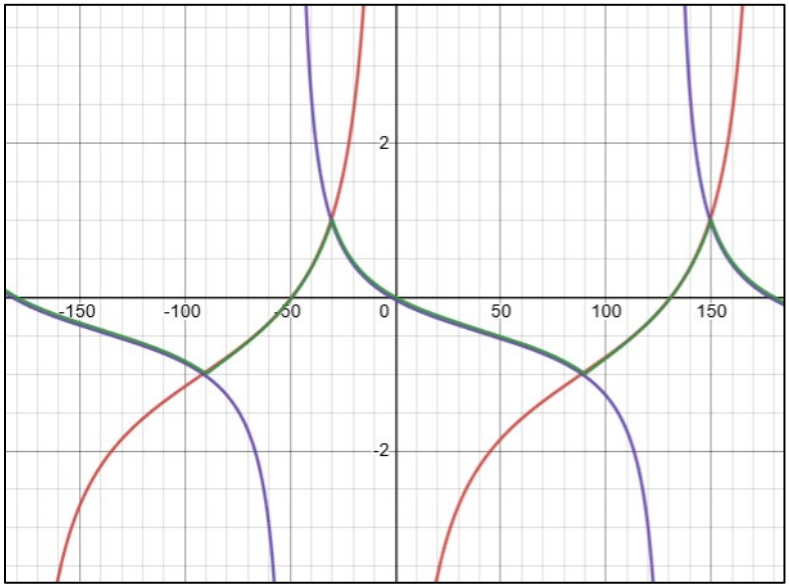

Green line: Dif/Sum curve

Red line: tangent curve

Purple line: fractional reciprocal tangent curve

Figure 46. Shadowed sensor response Dif/Sum curves (where A<B)

THIS PAGE INTENTIONALLY LEFT BLANK

APPENDIX C. ADDITIONAL DATA PLOTS

Additional data plots for the testing conducted in Section III are displayed below.

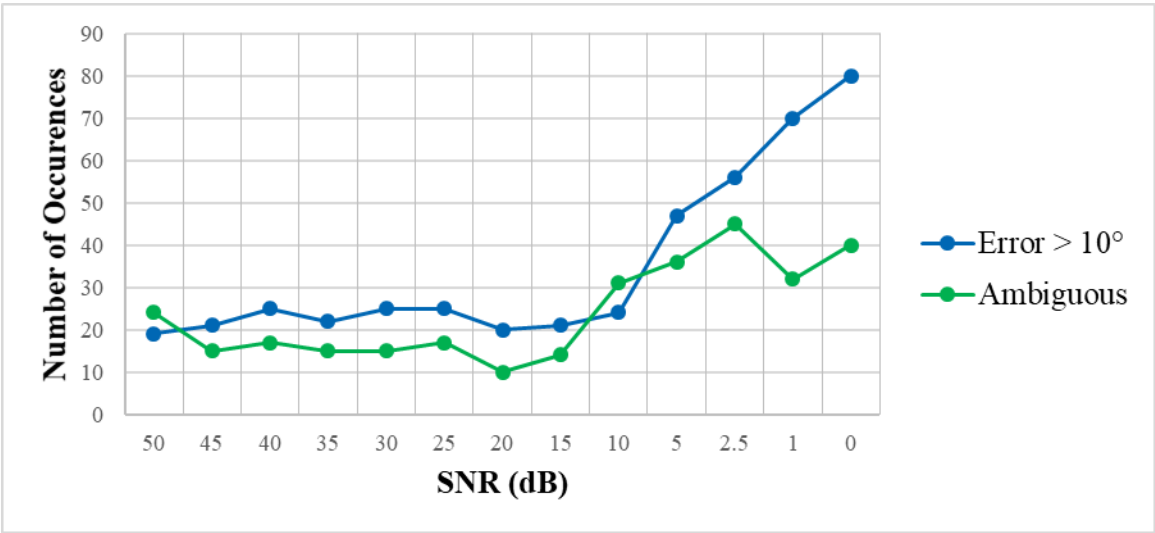

(a)

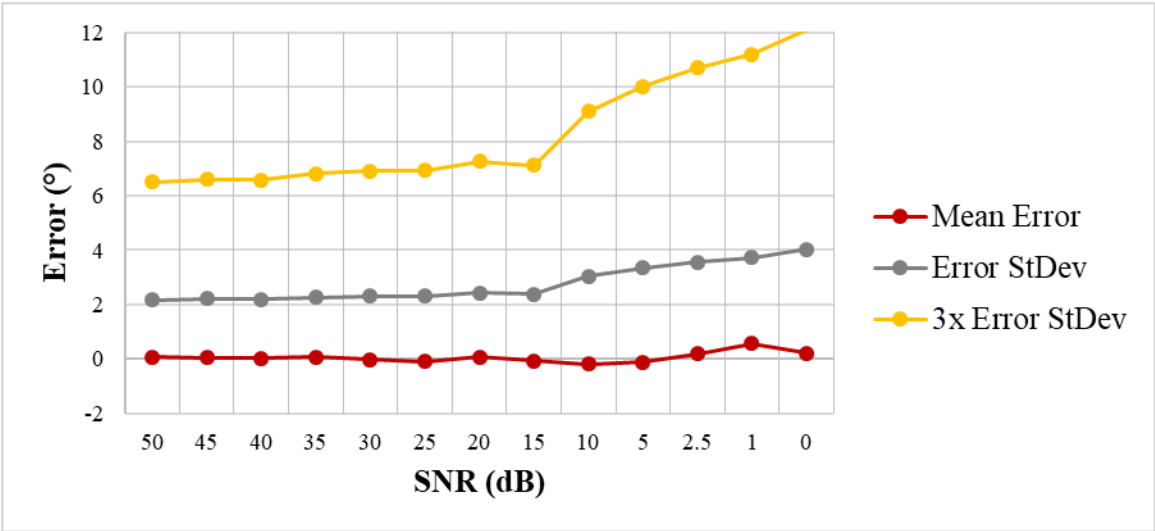

(b)

Figure 47. (a) SNR Effect on DOA Determination for Unloaded Typhoon – 10 Hz Central Frequency Mismatch (b) SNR Effect on Error for Unloaded Typhoon – 10 Hz Central Frequency Mismatch

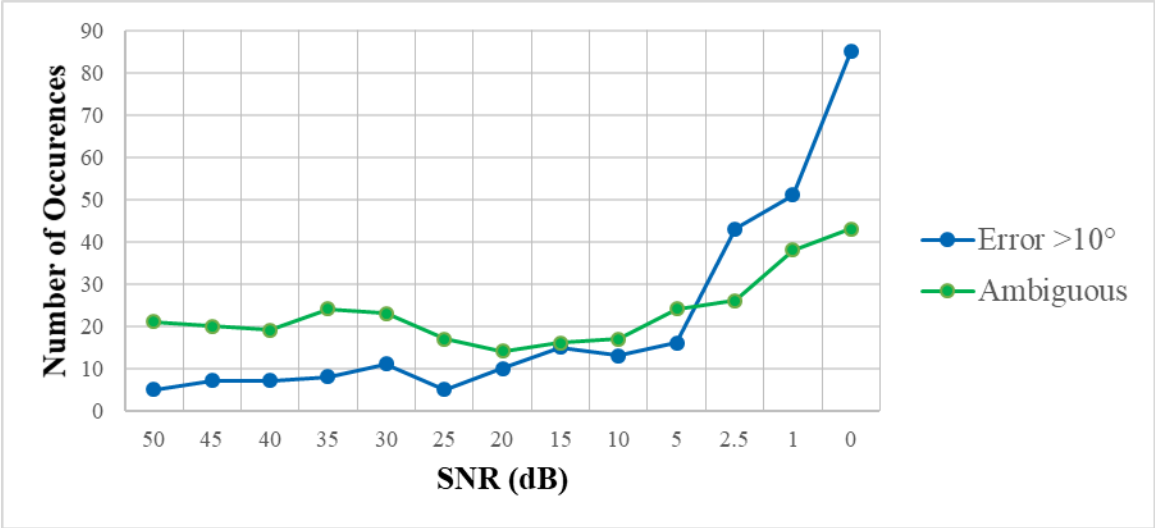

(a)

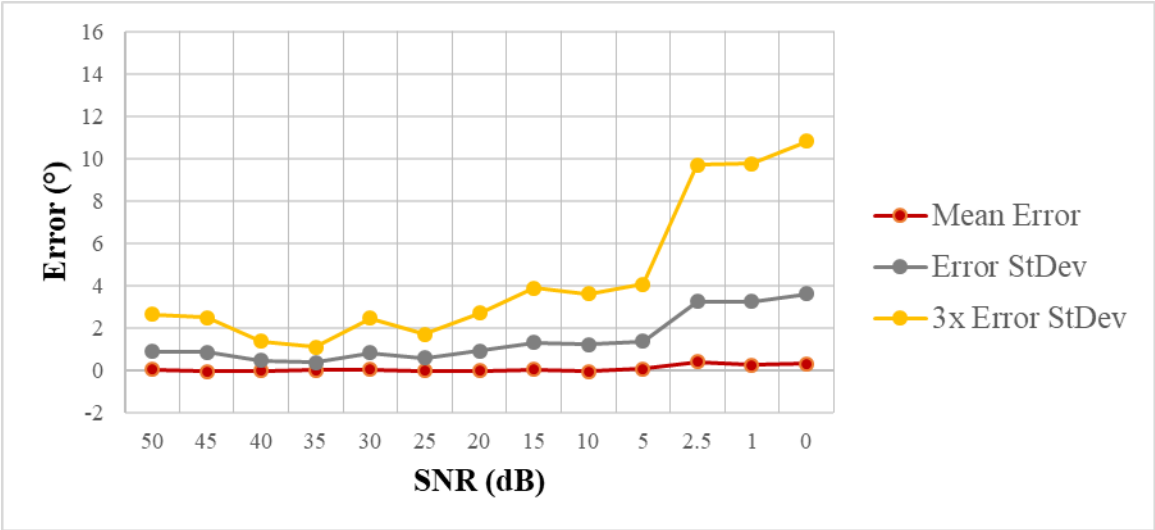

(b)

Figure 48. (a) SNR Effect on DOA Determination for Unloaded Typhoon – 0.5 Hz Central Frequency Mismatch (b) SNR Effect on Error for Unloaded Typhoon – 0.5 Hz Central Frequency Mismatch

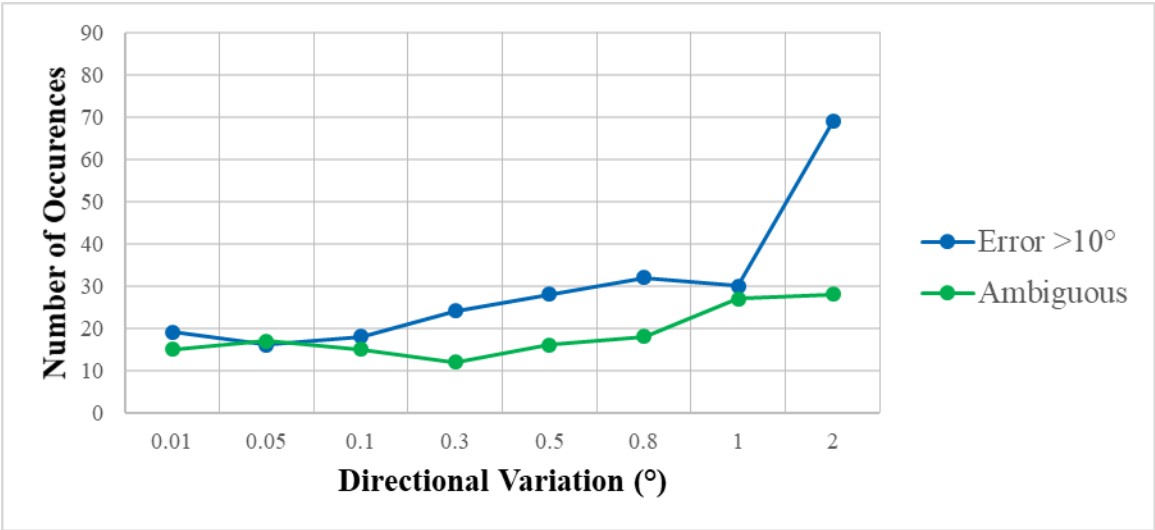

(a)

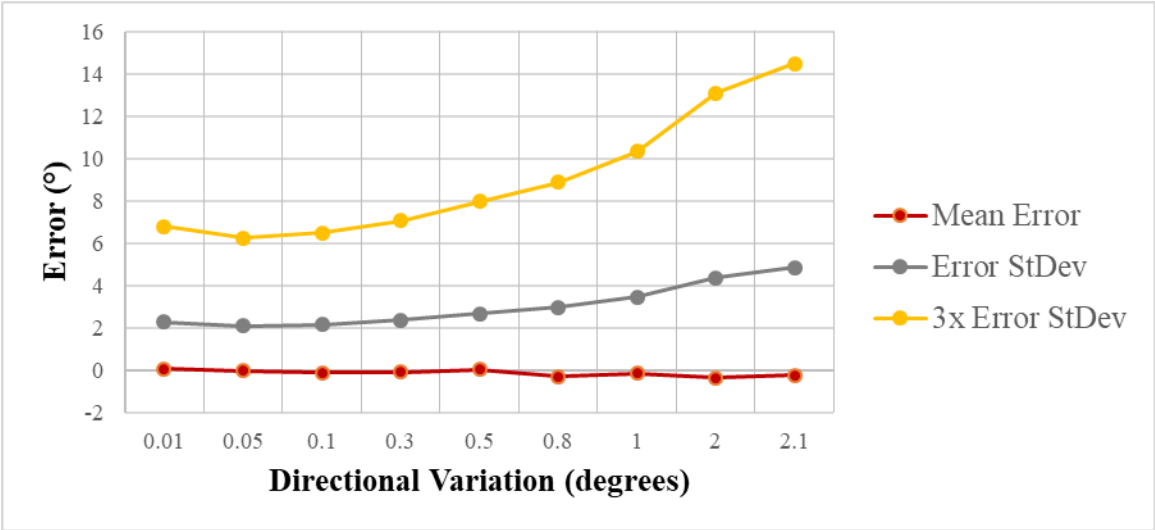

(b)

Figure 49. (a) Directional Variation Effect on DOA Determination for Unloaded Typhoon – 10 Hz Central Frequency Mismatch (b) Directional Variation Effect on Error for Unloaded Typhoon – 10 Hz Central Frequency Mismatch

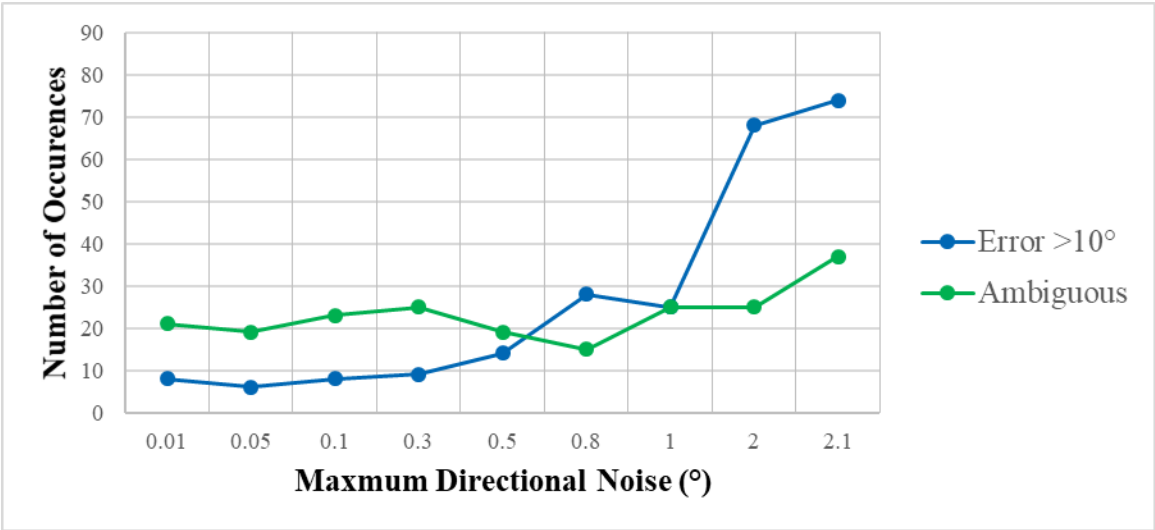

(a)

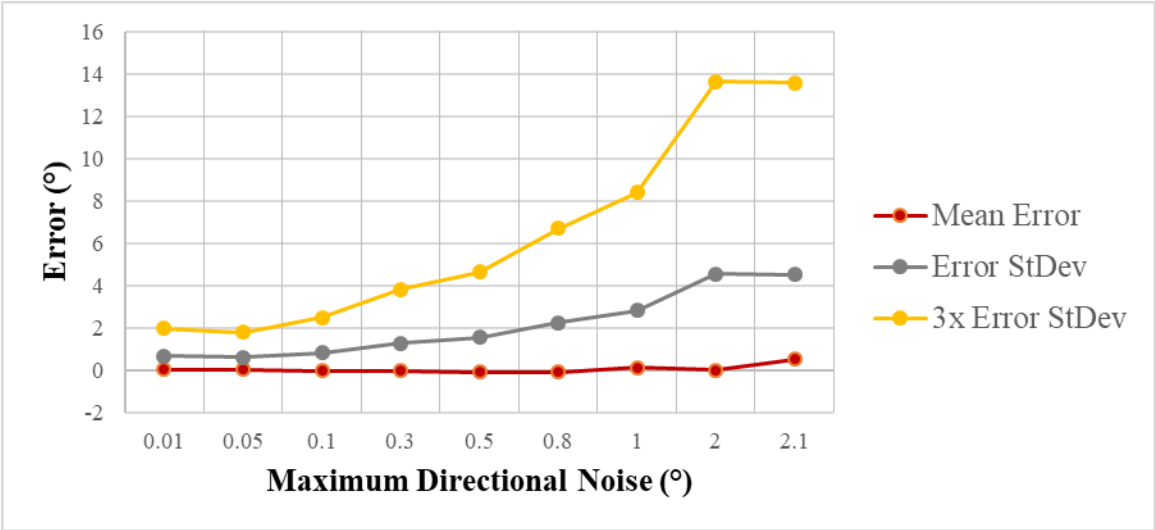

(b)

Figure 50. (a) Directional Variation Effect on DOA Determination for Unloaded Typhoon – 0.5 Hz Central Frequency Mismatch and SNR of 25 dB (b) Directional Variation Effect on Error for Unloaded Typhoon – 0.5 Hz Central Frequency Mismatch and SNR of 25 dB

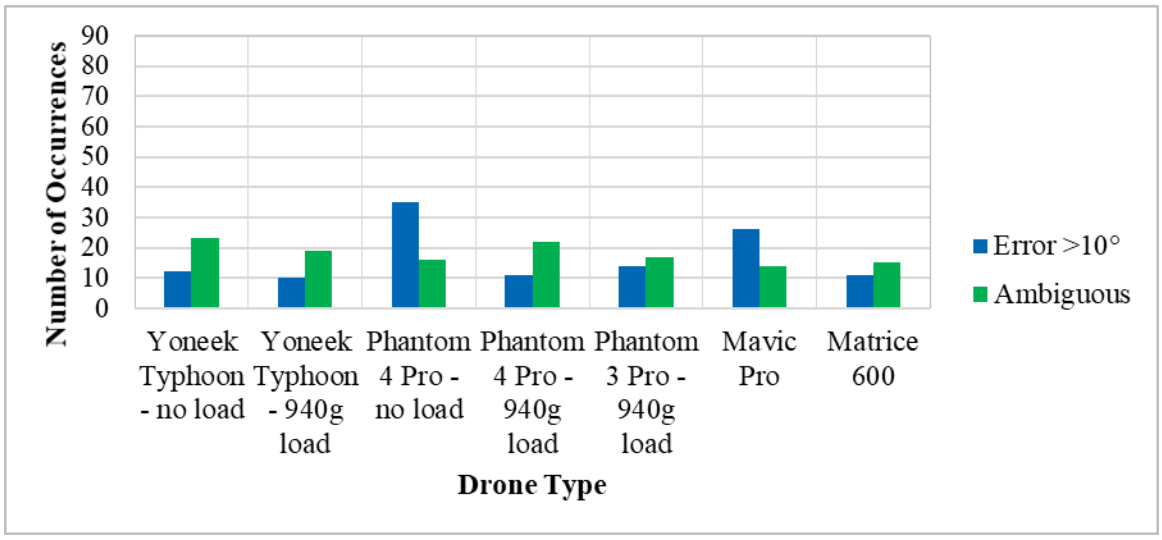

(a)

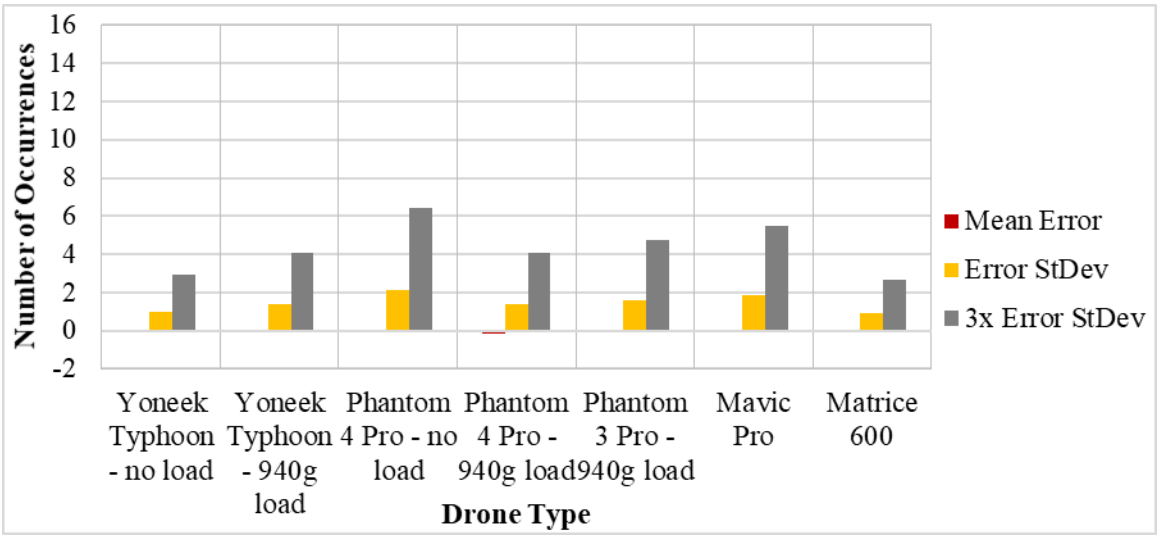

(b)

Figure 51. (a) Drone Type Effect on DOA Determination for Unloaded Typhoon – 0.5 Hz Central Frequency Mismatch, SNR of 25 dB, and 0.3° Maximum Directional Variation (b) Drone Type Effect on Error for Unloaded Typhoon – 0.5 Hz Central Frequency Mismatch, SNR of 25 dB, and 0.3° Maximum Directional Variation

THIS PAGE INTENTIONALLY LEFT BLANK

SUPPLEMENTAL

All Matlab scripts for this thesis and data collected are provided in the media supplementing this manuscript and can also be found at https://discover.dtic.mil/products-services/. Short descriptions of the routines are given below.

1. Matlab Computer Program - DataShaper.mat

Loads unaltered sensor data files produced by Zurich LabOne software in the form of a time stamp column and voltage response column, de-concatenates the data, removes outliers, and prompts the user to find the beginning and end of a 360° rotation of the sensor array. Saves the trimmed and cleaned data in a file to be used by CreateCalibrationCurve.mat.

2. Matlab Computer Program - CreateCalibrationCurve.mat

Loads trimmed data file produced by DataShaper.mat, calculates the Dif/Sum curves, finds and marks the angular intervals where the relative magnitudes of the unaltered sensor are constant, and saves a data file for use in DOADetermination.mat.

3. Matlab Computer Program - AudioSampling.mat

Loads and samples drone audio files, applies the directions response curve from COMSOL SensorResponse.mat and the frequency response curve from COMSOLFrequencyResponse.mat, applies the selected directional noise and central frequency shifts inputted by the user, and saves the resulting sensor response file for use in DOADetermination.mat.

4. Matlab Computer Program - COMSOLDirectionalResponse.mat

Contains the directional response curve for the *Ormia*-inspired MEMS sensor as modeled in COMSOL for use in CreateCalibrationCurve.mat and AudioSampling.mat.

5. Matlab Computer Program - COMSOLFrequencyResponse.mat

Contains the frequency response curve for the *Ormia*-inspired MEMS sensor as modeled in COMSOL for use in AudioSampling.mat.

6. Matlab Computer Program - AsymmetricDipoleDirectionalResponse.mat

Contains the measured asymmetric dipole directional response curve for the *Ormia*-inspired MEMS sensor for use in CreateCalibrationCurve.mat and AudioSampling.mat.

7. Matlab Computer Program - CardioidDirectionalResponse.mat

Contains the measured cardioid directional response curve for the *Ormia*-inspired MEMS sensor for use in CreateCalibrationCurve.mat and AudioSampling.mat.

8. Matlab Computer Program - DOADetermination.mat

Uses the sampled audio sensor response file from AudioSampling.mat, the calibration curve from CreateCalibrationCurve.mat, and the method described in this thesis to estimate the DOA of the sampled drone over 360°, outputting the results in a series of graphs and data entries.

9. Excel Spreadsheet – Algorithm Results.xlsx

Tabulated data from analytical tests of the algorithm.

LIST OF REFERENCES

[1] P. Belton, "Game of drones: As prices plummet drones are taking off," BBC, 16 Jan. 2015, [Online]. Available: https://www.bbc.com/news/business-30820399

[2] R. Miles, D. Robert, and R. R. Hoy, "Mechanically coupled ears for directional hearing in the parasitoid fly *Ormia* ochracea," *J. Acoust. Soc. Am.,* vol. 98, pp. 3059–3070, Dec. 1995 [Online]. Available: https://doi.org/10.1121/1.413830

[3] A. Mason, M. L. Oshinsky, and R. R. Hoy, "Hyperacute directional hearing in a microscale auditory system," *Nature*, vol. 410, pp. 686–690, Apr. 2001 [Online]. Available: https://doi.org/10.1038/35070564

[4] J. Blauert, Spatial Hearing: The Psychophysics of Human Sound Localization (Revised Edition), Cambridge, MA, USA: Massachusetts Institute of Technology, 1996 [Online]. Available: https://doi.org/10.7551/mitpress/6391.001.0001

[5] M. Risoud. J. N. Hanson, F. Gauvrit, C. Renard, P. E. Lemesre, N. X. Bonne, and C. Vincent, "Sound source localization," *Eur. Ann. Otorhinolaryngol. Head Neck Dis.*, vol. 135, no. 4, pp. 259–264, Aug. 2018 [Online]. Available: https://doi.org/10.1016/j.anorl.2018.04.009

[6] S. W. Smith, *The Scientist and Engineer's Guide to Digital Signal Processing,* San Diego, CA, USA: California Technical Publishing, 2018 [Online]. Available: http://www.dspguide.com/pdfbook.htm

[7] M. L. Kuntzman, N. N. Hewa–Kasakarage, A. Rocha, D. Kim, and N. A. Hall, "Micromachined In-Plane Pressure–Gradient Piezoelectric Microphones," *IEEE Sens. J.,* vol. 15, no. 3, pp. 1347–1357, Mar. 2015 [Online]. Available: https://doi.org/10.1109/JSEN.2014.2361118

[8] V. S. Nagaraja, K. J. Rudresha, and S. L. Pinjare, "Design, Fabrication and Characterization of a Biologically Inspired MEMS Directional Microphone," *2018 IEEE Sens.*, 2018, pp. 1–4, 2019 [Online]. Available: https://doi.org/10.1109/ICSENS.2018.8630304

[9] Y. Zhang, R. Bauer, W. M. Whitmer, J. C. Jackson, J. F. C. Windmill, and D. Uttamchandani, "A MEMS microphone inspired by *Ormia* for spatial sound detection," *2018 IEEE Micro Electro Mech. Syst. (MEMS)*, Belfast, UK, 2018 [Online]. Available: https://doi.org/10.1109/MEMSYS.2018.8346532

[10] H. Liu, L. Currano, D. Gee, T. Helms, and M. Yu, "Understanding and mimicking the dual optimality of the fly ear," *Sci. Rep.*, vol. 3, Aug. 2013 [Online]. Available: https://doi.org/10.1038/srep02489

[11] X. Shen, L. Zhao, J. Xu, and X. Yao, "Mathematical analysis and micro-spacing implementation of acoustic sensor based on bio-inspired intermembrane bridge structure," *Sensors*, vol. 21, no. 9, pp. 3168, May 2021. [Online]. Available: https://doi.org/10.3390/s21093168

[12] Insider Intelligence, "Drone technology uses and applications for commercial, industrial and military drones in 2021 and the future," Business Insider, Jan. 12, 2021 [Online]. Available: https://www.businessinsider.com/drone-technology-uses-applications?op=1

[13] J. Pegues, "Drone over White House highlights security concerns," CBS News, Jan. 26, 2015 [Online]. Available: https://www.cbsnews.com/news/drone-over-white-house-sparks-new-security-concerns/

[14] B. Watson, "The drones of ISIS," Defense One, Jan. 12, 2017 [Online]. Available: https://www.defenseone.com/technology/2017/01/drones-isis/134542/

[15] D. Hambling, "Here's what we know about the drone attack on Iraq's Prime Minister," *Forbes*, Jun. 1, 2021 [Online]. Available: https://www.forbes.com/sites/davidhambling/2021/11/08/heres-what-we-know-about-the-drone-attack-on-iraqs-prime-minister/?sh=225fde2429f7

[16] BBC, "Iraqi PM al-Kadhimi survives drone attack on his home," Nov. 7, 2021 [Online]. Available: https://www.bbc.com/news/world-middle-east-59195399

[17] A. Batrawy, "Drone attack in Abu Dhabi claimed by Yemen's rebels kills 3," *The Associated Press,* Jan. 17, 2022 [Online]. Available: https://apnews.com/article/business-dubai-united-arab-emirates-abu-dhabi-yemen-8bdefdf900ce46a6fd6c7bc685bf838a

[18] The Associated Press News, "UAE bans flying of recreational drones after fatal attack," Jan. 23, 2022 [Online]. Available: https://apnews.com/article/business-dubai-middle-east-abu-dhabi-yemen-75425bbfc0d5e2d07d882d7bb123c8f2

[19] J. Hernandez, "A military drone with a mind of its own was used in combat, U.N. says," *National Public Radio*, Nov. 8, 2021 [Online]. Available: https://www.npr.org/2021/06/01/1002196245/a-u-n-report-suggests-libya-saw-the-first-battlefield-killing-by-an-autonomous-d

[20] E. Farge, "U.N. talks adjourn without deal to regulate 'killer robots," *Reuters*, Dec. 17, 2021 [Online]. Available: https://www.reuters.com/article/us-un-disarmament-idAFKBN2IW1UJ

[21] Z. Kallenborn, "Meet the future weapon of mass destruction, the drone swarm," *Bulletin of the Atomic Scientists, A*pr. 5, 2021 [Online]. Available: https://thebulletin.org/2021/04/meet-the-future-weapon-of-mass-destruction-the-drone-swarm/

[22] D. Hambling, “Turkish military to receive 500 swarming kamikaze drones,” *Forbes*, Jun. 17, 2020 [Online]. Available: https://www.forbes.com/sites/davidhambling/2020/06/17/turkish-military-to-receive-500-swarming-kamikaze-drones/?sh=52fd9d6c251a

[23] D. Hambling, “China releases video of new barrage swarm drone launcher,” *Forbes*, Oct. 14, 2020 [Online]. Available: https://www.forbes.com/sites/davidhambling/ 2020/10/14/china-releases-video-of-new-barrage-swarm-drone-launcher/?sh=543af702ad7f

[24] Raytheon Missiles and Defense, “Mind of the swarm,” Jun. 29, 2018 [Online]. Available: https://www.raytheonmissilesanddefense.com/news/2018/06/29/mind-swarm

[25] D. Hambling, “Israel’s combat-proven drone swarm may be start of a new kind of warfare,” *Forbes*, Jul. 21, 2021 [Online]. Available: https://www.forbes.com/sites/davidhambling/2021/07/21/israels-combat-proven-drone-swarm-is-more-than-just-a-drone-swarm/?sh=32be61fd1425

[26] S. Wong, R. Jassemi-Zargani, and B. Kim, “Counter-measures against drone surveillance,” Ottawa, ON, CAN, 2016 [Online]. Available: https://cradpdf.drdc-rddc.gc.ca/PDFS/unc228/p803837_A1b.pdf

[27] T. Humphreys, “Statement on the security threat posed by unmanned aerial systems and possible countermeasures,” Austin, TX, USA, 2015 [Online]. Available: https://docs.house.gov/meetings/HM/HM09/20150318/103136/HHRG-114-HM09-Wstate-HumphreysT-20150318.pdf

[28] A. Rahaman and B. Kim, “Sound source localization by *Ormia ochracea* inspired low–noise piezoelectric MEMS directional microphone,” *Sci. Rep.,* vol. 10, Jun. 2020. [Online]. Available: https://doi.org/10.1038/s41598-020-66489-6

[29] R. C. Rabelo, F. D. Alves, and G. Karunasiri, “Electronic phase shift measurement for the determination of acoustic wave DOA using single MEMS biomimetic sensor,” *Sci. Rep*., vol. 10, Jul. 2020 [Online]. Available: https://doi.org/10.1038/s41598-020-69563-1

[30] L. Liu, M. Yang, Y. Zhang, X. Zhu, N. Ta, and Z. Rao, ““A miniature four-microphone array for two-dimensional direction-of-arrival estimation based on biomimetic time-delay magnification,” *J. Vib. Acoust*, vol. 141, no. 2, Jan. 2019 [Online]. Available: https://doi.org/10.1115/1.4042124

[31] D. Wilmott, F. D. Alves, and G. Karunasiri, “Bio-Inspired miniature direction finding acoustic sensor,” *Sci. Rep*., vol. 6, Jul. 2016 [Online]. Available: https://doi.org/10.1038/srep29957

[32] Z. Shang, W. Zhang, G. Zhang, X. Zhang, L. Zhang, and R. Wang, "A study on MEMS vector hydrophone and its orientation algorithm," *Sens. Rev.,* vol. 40, no. 2, pp. 191–201, Mar. 2020. [Online]. Available: https://doi.org/10.1108/SR-05-2019-0120

[33] M. Liu, L. Nie, S. Li, W. Jia, L. Zhang, G. Zhang, and W. Zhang, "Array MEMS vector hydrophone oriented at different direction angles," *Sens.*, vol. 19, Oct. 2019 [Online]. Available: https://doi.org/10.3390/s19194282

[34] H. de Bree, "The Microflown: an acoustic particle velocity sensor," *Acoust. Aust.*., vol. 31, no. 3, pp, 91–94, Dec. 2003 [Online]. Available: https://www.researchgate.net/publication/226756123_The_Microflown_Particle_Velocity_Sensor

[35] Microflown Technologies, "*USP regular 3D sound intensity probe product data,*" 2019 [Online] Available: https://www.microflown.com/assets/uploads/Product-Data/Product-Data-USP-Regular.pdf

[36] I. Jáuregui Novo, "Blind source separation using acoustic vector sensors - AVS," M.S. thesis, Telecommun. Eng. Sch., Univ. of Vigo, Vigo, ES, 2017 [Online]. Available: http://castor.det.uvigo.es:8080/xmlui/bitstream/handle/123456789/92/TFM%20Ignacio%20Jauregui%20Novo.pdf?sequence=1

[37] D. S. Terracciano, R. Costanzi, V. Manzari, M. Stifani, A. Caiti, K. LePage, and L. Troiano, "Passive detection and bearing-only tracking of large-time bandwidth signals using an AUV mounted vector sensor," in *2019 UACE Conf.*, 2019 [Online]. Available: https://www.uaconferences.org/docs/2019_papers/UACE2019_893_Terracciano.pdf

[38] R. A. Rayburn, *Eargle's Microphone Book: From Mono to Stereo to Surround - a Guide to Microphone Design and Application*, Waltham, MA, USA: Focal Press, 2012, [Online]. Available: https://ebookcentral.proquest.com/lib/ebook-nps/detail.action?docID=788014.

[39] Mathworks, "fit." Accessed 30 May, 2022 [Online]. Available: https://www.mathworks.com/help/curvefit/fit.html

[40] Mathworks, "knnsearch." Accessed 30 May, 2022 [Online]. Available: https://www.mathworks.com/help/stats/knnsearch.html

[41] Mathworks, "rmoutliers." Accessed 30 May, 2022 [Online]. Available: https://www.mathworks.com/help/matlab/ref/rmoutliers.html

[42] D. E. Joyce, "Summary of trigonometric identities," Clark University, 1997 [Online]. Available: https://www2.clarku.edu/faculty/djoyce/trig/identities.html

INITIAL DISTRIBUTION LIST

1. Defense Technical Information Center
   Ft. Belvoir, Virginia

2. Dudley Knox Library
   Naval Postgraduate School
   Monterey, California